The Photophysics of Metal Halide Perovskites for Next-Generation Solar Cells

Elizabeth S. Martin

Department of Physics

University of Oxford

A thesis submitted in fulfilment of the requirements for the degree of

Doctor of Philosophy

Hilary Term 2019

The Photophysics of Metal Halide Perovskites for Next-Generation Solar Cells

Elizabeth S. Martin

Thesis submitted in fulfilment of the requirements for the degree of

Doctor of Philosophy at the University of Oxford.

ABSTRACT

Metal halide perovskites have emerged as a promising absorber material for efficient third generation solar cells. In this thesis, the photophysics of these materials are investigated by photoluminescence and optical absorption spectroscopy, focussing on the charge-carrier recombination dynamics and the band gap. The work primarily discusses tin-based perovskite materials, which allow the band gap to be tuned to lower values but currently display poor power conversion efficiencies due to rapid charge-carrier recombination. In addition, the effect of thickness on lead-based perovskites is investigated, allowing the band gap to reach higher values by quantum confinement.

First, the temperature dependent photoluminescence of $MASnI_3$ is examined. A dramatic reduction in PL spectral linewidth with a concomitant increase in PL lifetime is seen at the low temperature structural phase transition. This points to the deactivation of defects, thus reducing scattering and recombination. Defect tolerance may therefore be related to the structure of the perovskite and could be enhanced by a targeted structural change to increase the charge-carrier lifetime and improve solar cell efficiency.

Further to this, the PL lifetime and relative radiative efficiency of $FASn_xPb_{1-x}I_3$ are investigated to uncover how metal composition influences charge-carrier recombination mechanisms. The PL dynamics fall into two regimes, with the tin-rich samples displaying fast mono-exponential decay that is largely temperature-independent, and lead-rich samples having longer, more stretched decays dominated by multi-phonon recombination. Band gap bowing of the mixed metal $FASn_xPb_{1-x}I_3$ perovskites is found to be parabolic at all temperatures, and is most likely due to local deformations in the lattice to accommodate the random placement of lead and tin ions. The benefits of a lower band gap may therefore be achieved whilst keeping the slower charge-carrier recombination of lead perovskites, thus enabling high efficiency bottom cells for all perovskite tandem solar cells.

Finally, the prospect of band gap tuning is investigated from a different angle, by growing very thin films of $MAPbI_3$ by vapour deposition which display quantum confinement. Films initially grow as islands, with blue-shifted photoluminescence, before forming uniform films still thin enough to exhibit quantum confinement. These films could be used to develop efficient LEDs, and the exposition of the growth mode could also lead the way to producing large-area vapour deposited solar cells with larger grain size which improves both efficiency and stability.

Together, the results show that the metal composition, the structural phase (which can be adjusted by changing the organic and halide ions) and the dimensions of the material, can all impact the optoelectronic properties, allowing great scope for tuning the properties of these materials to optimize their photovoltaic performance.

PUBLICATIONS

(All publications are under the name E. S. Parrott.)

1. Parrott, E. S.; Milot, R. L.; Stergiopoulos, T.; Snaith, H. J.; Johnston, M. B.; Herz, L. M. Effect of Structural Phase Transition on Charge-Carrier Lifetimes and Defects in $CH_3NH_3SnI_3$ Perovskite. *J. Phys. Chem. Lett.* **2016**, *7*, 1321–1326.

2. Eperon, G. E.; Leijtens, T.; Bush, K. A.; Prasanna, R.; Green, T.; Wang, J. T.-W.; McMeekin, D. P.; Volonakis, G.; Milot, R. L.; May, R.; Palmstrom, A.; Slotcavage, D. J.; Belisle, R. A.; Patel, J. B.; Parrott, E. S.; Sutton, R. J.; Ma, W.; Moghadam, F.; Conings, B.; Babayigit, A.; Boyen, H.; Bent, S.; Giustino, F.; Herz, L. M.; Johnston, M. B.; McGehee, M. D.; Snaith, H. J. Perovskite-Perovskite Tandem Photovoltaics with Optimized Band Gaps. *Science.* **2016**, *364* (6314), 861–864.

3. Sutton, R. J.; Eperon, G. E.; Miranda, L.; Parrott, E. S.; Kamino, B. A.; Patel, J. B.; Hörantner, M. T.; Johnston, M. B.; Haghighirad, A. A.; Moore, D. T.; et al. Bandgap-Tunable Cesium Lead Halide Perovskites with High Thermal Stability for Efficient Solar Cells. *Adv. Energy Mater.* **2016**, *6* (8), 1502458.

4. Patel, J. B.; Wong-Leung, J.; Van Reenen, S.; Sakai, N.; Wang, J. T. W.; Parrott, E. S.; Liu, M.; Snaith, H. J.; Herz, L. M.; Johnston, M. B. Influence of Interface Morphology on Hysteresis in Vapor-Deposited Perovskite Solar Cells. *Adv. Electron. Mater.* **2017**, *3* (2), 1600470.

5. Crothers, T. W.; Milot, R. L.; Patel, J. B.; Parrott, E. S.; Schlipf, J.; Müller-Buschbaum, P.; Johnston, M. B.; Herz, L. M. Photon Reabsorption Masks Intrinsic Bimolecular Charge-Carrier Recombination in $CH_3NH_3PbI_3$ Perovskite. *Nano Lett.* **2017**, *17* (9), 5782–5789.

6. Parrott, E. S.; Green, T.; Milot, R. L.; Johnston, M. B.; Snaith, H. J.; Herz, L. M. Interplay of Structural and Optoelectronic Properties in Formamidinium Mixed Tin-Lead Triiodide Perovskites. *Adv. Funct. Mater.* **2018**, 1802803.

7. Parrott, E.S.; Patel, J. B.; Haghighirad, A.-A.; Snaith, H. J.; Johnston, M. B.; Herz, L. M., Growth Modes and Quantum Confinement in Ultrathin Vapor-Deposited $MAPbI_3$ Films. *Nanoscale*. **2019**, *11*, 14276.

CONFERENCE PRESENTATIONS

1. Oral presentation on "Photophysics of hybrid organic metal halide perovskites" at *CDT-PV Showcase,* Liverpool University, UK, Nov 2015.

2. Poster presentation on "Enhanced Photoluminescence and Solar Cell Performance via Lewis Base Passivation of Lead Halide Perovskites" at *RSC 'Next Generation Materials for Solar Photovoltaics' Symposium,* Royal Society of Chemistry, London, UK, Jan 2016.

3. Poster presentation on "Effect of structural phase transition on charge-carrier lifetimes and defects in $CH_3NH_3SnI_3$ perovskite" at *nanoGe 'International Conference on Hybrid and Organic Photovoltaics' (HOPV),* Swansea University, UK, May 2016.

4. Poster presentation on "Effect of structural phase transition on charge-carrier lifetimes and defects in $CH_3NH_3SnI_3$ perovskite" at *CDT-PV Showcase,* Liverpool University, UK, Nov 2016.

5. Oral presentation on Chapters 4 and 5 of this thesis at *'International Conference on Perovskite solar cells and optoelectronics' (PSCO),* EPFL, Lausanne, Switzerland**,** Oct 2018.

ACKNOWLEDGEMENTS

To thank all those who made this work possible, I must start by thanking the Maker of the sun and the earth, the Designer of the elements which form endless possibilities of materials, the Giver of intelligence and creativity, and the Source of all life and joy. 'The Lord is my light' (Oxford University motto and Psalm 27.1).

I would like to thank Prof Laura Herz, for your knowledge, insight and advice, and for supporting me throughout. Thanks also go to Prof Henry Snaith for your infectious enthusiasm.

Thanks to Prof Laura Herz and to Prof Michael Johnston for fostering a healthy group atmosphere, for opening up your home for barbeques and Lebkuchen competitions, and for managing the lab so efficiently. A big thank you to all of the Herz and Johnston lab groups: Becky Milot, Laura Martinez Maestro, Jessica Boland, Juliane Gong, Adam Wright, Jay Patel, Chris Davies, Waqaas Rehman, Tim Crothers, Juliane Borchert, Djamshid Damry, Sabrina Sterzl, Hannah Eggimann, Alex Knight, Kimberley Savill, Chelsea Xia, and many others who came before and after. Thank you for useful discussions over countless cups of tea, and for always being willing to lend an extra pair of hands in the lab. Thank you too for your excellent company, takeaways on 'helium nights', park lunches, pub trips, and games nights. I would also like to thank the Snaith group for collaboration and friendship, particularly Tom Green, Thomas Stergiopolous, Amir-Abbas Haghighirad, Giles Eperon, and Rebecca Sutton.

To all of the CDT-PV Cohort 1, thank you for your friendship, discussions, and for fun times on our 7 city tour.

Thanks also to my family who always encouraged inquisitiveness and nurtured a love of science from a young age. Thank you for taking an interest in my work. Thank you for looking after me when I was ill and supporting me through a difficult time. I would also like to thank my housemates Abbie and Gail, without whose kindness I would not have been able to return to Oxford; and my church family at St Ebbe's, for all their support. I would also like to thank the people of St Mary's Church, Maidenhead, and Grace Church, Boroughbridge, for their warm welcome and generous provision.

A special thanks to Toby Martin who has progressed from stranger to friend to fiancé to husband over the course of this thesis. Thank you for reminding me what is important, for your love and all your encouragement to keep going, and for still thinking solar panels are interesting!

TABLE OF CONTENTS

LIST OF ABBREVIATIONS

AFM	Atomic Force Microscopy
AM1.5	Standard solar spectrum
BAC	Band Anti-Crossing
CB1	Conduction Band
CCD	Charge-Coupled Device
CIGS	Copper Indium Gallium Di-selenide
CZTS	Copper Zinc Tin Sulphide
DFT	Density Functional Theory
DMF	N,N-Dimethylformamide
DMSO	Dimethyl sulfoxide
DSSC	Dye Sensitized Solar Cell
EQE	External Quantum Efficiency
EXAFS	Extended X-ray Absorption Fine Structure
FA	Formamidinium ($HC(NH_2)_2^+$)
FTIR	Fourier Transform Infrared spectrometer
FWHM	Full Width at Half Maximum
IRF	Instrument Response Function
LED	Light Emitting Diode
MA	Methylammonium ($CH_3NH_3^+$)
MD, RD	Measured Decay and Real Decay
NIR	Near Infrared
OD	Optical Density

PCE	Power Conversion Efficiency
PL	Photoluminescence
PLQE	Photoluminescence Quantum Efficiency
PV	Photovoltaic
SPAD	Single Photon Avalanche Diode
SRH	Shockley Read Hall recombination
T1, T2	High and low energy transition of $MASnI_3$
TCSPC	Time Correlated Single Photon Counting
TEM	Transmission Electron Microscopy
VCA	Virtual Crystal Approximation
XPS	X-ray Photoelectron Spectroscopy
XRD	X-ray diffraction
X, M, A	Halide anion, Metal cation, A cation

LIST OF SYMBOLS

a	Optical depth
A	Fraction of light absorbed
A	General Fitting Parameter
b	Bowing parameter
	Background absorption
B	Quantum Confinement fitting parameter
c	Speed of light
C	General fitting parameter
d	Quantum confinement dimension (i.e. film thickness)
d, d_0, d_s	Lattice d-spacing, unstrained d-spacing and sample d-spacing
D	Film thickness
e	Euler's number (e = 2.71828)
E	Photon Energy
E_a	Activation energy
E_b	Binding energy for excitons or dopants
E_g	Band gap energy
ΔE	Deviation of band gap from Vegard's law
F, F^{-1}	Fourier transform and Inverse Fourier transform
h	Plank's constant ($h = 6.626 \times 10^{-34}$ Js)
H	Crystallite height
I	Photoluminescence intensity
k	Boltzmann constant ($k = 8.617 \times 10^{-5}$ eV/K)

k_1, k_2, k_3	Mono-, bi-, and tri-molecular rate constants for charge-carrier recombination
K	Dimensionless recombination rate parameter $K = k_1/(k_2 \Delta n_0)$
L	Length of path through film, $L = D/\cos\theta_i$
n_0, p_0	Density of doped electrons/holes
n_1, p_1	Electron/hole densities in the conduction/valence band when the Fermi level is equal to the energy level of a SRH trap
n_1, n_2	Refractive indices of first and second material
Δn, Δp	Photoexcited charge-carrier density (for electrons or holes)
Δn_0	Initial photoexcited charge-carrier density after excitation with a laser pulse
N_0	Density of traps in a material
P	Escape probability of a photon from a film
r	Ratio of crystallite height to optical thickness
R, R_b, R_f	Fraction of incident light reflected from surface, from back interface and from front interface
R	Ratio of radiative to non-radiative recombination
t	Time after exciting a sample with a laser pulse
T	Temperature
T	Fraction of incident light transmitted
U_r, U_{nr}	Rate of radiative and non-radiative recombination
U_{SRH}	Rate of Shockley Read Hall recombination
x	Composition ratio of tin:lead
z	Depth in film of an emitted photon
α	Absorption coefficient
β	Stretched exponential parameter

β	XRD peak broadening
γ_{imp}	PL broadening due to ionizable impurities
Γ	PL line broadening (FWHM)
Γ_0	Temperature independent PL broadening due to defects
ϵ	Lattice parameter strain
θ	Bragg angle
θ_i, θ_t	Angles of incidence and transmission of light at a boundary
κ	Crystallite shape parameter
λ	Wavelength
τ, τ_{10}	Time taken for PL intensity to drop to 1/e and 1/10 of initial intensity
τ_{eff}	Effective PL lifetime for stretched exponential decay
τ_n, τ_p	Minority carrier lifetimes of electrons and holes in SRH recombination
φ	Radiative efficiency (PLQE)

1 INTRODUCTION

1.1 Context

The rapid expansion of the global energy demand, dwindling fossil fuel reserves and the desire to reduce carbon emissions all contribute to the interest in photovoltaics as a means of generating electricity, offering a sustainable energy source for the future. The global primary energy consumption is currently 17 TW[1] and is predicted to reach around 20 TW (200 PWh per year) by 2040,[2] a level which cannot be sustained by non-renewable energy sources including both fossil fuels and nuclear fuels. In contrast, the total solar irradiation of the Earth's landmasses is around 23 000 TW,[3] enough to power the world a thousand times over. Harnessing 20 TW from the sun would require 0.5% of land to be covered with 20% efficient solar panels, not including the additional land requirements of energy storage facilities. Whilst this is theoretically possible, it would require a global transmission network to ensure that energy generated in places with high solar irradiation (see Figure 1.1) is distributed to where it is needed. Countries such as the UK which are situated at higher latitudes and have a relatively high population density would find it hard to spare enough land to meet the energy requirements of the population. To reduce the amount of land needed, the efficiency of the solar panels must be increased. For example, the UK requires at least 9000 km^2 of 20% efficient solar panels (3.7% of the total UK land area) to meet all of its current

energy needs (1.6 PWh final energy consumption* in 2017[4]), whereas 6000 km^2 would be needed if the efficiency is increased to 30%, assuming an annual irradiation of 900 kWh/m^2.[5] Where land prices are at a premium, this also results in a much lower cost of electricity, providing the increased efficiency does not add too much to the fabrication costs of the solar cell.

For this reason, research into materials for low cost and high efficiency solar cells is much needed. A promising candidate to achieve this aim is the metal halide perovskite, a semiconducting crystalline material made from abundant elements with good optical and charge transport properties. Unlike traditional inorganic semiconductors they are surprisingly defect tolerant, enabling them to be easily fabricated by solution processing methods or vapour deposition. Metal halide perovskite solar cells currently have a record single-junction power conversion efficiency (PCE) of 23.7%,[6] and many demonstrations of PCEs over 20%,[7–10] despite having been researched for less than a decade (see Section 2.1.3 for more detailed background).

One feature of metal halide perovskites is that the band gap of these materials can be tuned with composition, allowing two or more compositions to be used in tandem, boosting the theoretical efficiency limit by absorbing separate portions of the solar spectrum (see Section 2.1.2). The materials in this family which have a low band gap suitable for use in the bottom cell of a tandem solar cell are tin or tin-lead triiodide perovskites. The performance has been much poorer than the lead triiodide perovskites so far, thought to be due to spontaneous p-doping which causes rapid charge-carrier recombination. Another method of tuning the band gap is to employ quantum confinement effects by decreasing the size. This has the additional advantage of

* Final energy is the total energy consumed by users, including electricity, petrol, natural gas and other fuels. This calculation therefore assumes that the same amount of energy is required if petrol and other fuels are replaced with electricity. In fact, electric vehicles and heat pumps are more efficient, whereas using the electricity to produce alternative fuels (e.g. H_2) would likely be less efficient but easier to store.

increasing the radiative efficiency, making them suitable for use in Light Emitting Diodes (LEDs).

1.2 Aims and overview

The broad goal of this thesis is to further our understanding of the photophysics of metal halide perovskites for the purpose of guiding improvements to their efficiency in solar cells. I will focus on the effects of structural phase, composition, and material dimension on the band gap and recombination dynamics of perovskite materials with methylammonium or formamidinium as the cation, tin or lead as the metal ion, and iodine as the halide ion. These materials are introduced in Chapter 2, along with the theory necessary to interpret the experimental results in this thesis, focussing on the band gap, defects, and charge-carrier recombination in semiconductors.

The photophysics of these perovskites will be explored primarily using the method of photoluminescence spectroscopy, including time-resolved and temperature-dependent measurements, along with absorption spectroscopy and X-ray diffraction. Chapter 3 contains a description of the experimental methods used and the ways in which the data were processed or fitted to give the final results in this thesis.

The first aim of this thesis is to investigate why tin-based perovskites have such fast charge-carrier recombination, which is discussed in Chapter 4. I explore this question further in Chapter 5 by investigating alloys of lead and tin perovskites and how the optoelectronic properties, particularly the charge-carrier recombination and radiative efficiency, behave with changing composition.

The second aim is to investigate the tunability of the band gap by two methods, namely band gap bowing and quantum confinement. In Chapter 5 I gain insight into the

band gap bowing phenomenon which allows alloys of lead and tin perovskites to attain lower band gaps than either of the parent compositions. Chapter 6 assesses the feasibility of tuning the band gap to higher values by growth of very thin layers of $MAPbI_3$ by vapour deposition.

Finally, Chapter 7 concludes this thesis, summarising the findings and providing direction for further work.

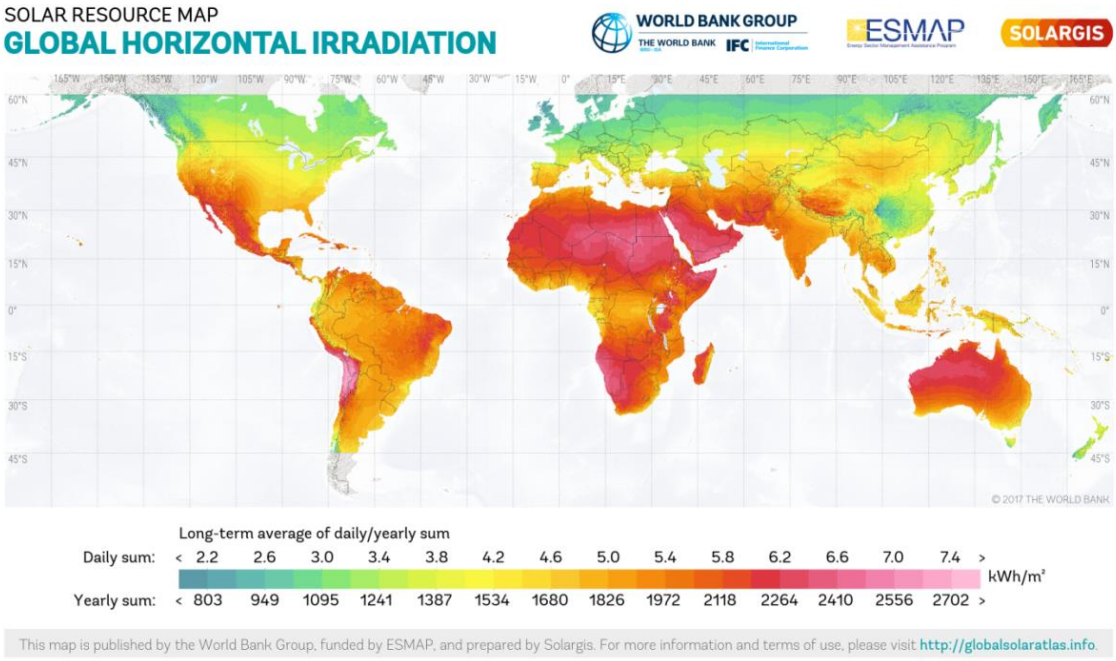

Figure 1.1. Map showing the long-term average of the solar irradiation of a horizontal plane on the Earth's surface in different parts of the world obtained from the Global Solar Atlas 2.0[†].[5]

[†] Global Solar Atlas is a free, web-based application developed and operated by the company Solargis s.r.o. on behalf of the World Bank Group, utilizing Solargis data, with funding provided by the Energy Sector Management Assistance Program (ESMAP). The image is reproduced under a Creative Commons 4.0 Attribution International license.

2 BACKGROUND AND THEORY

2.1 Solar cell background

2.1.1 Three generations

The first practical solar cell was demonstrated in 1954, with a power conversion efficiency (PCE) of 6%.[11] These first generation solar cells are made from doped silicon semiconductor wafers, creating a p-n homojunction with metal contacts to extract charge on either side. When a photon with energy greater than the band gap is absorbed by the semiconductor, an electron is promoted to the conduction band, leaving a positively charged hole in the valence band. Holes and electrons are separated by the intrinsic electric field across the junction, such that charge-carriers move freely to their respective contacts, generating a photocurrent and photovoltage. Silicon solar cells still dominate the commercial market, and the best lab PCEs are now nearing 27%,[12] with the record multi-crystalline modules (which are most commonly used) around 20% PCE.[12] They also have good stability, with commercial modules having guaranteed lifetimes of 25 years.[13] One drawback is that silicon has an indirect band gap, meaning the absorption coefficient is low and the wafers have to be thick (around 0.2 mm) to absorb all of the available sunlight.[14] Consequently, silicon is not suitable for applications which require the solar cell to be flexible. In addition the fabrication

process is energy intensive, particularly for monocrystalline silicon which produces the highest PCEs.[15]

Second generation solar cells are made from thin films of semiconductor material such as cadmium telluride (CdTe) and copper indium gallium diselenide (CIGS).[16] A p-n heterojunction is made by adding a thin layer of an oppositely doped semiconductor. The layers are grown directly onto a substrate, which could be glass or flexible plastic, coated with a transparent conducting oxide to make an electrical contact.[16] Due to the reduced volume of material, the fabrication cost and energy usage are lower than for silicon solar cells, resulting in a lower energy payback time.[15] However, their PCEs have lagged behind silicon. Recent progress has been made, with the best certified efficiency being 23% for a CIGS solar cell,[12] but the materials used are not earth abundant, and therefore cannot be deployed on the scale required to meet the predicted global energy demand. Materials developed to address this issue, such as amorphous silicon and copper zinc tin sulphide (CZTS), display much lower PCEs of around 11%.

Third generation solar cells include a wide range of technologies such as dye sensitized solar cells (DSSC), quantum dots and organic photovoltaics (OPV).[17] These materials use low cost and low energy manufacturing processes and can be coated or printed from solution onto many types of substrate. They can also be made in different colours by changing the dye or the size of the quantum dot. However they have not yet made a significant impact on the commercial market as they are a relatively new technology and have lower efficiencies of around 11%.[12] In general, this is due to poorer electronic properties, with lower mobilities, high disorder, and high exciton binding energies which prevent efficient charge separation.[17] They are also less stable,

and the expected working lifetime is not well known, with a demonstrated outdoor lifetime of only a couple of years for OPVs.[18]

2.1.2 Multi-junction solar cells

The materials discussed above have band gaps which fall in the optimum range for extracting the most power from the solar spectrum, as originally calculated by Shockley and Queisser.[19] The maximum theoretical current is limited by the number of incident photons with energy greater than the band gap, since lower energy photons cannot generate an electron-hole pair and are transmitted through the material. The maximum theoretical voltage is limited by the band gap of the material, since additional energy gained by charge-carriers from high energy photons is lost to thermalization as electrons quickly relax to the conduction band minimum, and holes to the valence band maximum. A trade-off between current and voltage is therefore necessary, since using a material with a higher band gap increases the maximum voltage attainable, but reduces the current, and the reverse is true for a material with a lower band gap. By balancing these two considerations, the optimum band gap was calculated by Shockley and Queisser to be 1.1 eV, which gives a maximum single-junction efficiency of 30%.[19] Shockley and Queisser assumed the solar spectrum to be that of a blackbody at 6000 K, but more recent calculations using the AM1.5 spectrum,[‡] give a maximum PCE of around 33% at 1.34 eV (this depends on cell temperature, whether a perfect back reflector is used, and other assumptions).[20,21] Materials with different band gaps can still be used to make high efficiency solar cells, since the maximum efficiency is above 32% within the 1.1 - 1.4 eV range, as shown in Figure 2.2.

One method of going beyond the Shockley-Queisser limit, is to employ two or more semiconducting materials absorbing different portions of the solar spectrum in a tandem

[‡] a standardized solar spectrum defined by the American Society for Testing and Materials, which takes absorption of light by the atmosphere into account

or multi-junction solar cell, thus reducing charge-carrier thermalization losses and enabling a higher PCE than is possible for a single-junction cell (see Figure 2.1).[22] Since a significant proportion of the overall cost of solar panels is made up of installation, structural and land costs, all of which scale with area, high efficiency solar cells are important in reducing the resultant price of electricity.[23] The highest efficiency multi-junction cells to date use alloys of $Ga_xIn_{1-x}As_yP_{1-y}$ in different proportions to make three or four materials with varying band gaps.[6] However, these cells are very expensive to make, meaning the resulting energy price is large despite their high efficiencies[24] and their viability is limited to spacecraft or concentrator solar cells. The band gap tunability of third generation solar cells is ideal for use in multi-junction cells, providing their efficiency and stability can be improved. A tandem solar cell which retains the low-cost production of solution-processable materials whilst achieving the efficiency boost enabled by multiple layers would have great potential to deliver large scale and affordable renewable energy.[25]

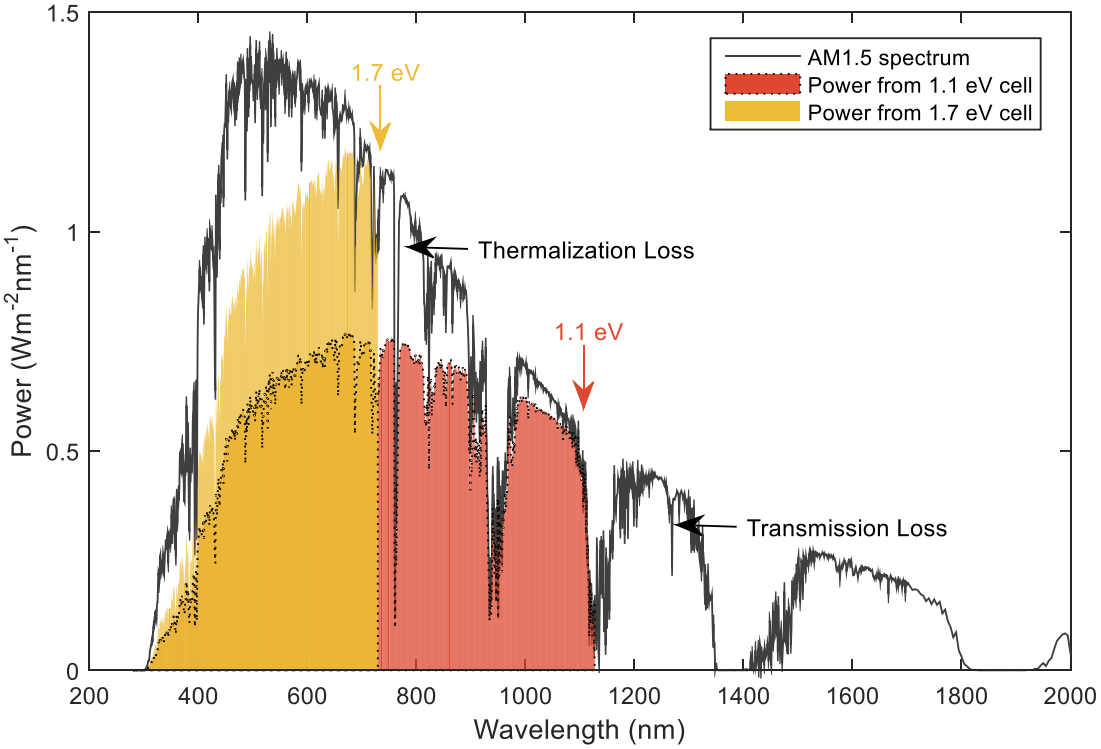

Figure 2.1. Solar spectrum reaching the surface of the Earth according to the AM1.5 standard. The shaded regions show the power available to a 1.1 eV bottom cell (red) and a 1.7 eV top cell (yellow) in a tandem solar cell, considering only losses due to transmission of low energy photons and thermalization of charge-carriers to the band gap energy of the cell. The yellow shaded region above the dotted line shows the extra power available for a tandem solar cell compared with a single junction 1.1 eV cell.

2.1.3 Perovskite solar cells

The methylammonium lead halide perovskites $CH_3NH_3PbX_3$ (where X is any of the halides I, Cl or Br) were first synthesised by Weber in 1978.[26] However it was only in 2009 when these materials were first used as a sensitizer, coated on porous titanium dioxide (TiO_2), in a dye-sensitized solar cell, achieving a PCE of 3.8%.[27] Initially there were substantial limitations to these cells, since the perovskite rapidly dissolved in the liquid electrolyte. This problem was overcome in 2012 when the electrolyte was replaced with a solid hole transporting material, spiroOMetad, resulting in a PCE of around 10%.[28,29] An interesting development came with the realisation that replacing conducting TiO_2 with non-conducting aluminium oxide (Al_2O_3) made solar cells that were just as effective, and the efficiency increased further when a capping layer of perovskite was deposited on top of the porous Al_2O_3, showing that charges could travel through the perovskite.[28] This was surprising because solution processed materials are typically disordered and have very low charge-carrier mobilities, and must therefore be used as a thin layer on a conducting material with a large surface area that can quickly extract charge. Following this revelation, planar device architectures with no porous metal oxides were also shown to produce high efficiencies, with a vapour deposited perovskite solar cell reaching a PCE of 15% in 2013.[30]

Over the last 5 years the PCE has been continually improved (see Figure 2.2),[31] with the current record for a single junction metal halide perovskite solar cell standing at 23.7%,[6] and many demonstrating PCEs over 20%.[7–10] As the electronic properties have been researched further, it has become apparent that metal halide perovskites are crystalline semiconductors more similar to the materials used in first and second generation solar cells (albeit with some unique features).[32] For example, they have a direct optical band gap[33], high charge-carrier mobilities,[34] and long charge-carrier

diffusion lengths.[35,36] The similarity of their optoelectronic properties to GaAs,[34,37] which currently holds the record for the most efficient single-junction solar cell at 29%,[6] has led to hopes that perovskites may be able to match this efficiency with further research.

Metal halide perovskites also offer the versatility and low material costs of third generation solar cells, offering a significant advantage over GaAs where the expense of the material has limited its use. The constituent elements are all earth-abundant, making them a viable option for large scale deployment.[38] Lead halide perovskites also have surprisingly benign defect chemistry,[39,40] meaning expensive purification processes are not necessary to produce a working device. They can be fabricated in a number of different ways, either from solution such as spray coating and inkjet printing or by vapour deposition methods.[41,42] Due to the large compositional parameter space which will be discussed in Section 2.2.1, the band gap can be tuned over the entire visible spectrum and beyond, extending from 1.2 to 3.0 eV through alloying of the metal cation (Pb^{2+}, Sn^{2+}),[43,44] A-cation ($HC(NH_2)_2^+$ (FA), $CH_3NH_3^+$ (MA), Cs^+)[45–47] and halide (I^-, Br^-, Cl^-).[47–51] This makes them ideal candidates for multi-junction solar cells. All-perovskite tandem cells are still in the early stages of development, but have already reached a record 4-terminal efficiency[52] of 23% and 2-terminal efficiency[53] of 18.5%. In addition, the compositions with higher band gaps can be used in tandem with silicon to boost the efficiency of widely available solar panels at an acceptable cost. This offers a promising pathway for commercialisation, with the record PCE currently set at 28%.[54]

The bottom cell in all-perovskite tandem cells requires a small band gap, which can be achieved using a tin-based perovskite material. However, the best PCEs for tin perovskite solar cell are around 6%,[55–57] with a new record of 8% in 2017[58], still far below the efficiency of lead perovskite solar cells. The stability is also a problem, with

the material degrading on contact with air. As material quality has improved, the stability has also improved, with $FASnI_3$ single crystals reportedly unchanged after being exposed to ambient air for one month.[59] Alloying tin and lead and the cation also improves both stability and efficiency.[44,60] Consequently the development of a stable and efficient low band gap perovskite containing tin is not an unreasonable goal.

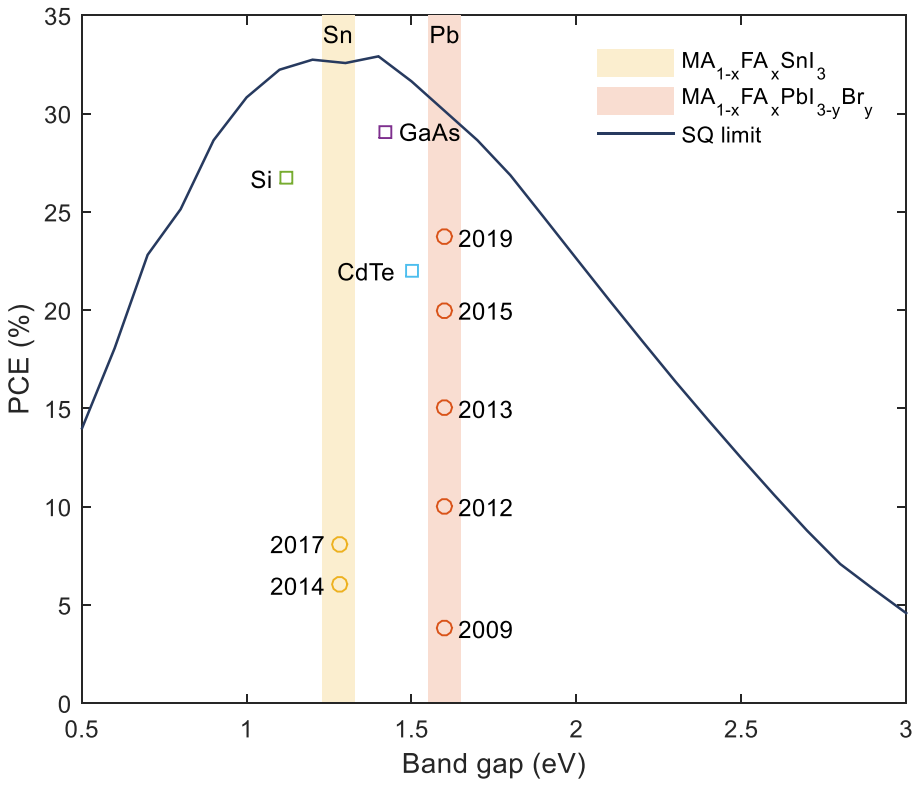

Figure 2.2. Shockley-Queisser limit assuming AM1.5G illumination and no back reflector.[20] The shaded regions show the band gap range of commonly used compositions for lead and tin based perovskites. Circles show solar cell efficiency records for Sn-based (yellow)[58,61] and Pb-based (red)[6,7,27,28,30] perovskites in each year marked. Squares show current efficiency records for Si (green) CdTe (blue) and GaAs (purple).[6]

2.2 Perovskite structure

This section will outline the chemical structure of perovskites, their composition and how the structure changes with temperature.

2.2.1 Composition

Metal halide perovskites are comprised of connected octahedra with a metal ion such as tin (II) or lead (II) at the centre, surrounded by halide ions – iodine, chlorine or bromine.[62,63] This network of octahedra largely determines the band structure, with the metal s-orbitals and halide p-orbitals contributing to the conduction and valence bands.[64,65] A third ion, the 'A-cation', which can be organic such as methylammonium ($CH_3NH_3^+$) or formamidinium ($HC(NH_2)_2^+$), sits inside a 'cage' of 8 metal-halide octahedra (see Figure 2.3).

The large range of ions that can be incorporated in the perovskite structure, and the fact that they can be alloyed, gives a huge parameter space to explore which enables the physical and optical properties of these materials to be adjusted to desired values.

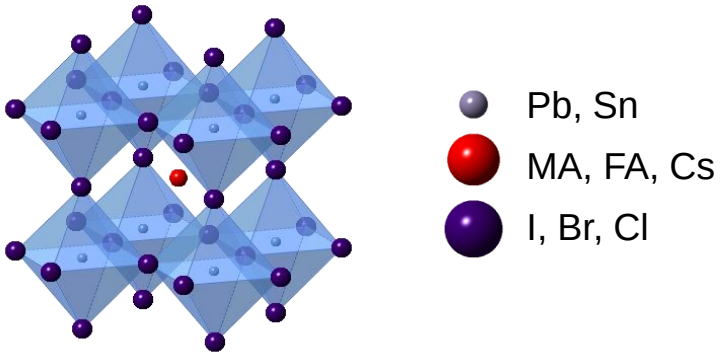

Figure 2.3. Chemical structure of a cubic perovskite. Metal (grey) and halide (purple) ions form a network of octahedra.

2.2.2 Structural phases

Perovskites can exist in several possible phases including cubic, tetragonal and orthorhombic, which can be classified by the tilt of the metal-halide octahedra (illustrated in Figure 2.4).[66] They tend to exhibit at least one phase transition to a lower symmetry structure as their temperature is lowered.[67–69] The structural phase at room temperature depends on the size of the three ions, and is approximately determined by the Goldschmidt tolerance factor, although there have been attempts to deduce improved tolerance factors that give more accurate predictions.[70]

In $CH_3NH_3PbI_3$ the transition from cubic to tetragonal (α to β) occurs when cooled below 330 K and the transition from tetragonal to orthorhombic (β to γ) occurs at 160 K.[71] In these transitions the lead-iodide bonds are distorted, but no bonds are broken. The unit cells of the β and γ phases are $2\sqrt{2}$ times bigger than the cubic unit cell. In certain perovskites, such as $FAPbI_3$ and $CsPbI_3$, a fourth non-perovskite structure (δ) can be accessed, where some lead-iodide bonds are broken.[72] This is often called the 'yellow phase' due to its colour, as compared to the black or dark brown perovskite phase.

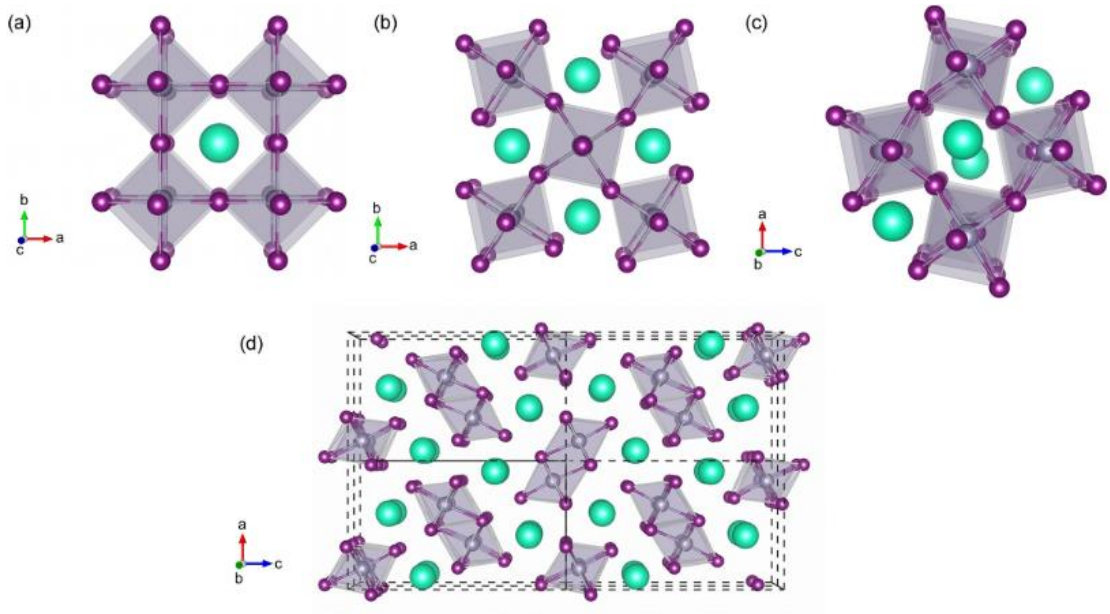

Figure 2.4. Diagram showing the structural phases of metal halide perovskites. The halide ions are shown in purple, metal ions in grey at the centre of the purple octahedra, and the organic cations are shown as green spheres. The four phases are (a) cubic phase, (b) tetragonal phase, (c) orthorhombic phase, (d) 'yellow' phase. Reprinted figure with permission from ref. 73 (http://dx.doi.org/10.1103/PhysRevB.91.144107). Copyright 2015 by the American Physical Society.

2.3 Band gap

The rest of this chapter will focus on the optoelectronic properties of metal halide perovskites – their band gap and charge-carrier recombination. I will discuss some theory relevant to all semiconductors, where it is applicable to the interpretation of my experimental work, and review the literature surrounding perovskites.

The band gap is the most fundamental property of a semiconductor, and crucial to understanding its other properties. The band structure is affected by both the elements used and their positioning in the crystal lattice, and can be considered in terms of the electronic orbitals of the individual atoms and how they interact to form electronic bands. Most calculations of the band structure rely on the computational method of density functional theory (DFT),[74,75] or methods based on DFT such as GW theory.[76,77] Calculating an accurate band gap by these methods is not trivial, requiring correct inclusion of the relevant effects (spin orbit coupling, relativistic effects etc.) and a good choice of functionals.[74]

As mentioned in Section 2.2.1, it is the metal s-orbitals and halide p-orbitals which contribute most to the conduction and valence bands in metal halide perovskites.[64,65] Changing the metal and halide used therefore has the most impact on the size of the band gap. Whilst alloying the halide changes the band gap in a linear fashion, alloying the metal ion results in a large band gap bowing parameter, which is discussed in Section 2.3.1. The A-cation is less important to band structure calculations than the metal-halide octahedra, but can change the band gap by tilting the octahedra or by changing the size of the lattice parameter.[46] In lead halide perovskites, increasing the cation size from caesium, to methylammonium to formamidinium, tilts the octahedra,[46] which changes the overlap of the orbitals and subsequently reduces the band gap.[50]

However for tin perovskites, increasing the cation size expands the lattice parameter[46] and the opposite trend is true, with $FASnI_3$ having a larger band gap than $CsSnI_3$.[69]

2.3.1 Band gap bowing

It is common for semiconductor alloys to display some degree of band gap bowing, with the band gap bowing parameter *b* being defined by the following equation:[78]

$$E(x) = E_1 x + E_2 (1-x) + b\, x\, (1-x)$$

Equation 2.1

where $E(x)$ is the band gap energy of the mixed composition comprising material 1 with band gap energy E_1 and material 2 with band gap energy E_2, and x is the proportion of material 1. The first two terms represent a linear change in band gap with composition between the two end points, and the third term captures a quadratic deviation from linearity. Equation 2.1 shows that the maximum deviation ΔE occurs at $x = 0.5$ and is given by $\Delta E = b/4$ (illustrated in Figure 5.5).

For traditional inorganic semiconductors, the bowing parameter *b* is usually small compared to the size of the band gap,[79] with only slight deviation from the linear behaviour often referred to as 'Vegard's Law',[80] which was however originally stated for lattice parameters rather than band gaps. There are a handful of semiconductors with bowing parameters large enough for the mixed compositions to have lower band gaps than either of the end compositions, including GaN_xAs_{1-x}, $GaAs_xSb_{1-x}$, $CdSe_xTe_{1-x}$ and ZnS_xTe_{1-x}.[79,81] For some of these alloys, the band gap bowing is thought to be caused by the local environment around the alloyed atom, meaning that averaging the properties of the alloy atoms (the 'Virtual Crystal Approximation') is not valid. Extended X-ray absorption fine structure (EXAFS) measurements show that for pseudo-binary alloys such as those listed above, the individual bond lengths are often closer to those of the un-alloyed materials, rather than adopting an intermediate value, illustrated in Figure 2.5. The mismatch resulting from the different sizes of the alloyed atoms is then

accommodated by local changes to bond angles, which results in properties that cannot be described by considering the global structure where the bond lengths take an average value and the angles are all the same.[82,83] These effects can be calculated using density functional theory, but since the local placement of the atoms is important, large supercells are required, making it computationally expensive to model.

In certain cases (usually where the size or electronegativity of the alloy atoms differ greatly from each other) band gap bowing can be described by considering an atom as an impurity that forms a new localized energy level which, if sufficiently close in energy, mixes with the conduction or valence band to form two new bands, illustrated in Figure 2.6.[84] The bowing can then be modelled by a simple 'band anti-crossing' (BAC) equation,[84] interpolated between the two impurity limits[85] and in some cases producing highly non-parabolic bowing, such as in such as for GaN_xAs_{1-x}.[86]

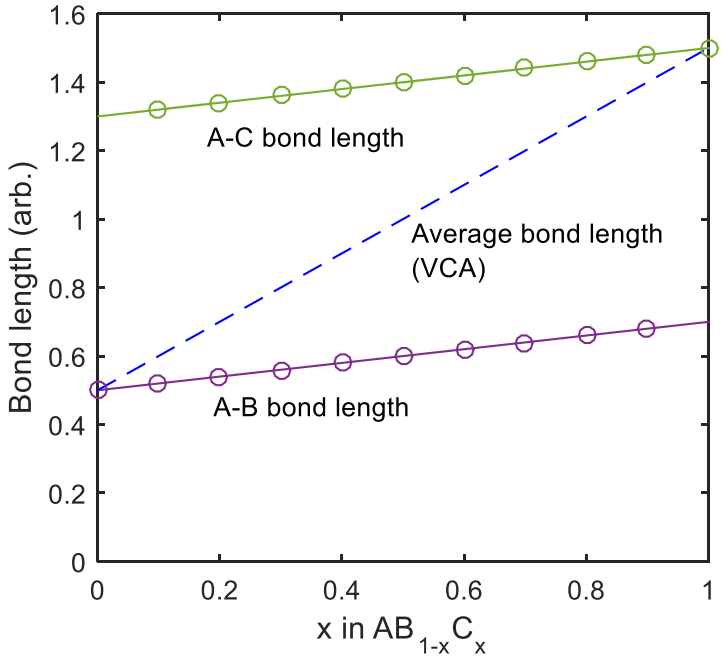

Figure 2.5. Illustration of the Virtual Crystal Approximation (VCA) compared to actual bond lengths in a semiconductor alloy. Based on data from ref. 83.

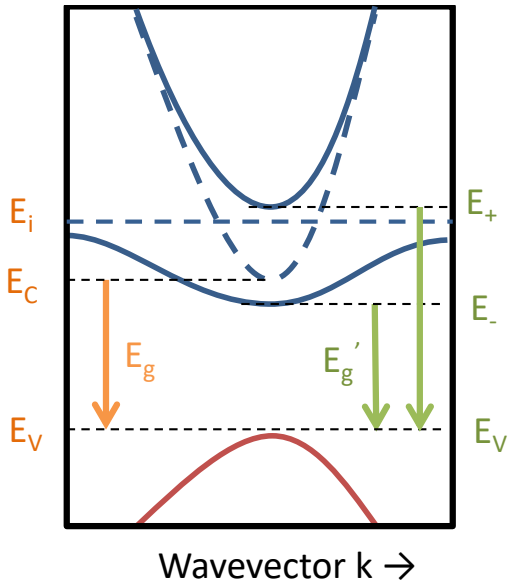

Figure 2.6. Diagram of Band Anti-Crossing. On the left, the band gap E_g of the parent composition is shown in orange between the conduction and valence band. The valence band is shown in red (with maximum E_V) and the conduction band as a blue dashed line (with minimum E_C). Adding another element introduces impurity level E_i. The solid lines show how the bands mix to form two new bands with energy minima at E_- and E_+. The new transitions are shown on the right hand side in green, and the band gap of the alloy is smaller than the unalloyed material.

Alloyed lead-tin perovskites have been found to exhibit a large band gap bowing parameter, enabling alloys to have lower band gaps than either of the 'parent' compositions $APbX_3$ or $ASnX_3$. This is in contrast to the linear change in band gap observed for metal halide perovskites with compositional changes in A-cation[45] and halide anion[49]. There is little understanding of the cause of band gap bowing in metal halide perovskites at the present time, and reports disagree on both the origin[44,87] and magnitude of the effect. Hao[43], Zhao[88], Anaya[89] and Liu[90] all report bowing in $MAPb_{1-x}Sn_xI_3$ with a minimum band gap of just below 1.2 eV at around 80% tin content, determined from optical absorbance or EQE measurements. Yang[91] reports a minimum of 1.27 eV at 75% tin, Im[87] and Stoumpos[92] find a minimum band gap of 1.1 eV at around 50% tin content, while Ogami finds the minimum band gap to be 1.1 eV at 100% tin with little bowing. For $FAPb_{1-x}Sn_xI_3$, Eperon[44] and Prasanna[46] report a minimum band gap of 1.2 and 1.25 eV respectively at around 60% tin content.

2.3.2 Temperature dependence

The band gap of metal halide perovskite semiconductors has been shown to increase as temperature is increased, which is observed as a blue-shift in photoluminescence (PL) maximum and absorption onset[71,93–95]. This finding is contrary to the usual behaviour of semiconductors for which the band gap decreases as the temperature increases (negative dE_g/dT), according to the empirical Varshni formula.[96] Although one might intuitively expect this decrease (red-shift) as the lattice expands, in fact the lattice expansion is usually a relatively small contribution, and can increase or decrease the band gap with temperature as determined by detailed band structure calculations.[97]

The main contribution to the change in band gap with temperature is the influence of phonons i.e. the change in band gap caused by the dynamic displacement of atoms due to thermal lattice vibrations (rather than the phonon anharmonicity responsible for

lattice expansion).[98] Phonons usually reduce the band gap as the temperature is raised, but can increase it, and there can be multiple phonons with opposite effects on the band gap in the same material, resulting in complex temperature dependence.[99]

For metal halide perovskites it was initially proposed that the linear increase in band gap with increasing temperature is due to the cancellation of phonon terms with opposite effect on the band gap, leaving lattice expansion as the dominant contribution.[93] More recently, calculations have shown that the phonon anharmonicity is large, possibly making the lattice expansion explanation plausible without the need for other terms cancelling.[100] As the lattice constant is increased, the valance band maximum decreases linearly because of the reduced overlap of the Pb-6s and I-5s antibonding orbitals, therefore increasing the band gap.[64] However another study has identified that the Pb-I-Pb bond bending phonon mode increases the band gap and suggests this to be the main contribution.[101]

In addition to the linear change in band gap, phase transitions result in a discontinuity in the band gap at the transition temperature, with both the PL and the absorption edge jumping to a higher energy.[71,94,102]

2.3.3 Quantum Confinement

When the smallest dimension of a material is of the same order of magnitude as the exciton Bohr radius or free electron/hole de Broglie wavelength, typically a few nanometres, the observed band gap is increased by quantum confinement. As the dimensions are reduced, the allowable values of kinetic energy transition from a continuum to discrete levels. In this thesis, thin layers of perovskite material will be studied, which may be confined in one dimension. The simplest equation for the discrete levels in a quantum confined system is the 'particle in a box' solution to the Schrodinger equation, which applies to free electrons and holes in a confined space

considered as an infinite potential well. If the binding energy is large enough for there to be a significant presence of excitons at room temperature, then the equation must be modified to treat excitons rather than separate electrons and holes, known as the weak confinement regime.[103] A full analysis is not required for the purposes of this thesis, but in all of these scenarios, the equation for the energy of the lowest transition has the approximate form[103]

$$E = E_g + \frac{B}{d^2}$$

Equation 2.2

where E_g is the band gap, d is the height of the film and B is a constant.

At room temperature, the exciton binding energy in bulk $MAPbI_3$ is approximately 5 meV[33,104,105] (corresponding to a Bohr radius of ~5 nm), meaning excitons spontaneously dissociate and only free electrons and holes need to be considered. However for thinner material, the exciton binding energy will increase due to increased Coulomb interaction, both as a direct result of the proximity of electrons and holes, and also due to the change in effective dielectric constant which occurs when the film thickness is less than the Bohr radius, sometimes referred to as dielectric confinement[106] or the image charge effect.[107] This effect can be quite substantial with reports of a binding energy as high as 360 meV for a single layer of a two dimensional perovskite ($(C_6H_{13}NH_3)_2PbI_4$) with a well width of 6 Å,[107]

Quantum confinement effects have been observed in 3D perovskite nanocrystals.[108–111] Wavelengths as low as 630 nm have been reported for colloidal nanocrystals of $MAPbI_3$ with a diameter of 2.6 nm.[110] Perovskite nanocrystals can also be made by templating in nanoporous silicon[108,109] or alumina[109] which show large shifts in PL wavelength with size.[108]

2.4 Defects

Defects are essential to semiconductor physics, enabling controlled doping by intentional inclusion of another element, which is the basis for p-n junctions. However, unintentional defects are a serious hindrance to performance, either through unwanted doping if the defect level is shallow, or by creating recombination centres if the defect level has an energy close to the middle of the band gap. Defects can be of many types, including the presence of foreign elements (impurities), interstitial ions, native ions on the wrong lattice site, vacancies in the lattice and dislocations.[112,113]

2.4.1 Doping

Doping is caused by shallow defects which contribute electrons or holes with energy levels close enough to the conduction or valence band for charge-carriers to be thermally excited into the band ($E_b < kT$). A well-known example of intentional doping is phosphorous doping of silicon – since phosphorous has one extra valence electron compared with silicon, it is a donor ion and contributes 1 electron for n-doping per atom which has localized hydrogen-like energy levels just below the conduction band minimum. Spontaneous doping occurs when defects in the semiconducting crystal act as donor or acceptor ions.[114]

For $MASnI_3$, spontaneous p-doping has been linked to poor device performance due to very fast charge-carrier recombination. Several studies have shown that both $MASnI_3$ and $CsSnI_3$ can become p-doped during crystal formation with dark hole densities (p_0) ranging from 10^{14}-10^{19} cm^{-3} depending on preparation method.[56,57,69,115–117] This leads to fast recombination of photo-excited electrons with doped holes (see Section 2.5.1) which may limit both the charge-carrier extraction and the voltage.[55,115,116,118]

There has been some confusion in the literature over the origin of the p-doping. Unlike lead which always forms Pb^{2+} ions, tin can easily form compounds in both the 2+ and 4+ oxidation state. This tendency to oxidize has been linked to the instability of tin-based perovskites in air.[119] However, if it were possible to substitute Sn^{2+} for Sn^{4+} as a dopant this would n-dope the material, and is therefore not acting as an acceptor ion responsible for p-doping as some have claimed.[120] Instead, the presence of Sn^{4+}, which can be detected by X-ray photoelectron spectroscopy (XPS),[121] indicates that tin vacancies have been formed.[115] Indeed, the stable compound Cs_2SnI_6 can be formed from $CsSnI_3$ when half the tin ions are removed and all remaining tin ions are therefore in the 4+ oxidation state.[120] It is tin vacancies then that are most likely to be the defects responsible for p-doping.[116,122,123] First-principles calculations for $CsSnI_3$ have suggested that tin vacancies have a low formation energy, meaning they are likely to be present when the material is fabricated.[116,117,124] Exposure to air can create further defects by parts of the perovskite crystal reacting with oxygen to form SnO_2 and SnI_4.[119] Calculations have also shown that the energy level of a tin vacancy is close to the valence band edge making it easy to ionize, with each vacancy able to contribute two holes, thus p-doping the material.[124]

In lead halide perovskites, spontaneous doping is thought to be either low or compensated (with equal numbers of donors and acceptors), with various Hall effect measurements showing densities of 10^9-10^{14} cm^{-3}.[112]

2.4.2 Recombination centres

As well as doping a material, defects can act as recombination centres, acting as a pathway for non-radiative recombination, which will be discussed in Section 2.5.2. Defects with energy levels lying deeper within the band gap have faster recombination rates and are therefore more detrimental to solar cell performance.[125] One of the reasons

for the success of metal halide perovskite solar cells is that they are surprisingly defect tolerant, meaning the defects do not contribute deep levels that would be harmful to performance.[39] Defect levels in $MAPbI_3$ have been studied by first principles calculations which have found that defects with deep levels have high formation energies whereas defects with shallow levels have low formation energies.[112] Some have suggested that iodine interstitials are most likely to be problematic, but a recent study has shown that these can be deactivated under mild oxidation conditions or by mixing in another halide.[126]

2.4.3 Charge-carrier scattering

The periodicity of a perfectly regular lattice results in delocalized electrons with high conductivity, described by Bloch waves. All defects cause a disruption to this periodicity, causing charge-carriers to scatter. Scattering both lowers the conductivity of the semiconductor[34] and increases the energy spread of the charge-carriers. As a result, the PL emission is broadened inhomogeneously.[127] The other main contribution to charge-carrier scattering is interaction with phonons. This is unrelated to defects and is an intrinsic property of the material which causes homogeneous broadening.[127]

Since charge-carrier scattering effects the PL linewidth, information about the nature of defects can be learnt from the temperature dependent linewidth, which can be modelled by the equation:[127]

$$\Gamma(T) = \gamma_{ac}T + \gamma_{LO} / (e^{E_{LO}/kT} - 1) + \gamma_{imp}\, e^{-E_b/kT} + \Gamma_0$$

Equation 2.3

Here, k and T refer to the Boltzmann constant and the temperature of the lattice, and the terms (in order of appearance) arise from scattering with acoustic phonons (coupling strength γ_{ac}), optical phonons of energy E_{LO} (coupling γ_{LO}), donor/acceptor impurities with ionization energy E_b (coupling γ_{imp}) and a temperature-independent broadening term Γ_0 arising e.g. from energetic disorder.

At high temperature both phonon terms give a linewidth which is linear with temperature, whereas the ionized defect term has a sublinear temperature dependence, as illustrated in Figure 2.7.

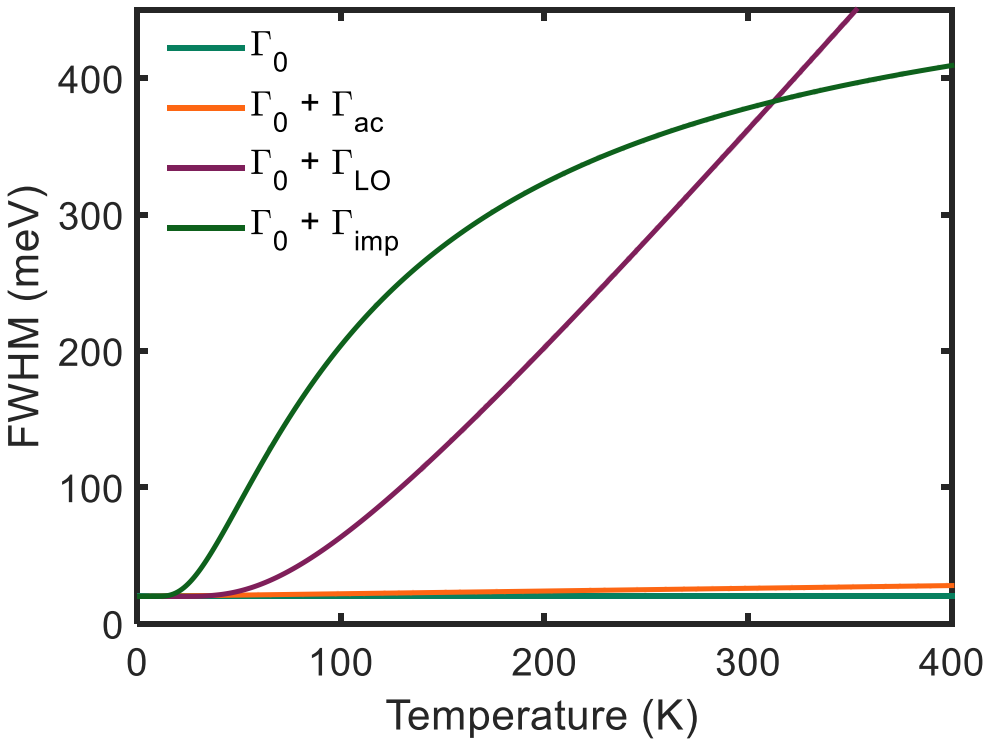

Figure 2.7. Temperature dependence of the four terms in the line width model. Values are chosen to be typical for CdTe: $\Gamma_0 = 20$ meV, $\gamma_{ac} = 0.02$ meV/K, $\gamma_{LO} = 400$ meV, $E_{LO} = 20$ meV, $\gamma_{imp} = 500$ meV, $E_b = 100$ meV.

2.5 Charge-Carrier Recombination

In a solar cell, charge-carrier recombination competes with charge extraction (providing a current), and also determines the quasi-Fermi-level splitting which is related to the open circuit voltage.[37] Understanding recombination is therefore fundamental to optimizing solar cell operation. There are many types of charge-carrier recombination mechanisms in semiconductors, the most important of which are shown in Figure 2.8. The charge-carrier density, including contributions from all types of recombination, can be approximately modelled by the equation[34,128,129]

$$\frac{d(\Delta n)}{dt} = G - k_1 \Delta n - k_2 \Delta n^2 - k_3 \Delta n^3$$

Equation 2.4

Here G is the rate of charge-carrier generation (e.g. by solar illumination), Δn is the photo-generated charge-carrier density, k_1 is the monomolecular recombination rate constant which typically reflects trap-mediated recombination (unless there is significant excitonic recombination), k_2 is the bimolecular recombination rate constant which typically reflects band-to-band recombination, and k_3 is the trimolecular recombination rate constant which typically reflects Auger recombination.

The rate constants in vapour deposited $MAPbI_3$ (with a small addition of chlorine)[130] and solution-processed $FAPbI_3$[131] have been measured using Terahertz Spectroscopy and found to be approximately $k_1 \sim 10^7 s^{-1}$, $k_2 \sim 10^{-10} cm^3 s^{-1}$ and $k_3 \sim 10^{-29} cm^6 s^{-1}$, whereas the same measurements for $MASnI_3$[55] give $k_1 \sim 10^{10} s^{-1}$, $k_2 \sim 10^{-9} cm^3 s^{-1}$.

The higher order terms become increasingly important as the intensity of the incident light, and therefore Δn, is increased. In the experiments performed in this thesis, Δn is not large enough for Auger recombination to be significant,[132] so from here on I will discuss only trap-mediated and band-to-band recombination mechanisms and the Auger recombination term can be dropped from Equation 2.4. In this thesis I will measure the

PL intensity over time in the dark after initially using a laser pulse to generate a photoexcited charge-carrier density of Δn_0. Under these conditions, Equation 2.4 can be solved to give

$$\frac{\Delta n(t)}{\Delta n_0} = \frac{K}{(K+1)e^{k_1 t} - 1}$$

Equation 2.5

where t is the time after excitation with a laser pulse and $K = k_1/(k_2 \Delta n_0)$ is a dimensionless parameter. Figure 2.9 shows the charge-carrier density Δn over time after excitation with a laser pulse. The relative values of k_1 and k_2 determine how 'stretched' the curve is, as described by Equation 2.5.

The overall recombination rate, together with the charge-carrier mobility, determines how far a charge-carrier is likely to travel before recombination. This is known as the charge-carrier diffusion length.[34] The distance between the point in the solar cell where charge-carriers are generated (across the semiconductor bulk), and the point of extraction (at the semiconductor interface), should be smaller than the diffusion length to maximise the probability of extraction. Thus making the absorber layer thinner tends to improve extraction, whereas making it thicker improves absorption of incident light. $MAPbI_3$ has a high absorption coefficient, and a long charge diffusion length on the micrometre scale,[35,130] meaning that full absorption and full extraction (assuming ideal contacts) are both easily achievable.

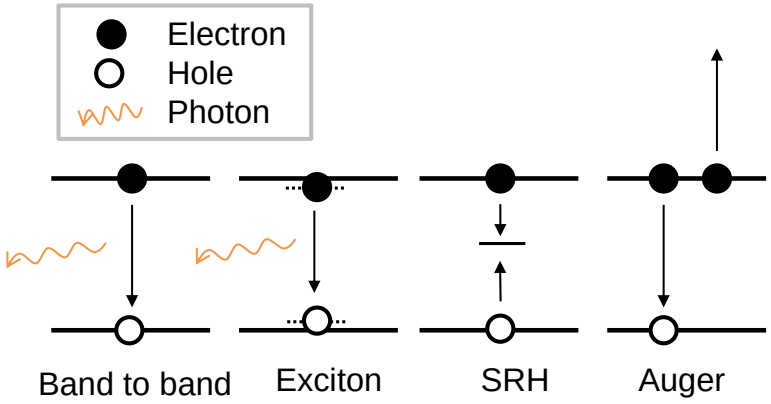

Figure 2.8. Diagram of charge-carrier recombination mechanisms. The vertical direction corresponds to increasing energy and the horizontal lines show available energy levels. Transitions showing the emission of a photon indicate radiative recombination mechanisms.

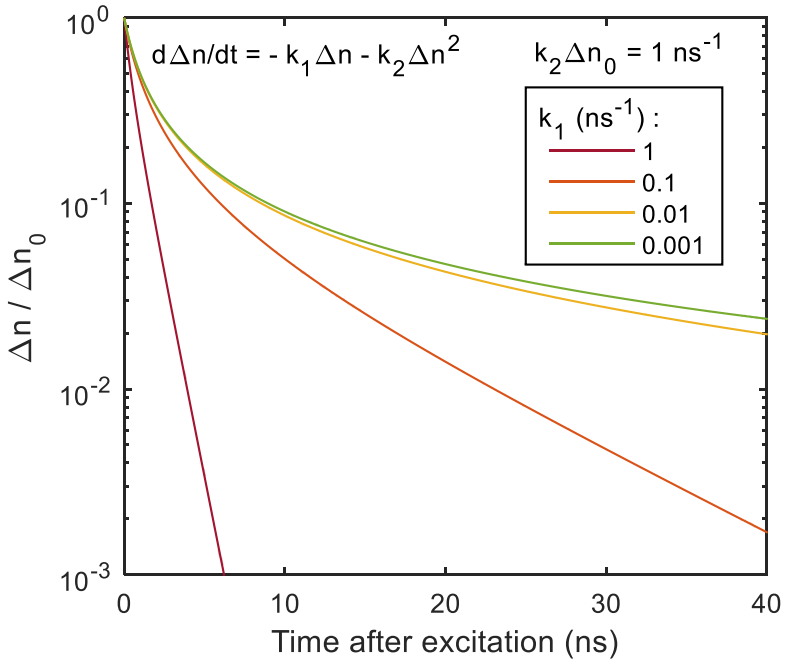

Figure 2.9. Simulation of the charge-carrier density decay curves for a range of values of k_1. For a typical room temperature value of $k_2 = 10^{-10}$ ns^{-1}cm^3, a high initial carrier density of $\Delta n_0 = 10^{19}$ cm^{-3} is required to give $k_2\Delta n_0 = 1$ ns^{-1}.

2.5.1 Band-to-band recombination

When a semiconductor is under zero bias and in steady state conditions, the rate of generation of charge-carriers must be equal to the rate of their recombination in order to maintain thermal equilibrium. In an ideal defect-free intrinsic semiconductor under illumination, this necessary recombination occurs through photoexcited electrons in the conduction band recombining with photo-excited holes in the valence band, emitting one photon per recombination event with energy equal to the band gap (photoluminescence). If the charge-carriers are free (i.e. the exciton binding energy is smaller than the thermal energy), the rate of recombination is proportional to the density of photo-excited electrons and photo-excited holes, which are equal to each other since they are generated in pairs: $\Delta n \Delta p = \Delta n^2$.[34] Alternatively if there is a significant population of excitons, the rate is proportional to the number of excitons, equal to Δn, and photons are emitted at the energy of the band gap minus the exciton binding energy. For the perovskites considered in this thesis, the exciton binding energy is small enough for carriers to be considered as free charges.[104,133,134] Band-to-band recombination in $MAPbI_3$ has been shown to be the inverse process of absorption.[33] As temperature is decreased, the thermal spread of the excited electron and hole populations narrow, which subsequently increases band-to-band recombination leading to a higher value of the rate constant k_2 at low temperature.[33,71]

Since band-to-band recombination (the only necessary recombination mechanism) results in the emission of photons as described above, a mark of a good semiconductor for use in a solar cell is a high photoluminescence quantum efficiency (PLQE).[37] A PLQE of 100% is attained when one photon is emitted for every photon absorbed. Thus a lower PLQE indicates the presence of at least one non-radiative recombination mechanism, which could lower the efficiency of the solar cell.

Doping a semiconductor influences the rate of band-to-band recombination by increasing the density of charge-carriers available. In the case of p-doping, the density of holes available for recombination is equal to the doping density p_0 plus the photo-generated charge-carrier density Δn. Equation 2.4 (neglecting trimolecular recombination) then becomes

$$\frac{d(\Delta n)}{dt} = G - k_1^{nr}\Delta n - k_2^r(p_0 + \Delta n).\Delta n$$
$$= G - (k_1^{nr} + k_1^r)\Delta n - k_2^r\Delta n^2$$

Equation 2.6

where the superscripts r and nr have been introduced to mean radiative and non-radiative recombination, and k_1^r is defined as $k_1^r = p_0\, k_2^r$ since the recombination of electrons with a fixed density of doped holes is pseudo-monomolecular and can be treated as a radiative contribution to $k_1 = k_1^r + k_1^{nr}$. Although lead-based perovskites are thought to be close to intrinsic semiconductors, the case of recombination in a p-doped semiconductor is relevant to the study of tin-based perovskites. Previous studies have shown significant contributions from a monomolecular radiative rate in $MASnI_3$, which has been attributed to the recombination of photoexcited electrons with holes arising from spontaneous doping,[135] as discussed in Section 2.4.1.

2.5.2 Trap-mediated recombination

The trap-mediated recombination of charge-carriers in semiconductors is generally described by the Shockley-Read-Hall (SRH) model.[125] In most cases, the common assumption of a constant decay rate k_1 (as in Equation 2.4) is a good approximation to SRH recombination. This approximation is applicable to many situations such as extrinsically doped semiconductors, and leads to mono-exponential decay dynamics. However the full SRH formula has a more complex dependence on the photoexcited carrier density Δn

$$U_{SRH} = \frac{(p_0 + n_0 + \Delta n)}{\tau_n(p_0 + \Delta n + p_1) + \tau_p(n_0 + \Delta n + n_1)} . \Delta n$$

Equation 2.7

where n_0 and p_0 are equilibrium electron and hole densities (from doping), n_1 and p_1 are the electron/hole densities in the conduction/valence band when the Fermi level is equal to the energy level of the trap, and τ_n and τ_p are the minority carrier lifetimes of electrons and holes respectively. Equation 2.7 is derived using the assumption that the density of electrons in the traps remains in thermal equilibrium, which is valid either in steady state or when one of n_0, p_0, n_1 or p_1 are large compared to the total trap density.[125,136] The case when this is not valid is discussed in 2.5.4.

The two cases applicable to metal halide perovskites are that of a p-doped semiconductor, as is the case for tin-based perovskites, and that of an intrinsic semiconductor with shallow traps, as is the case for lead-based perovskites.[137,138] In the first case, Equation 2.7 reduces to[125]

$$U_{\mathrm{SRH}} = 1/\tau_n \Delta n,$$

Equation 2.8

which is equivalent to the non-radiative term in Equation 2.6 with $k_1^{nr} = 1/\tau_n$. In the second case, if it is assumed that the traps are located close to the conduction band, Equation 2.7 becomes

$$U_{SRH} = \frac{\Delta n}{(\tau_n + \tau_p)\Delta n + \tau_p n_1} . \Delta n$$

Equation 2.9

The equation for traps located close to the valence band is equivalent but with n and p swapped. This means that the commonly used rate equation (Equation 2.4) is not strictly applicable to lead-based perovskites. Several scenarios are explored in Appendix A where Equation 2.7 is used to simulate decay of a photoexcited charge-carrier density Δn over time.

2.5.3 Temperature dependent trap-mediated recombination

The rate of SRH recombination depends on the charge-carrier densities and on the lifetimes of the trapped electrons or holes. The temperature dependence of the charge-carrier densities can be calculated from Fermi-Dirac statistics – the densities reduce as the temperature is lowered. The SRH lifetimes, corresponding to the rates at which electrons and holes are trapped, are determined by the physical mechanism of recombination and can therefore display a variety of temperature dependent behaviours. For clarity I will discuss the mechanisms in terms of electron trapping, but the mechanisms are equivalent for hole trapping.

The most common mechanism in traditional semiconductors is multi-phonon recombination, during which a trapped electron moves to a lower energy level by converting its energy into several phonons.[139] There is an activation energy associated with this process because energy and momentum conservation requires a number of particular phonons to be absorbed, in addition to those emitted.[140] The temperature dependence of the process depends on conditions such as the charge of the trap, whether the transition is between localized states or bands, and the possibility for quantum tunnelling through the energy barrier, but in all cases the rate is expected to increase with temperature according to a power law or exponential rise, which has been experimentally observed in several semiconductors.[141]

An alternative mechanism is cascade capture, where a charged trap has hydrogen-like excited states that an electron can cascade through by emitting a single phonon each time.[142] In contrast to the multi-phonon process, the rate decreases with increasing temperature, since the electron is more likely to be thermally excited out of the first level.[141,142] The recombination rate is also expected to decrease in the presence of a continuous distribution of traps for the same reason.[143,144]

As another channel (though one not included in the simple SRH model), trap-assisted Auger recombination may operate, during which an electron loses its energy to another electron.[145] Trap-assisted Auger recombination is only weakly dependent on temperature.[145]

Finally, an electron can emit a photon when it is captured, which would contribute to the PL spectrum at an energy lower than the band gap. This process is also weakly dependent on temperature, but tends to be slower than the other mechanisms.[141]

2.5.4 Charge-carrier trapping

There has been some discussion in the literature as to whether the process of populating traps is important to the charge-carrier dynamics of metal halide perovskites.[146,147] This implies that the trapped electron (or hole) density does not remain in thermal equilibrium with the free charge-carrier density, which can occur when the system is not under steady state conditions and the total trap density is large compared with n_0, p_0, n_1 and p_1.[125,136] In this case, transient measurements may initially be determined by the rate at which traps are populated, rather than the rate of recombination, until the free and trapped populations reach thermal equilibrium. The initial population of traps creates an imbalance in free carrier densities, e.g. if electrons are trapped much faster than holes, Δn will be depleted as electrons populate traps, whilst Δp initially remains approximately constant, thereby photodoping the semiconductor.[125,136] The trapping lifetime (dominated by fast electron trapping) is then much shorter than the SRH recombination lifetime (dominated by the slower hole trapping).

For small photoexcitation, the free charge-carrier density follows a bi-exponential decay, with the shorter lifetime corresponding to the filling of traps and the longer

lifetime corresponding to recombination. Since it is the steady state recombination which is important in normal solar cell operation, it is the longer lifetime given by the bi-exponential decay that is most relevant.[147] However if the photoexcited free electron density is large enough ($\Delta n > n_0+n_1+N_0$ where N_0 is the density of empty electron traps) the decay will not be exponential.[136]

2.5.5 Radiative efficiency

The radiative efficiency of a material is the ratio of the number of charge-carriers recombining radiatively to the number of charge-carriers generated. When measuring the photoluminescence, it is also known as the PL quantum efficiency, or quantum yield (PLQE). In steady state, this is given by

$$\varphi(T) = \frac{U_r}{G} = \frac{U_r}{U_r+U_{nr}} = \frac{1}{1+R(T)}$$

Equation 2.10

where U_r is the radiative recombination rate and U_{nr} is the non-radiative recombination rate, where both are dependent on the charge-carrier density Δn and can also be dependent on the temperature T. G is the generation rate, which in steady state is equal to the total recombination rate, and R is the ratio U_{nr}/U_r. I discuss an analogous approach for pulsed-excitation in Appendix B.

Measurements of the PLQE are useful in conjunction with time-resolved PL measurements to determine whether it is the radiative or non-radiative recombination rate that is changing. Eliminating recombination by mechanisms other than radiative band-to-band recombination is important when maximising the efficiency of a solar cell.

The temperature dependence of the PLQE can be particularly useful in understanding charge-carrier recombination mechanisms. A common approach[102,148–151] to characterising temperature dependent PL intensities is to fit the equation

$$\frac{I(T)}{I(0)} = \frac{1}{1 + A\,exp\left(-\frac{E_a}{k_B T}\right)}$$

Equation 2.11

which is equivalent to Equation 2.10 when the intensity at a temperature of 0 K corresponds to a radiative efficiency of 100%, and when the ratio R shows a temperature activated behaviour with E_a being the activation energy.

In excitonic materials, the radiative rate U_r is proportional to $\exp(E_b/kT)$, where E_b is the binding energy of the exciton, since thermal dissociation of excitons reduces the rate of exciton-mediated electron-hole recombination. The activation energy in Equation 2.11 can therefore be equated with the exciton binding energy. In this scenario, the charge-carrier lifetime reduces as the temperature is lowered due to the increased rate of radiative recombination.

In metal triiodide perovskites, the exciton binding energy is small (approximately 5 meV at room temperature for $MAPbI_3$)[33,104,105] and therefore this is not the main contribution to the temperature dependence of the radiative efficiency. However the radiative efficiency still follows the form of Equation 2.11.[102,150,151] Several studies have used this method to extract a binding energy for metal halide perovskites and found values much larger than those measured by direct methods,[102,150,151] showing the inadequacy of this interpretation and the need for an alternative explanation.

The radiative rate in $MAPbI_3$ is the inverse process of absorption and is strongly temperature dependent, as recently shown by Davies et al.[33] (see also Section 2.5.1), and has the approximate form $k_2^r \sim \exp(C/kT)$. The non-radiative recombination mechanisms discussed in Section 2.5.3 can also be temperature dependent. I therefore believe that the temperature dependence observed in the radiative efficiency of metal halide perovskites is likely to be due to the interplay of these two rates.

3 EXPERIMENTAL METHODS

3.1 Photoluminescence spectra

Charge-carrier recombination mechanisms are vital to the understanding of solar cell operation, as discussed in Section 2.5. Studying the photoluminescence emitted when a material is excited by a light source is therefore a useful way to achieve insights into the optoelectronic properties. Measuring the intensity of the PL emitted as a function of wavelength (PL spectrum) gives three main parameters – the wavelength (or energy) of maximum emission intensity, the linewidth of the emission, and the intensity. The peak photon energy gives an approximate indication of the band gap or the energy of a defect level if this is the main source of emission. The linewidth indicates the disorder in the material. The intensity can determine what proportion of charge-carrier recombination is radiative.

3.1.1 Photoluminescence spectroscopy

The experimental set-up used for photoluminescence spectroscopy is shown in Figure 3.1. Samples are excited using a Ti:Sapphire pulsed (80 fs) laser with a tunable infrared wavelength and an 80 MHz repetition rate (Mai Tai, Spectra-Physics). A BBO crystal is used to double the excitation frequency to give a wavelength in the visible spectrum. The infrared fundamental wavelength is filtered out using a polarizer and a band-pass

colour filter. The excitation intensity is attenuated to an appropriate value for each experiment, using an OD1 filter and a variable attenuator consisting of a waveplate and a vertical polarizer. A horizontal polarizer and a 550-nm long-pass colour filter are placed after the sample to remove any laser scatter from the spectrum. Photoluminescence from the sample is collected by a pair of off-axis parabolic mirrors and focused onto the entry slit of a grating monochromator (Triax, Horiba). The spectrally resolved PL is detected by a nitrogen-cooled Si-CCD detector (Symphony, Horiba) and the spectral response of all components is corrected for using a tungsten filament lamp with known spectrum. This is particularly important for tin perovskites since the sensitivity of the CCD drops off in the near infrared (NIR) where these materials emit. The specific experimental conditions used in each chapter are shown in Table 3.1, unless stated otherwise.

	Wavelength / nm	**Power / mW**	**Beam Size / mm^2**	**Fluence / $nJcm^{-2}$**
Chapter 4	400	0.5	0.2	3
Chapter 5	400	1 100	0.09	14 1400
Chapter 6	500	0.1	0.2	0.6

Table 3.1. Laser wavelength and excitation power used to excite samples for photoluminescence measurements.

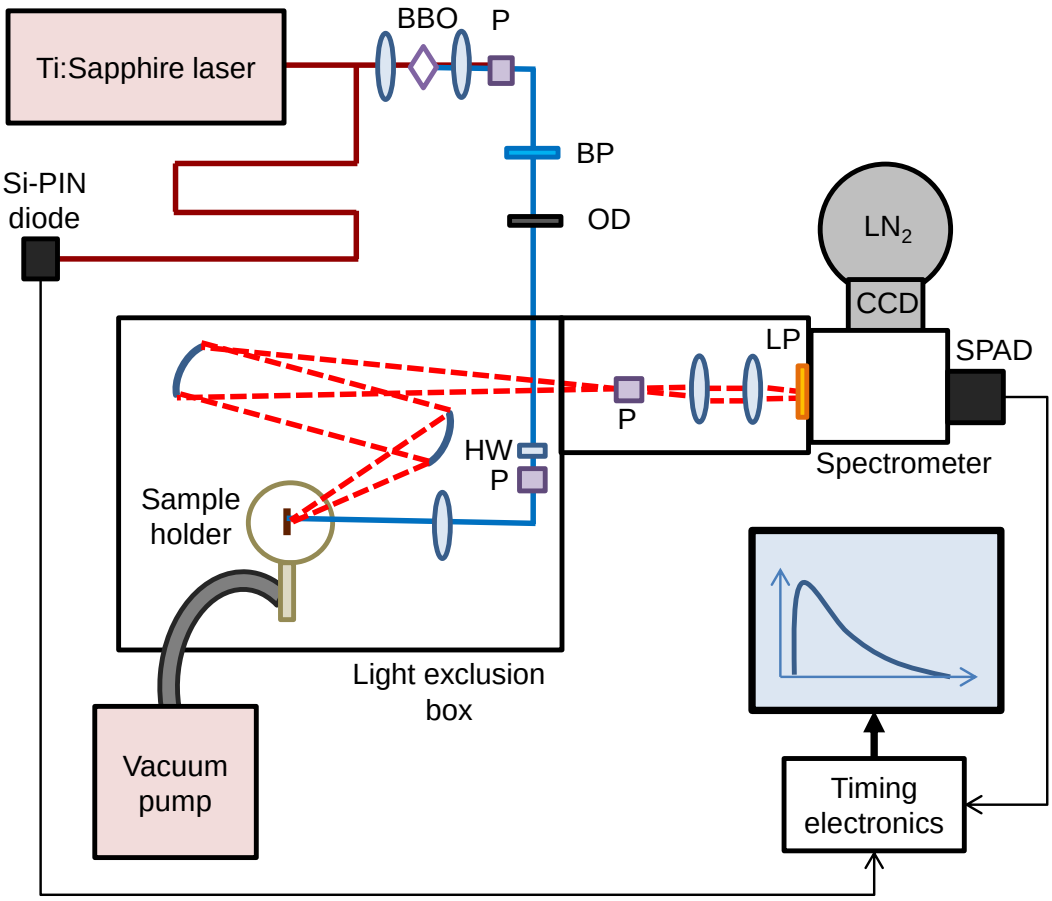

Figure 3.1. Schematic diagram of the experimental set up for measuring PL spectra and time-resolved PL. Polarizers are marked 'P', the half-wave plate is marked 'HW', band-pass filter 'BP', long-pass filter 'LP', and optical density filter 'OD'. The IR beam path is shown in dark red, the frequency doubled excitation beam in blue and the PL with a red dashed line.

3.1.2 Fitting PL spectra

For the purposes of relating the PL spectrum to the band gap energy and amount of disorder, it is more useful to analyse the PL spectrum in terms of photon energy. The PL intensity is recorded experimentally as a function of wavelength. The following equation can be used to convert the spectrum from wavelength to energy:

$$f(E)dE = f(\lambda)d\lambda$$

Equation 3.1

Using the conversion between energy and wavelength $E = hc/\lambda$ gives

$$f(E) = f(\lambda)\frac{\lambda^2}{hc}$$

Equation 3.2

where h is Plank's constant and c is the speed of light.

To find the energy of maximum PL intensity and the linewidth, one could fit the whole peak with a Gaussian, however the spectral shape is rarely a perfect Gaussian as shown in Figure 3.2a. Instead, the maximum intensity is found by fitting a Gaussian function to the very top of the peak, which means the exact shape of the peak does not need to be known, but the value is less affected by noise compared with picking the point of maximum intensity. The full width at half maximum (FWHM) is found from the energy difference of the two points in the spectrum which have half the maximum intensity (one on each side of the peak). These points are located by smoothing the spectrum and, (taking each half of the spectrum separately) using a linear interpolation between the points closest to having half the maximum intensity to find the correct photon energy. The FWHM is the difference between the photon energy values found. This method is show in Figure 3.2b.

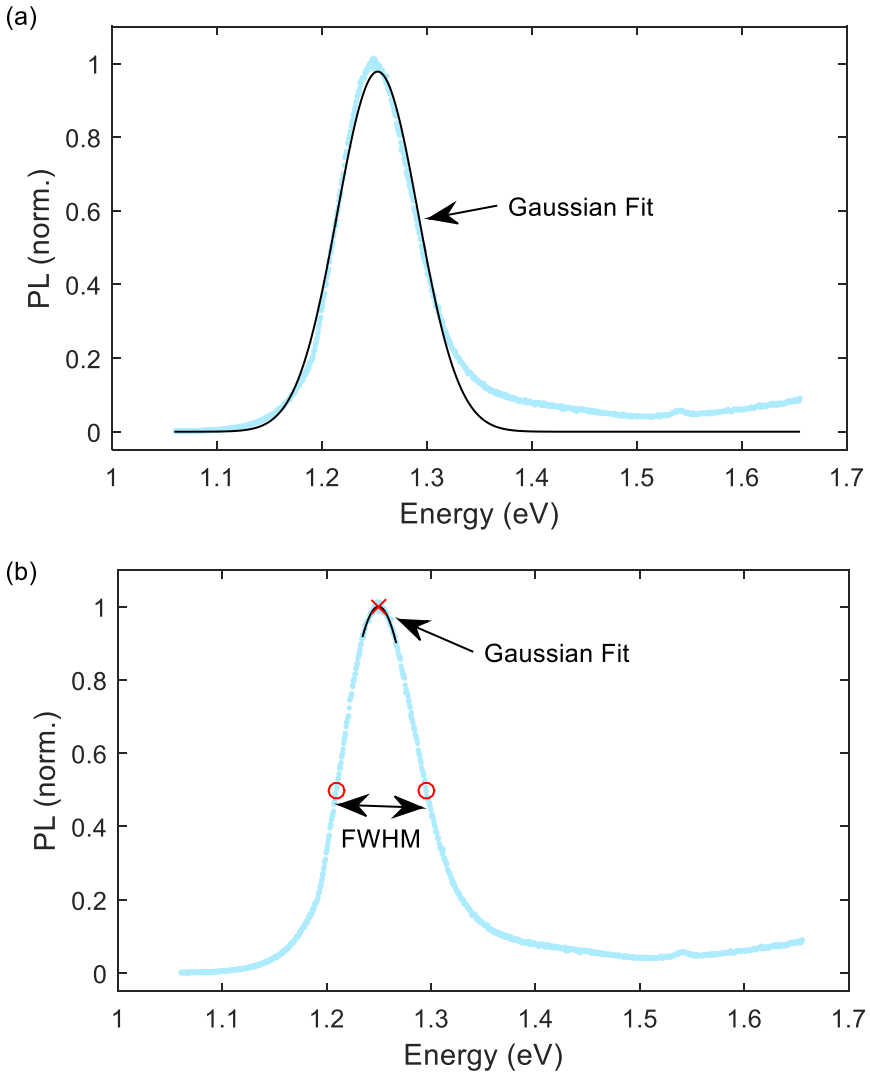

Figure 3.2. Examples of (a) a Gaussian fit to the whole peak and (b) the method described in Section 3.1.2, used to determine peak PL and FWHM

3.1.3 Correction of PL spectra for self-absorption

If the PL spectrum and absorption spectrum of a material overlap, some of the emitted PL will be reabsorbed by the material before escaping, a phenomenon known as self-absorption. This is applicable to lead halide perovskites since their Stokes shift is small. According to Steiner et al.[152], the escape probability from the front side of a film for a photon emitted at an angle θ_i and a depth z in the direction of travel is given by[§]

$$P(z,\lambda) = \frac{1}{2}(1 - R_f)\,\frac{e^{-\alpha z} + R_b e^{-\alpha(2L-z)}}{1 - R_f R_b e^{-2\alpha L}}$$

Equation 3.3

where R_b is the probability of reflection from the back interface, R_f is the probability of reflection from the front interface, α is the absorption coefficient, $L = D/\cos\theta_i$, D is the film thickness and θ_i is the angle of incidence of the emitted photon at the interface. This equation is derived by summing the intensity over multiple reflections, thereby assuming that there is no interference between reflections, which is reasonable since light is being emitted at all points in the film and therefore coherence is lost.

The angle θ is determined via Snell's law by the collection angle given by the optics in our experiment. The reflection probabilities are determined by using the Fresnel equations, assuming no favoured polarization. The refractive indices are taken to be 2.5 for perovskite,[153] 1.0 for vacuum (front interface) and 1.5 for quartz.[153]

The Fresnel equation giving the probability of reflection R for a mixture of parallel and plane polarized light is:

$$R = \frac{1}{2}\left(\frac{n_1\cos(\theta_i) - n_2\cos(\theta_t)}{n_1\cos(\theta_i) + n_2\cos(\theta_t)}\right)^2 + \frac{1}{2}\left(\frac{n_1\cos(\theta_t) - n_2\cos(\theta_i)}{n_1\cos(\theta_t) + n_2\cos(\theta_i)}\right)^2$$

Equation 3.4

[§] Steiner's equation does not contain the factor ½, but I believe this to be in error. However this does not make a difference to the shape of the spectrum, which is what we are interested in.

where n_1 and n_2 are the refractive indices of the first and second materials and θ_i and θ_t are the angles of incidence and transmission at the boundary. For the front surface, the first medium is perovskite and the second medium is air with a transmission angle of 5° determined by the collection optics. The incident angle can be calculated from Snell's law:

$$\theta_i = sin^{-1}\left(\frac{n_2}{n_1} sin(\theta_t)\right)$$

Equation 3.5

Thus for the front surface, n_1 = 2.5, n_2 = 1.0, θ_t = 5°, θ_i = 2°; giving a reflection probability of R_f = 18%.

For the back surface, the first medium is perovskite and the second medium is quartz with an incident angle equal to that calculated above. The transmission angle can be calculated from Snell's law. Thus n_1 = 2.5, n_2 = 1.5, θ_t = 3°, θ_i = 2°; giving a reflection probability R_b = 6%. These angles are illustrated in Figure 3.3.

Emitted photons can be assumed to originate equally from all depths of the film, since the initial charge-carrier distribution becomes homogeneous by diffusion of carriers and by self-absorption on a short time scale compared with the PL lifetime of the sample.[153] To find the external intensity, the internal quantum efficiency and number of reabsorption events must be taken into account. For the purposes of this thesis it is necessary only to know the shape of the spectrum, therefore the escape probability P given in Equation 3.3 can be integrated over all depths z to find the shape of the PL spectrum emitted from the film, $M(\lambda)$, from a true PL spectrum $I(\lambda)$:

$$M(\lambda) \propto I(\lambda)\ \frac{1}{L}\int_0^L P(z,\lambda)\ dz$$

Equation 3.6

The real spectrum can then be calculated from the measured spectrum, M, by performing the integration in Equation 3.6 and rearranging to give

$$I(\lambda) \propto M(\lambda)\, \alpha_\lambda L \left(1 - R_f R_b e^{-2\alpha_\lambda L}\right)\left(1 - R_f\right)^{-1}(1 - e^{-\alpha_\lambda L})^{-1}(1 + R_b e^{-\alpha_\lambda L})^{-1}$$

Equation 3.7

where α_λ is the absorption coefficient as a function of wavelength. By substituting $\alpha_\lambda L = a_\lambda/\cos\theta_i$, Equation 3.7 can be calculated using the measured optical depth a, and incident angle θ_i, without needing to know the thickness or absorption coefficient (see Section 3.3.2).

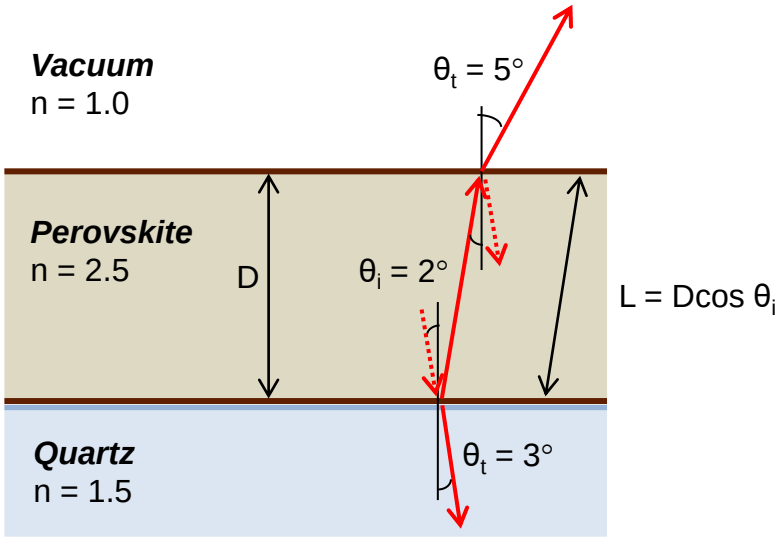

Figure 3.3. Reflection from interfaces of a perovskite film on quartz, used to calculate self-absorption.

3.2 Time-resolved photoluminescence

In addition to the PL spectroscopy measurements already discussed, it is also possible to measure the PL over time after excitation with a laser. The average time taken for the PL signal to decay to 1/e of its initial value reflects the lifetime of the charges before recombination. The functional form of the decay curve can also provide insight into the type of recombination mechanisms which are dominating.

3.2.1 Time-correlated single photon counting

Time-correlated single photon counting (TCSPC) is a method of recording the time dependence of the PL of a material. The method uses a pulsed laser to excite the material, then electronically records the arrival time of a single photon that is subsequently emitted. This is repeated each time the laser pulses, over many periods, to generate a histogram showing the PL over time.

Single photon detection relies on the expected number of detected photons in a pulse period being much less than 1, such that either 0 or 1 photons will be detected between laser pulses. If 2 or more photons arrive in a period the detector registers the first photon only, introducing a bias towards early photons, which leads to the PL lifetime appearing artificially shorter. To prevent this, the average count rate of the detector is kept at around 1% of the laser excitation rate, so that only 1 in 100 pulses generate a count at the detector. Assuming a Poisson distribution, the number of photons not registered due to arriving in the same interval as another photon is around 0.5% of the total number of counts, which is low enough to give an accurate histogram.

Standard System

When a measurement window of less than 12.5 ns is required, the set up for time-resolved photoluminescence is the same as in Section 3.1.1, except for two differences.

Firstly, the fundamental infrared beam is detected by a silicon PIN diode, acting as a trigger to mark out the time between laser pulses used as the measurement window for time correlated single photon counting (TCSPC). The second difference is that light emitted at the peak PL wavelength is not directed onto the CCD but selected by a second slit at the exit of the spectrometer and detected by a silicon single photon avalanche diode (SPAD). These two detectors allow the time between the sample being excited and emitting a particular PL photon to be measured. The instrument response function (IRF) is measured by recording the time-resolved signal of laser light scattered from a roughened quartz disk placed in the sample holder. For this set-up, the IRF is limited by the detector response (~35 ps), not the laser pulse duration (~80 fs). The detector response is slightly dependent on detection wavelength, so when measuring the IRF it is necessary to set the wavelength of the laser as close as possible to the PL measured for each experiment. The excitation conditions for each experiment were the same as listed in Table 3.1.

Diode Laser System

For samples with longer PL lifetimes, the PL does not decay sufficiently within the 12.5 ns measurement window to accurately record the decay curve. Instead an electronically pulsed diode laser with a wavelength of 400 nm and a variable pulse frequency (PicoHarp LDH-D-C-405M) is used for excitation. The PL wavelength was selected using Princeton Instruments SP-2558 grating spectrometer before detection by a silicon single photon avalanche diode. This laser has a much longer pulse duration (a few hundred picoseconds) than the Ti:Sapphire laser, and it is this that limits the IRF. The pulse duration is dependent on the settings used to control the diode laser, particularly the power, so when measuring the IRF it is necessary to keep the laser settings the same as when exciting the sample.

This set up is only necessary for the experiments in Chapter 5 for $FAPb_{1-x}Sn_xI_3$ with more than 50% tin content (x > 0.5). The beam size of this laser at the sample position is 0.018 mm^2 and the pulse frequency is chosen between 0.5 and 20 MHz depending on the lifetime of the sample. The power is chosen to match the fluences used for measurements on the standard system (14 and 1400 $nJcm^{-2}$).

3.2.2 Fitting time-resolved PL

It may initially seem sensible to fit Equation 2.5 from Section 2.5 to the time-resolved PL data. However, the PL intensity is proportional not to the photoexcited charge-carrier density Δn, but to the radiative recombination rate. For band-to-band recombination of free charge-carriers, it is assumed that the PL intensity is proportional to Δn^2, as discussed in Section 2.5.1. However this does not hold in a doped semiconductor, where the presence of doped electrons or holes results in a contribution to radiative recombination that is proportional to Δn, such that the PL dynamics will be determined by the ratio of k_1^r to k_2^r. I have already discussed that doping is relevant for tin halide perovskites (Section 2.5.1), and I have also shown that Equation 2.5 does not hold in some trap-assisted recombination scenarios, which may be applicable to lead halide perovskites (Section 2.5.2). It would be possible to develop a model involving all of these factors, however in practice, this would result in an equation with too many fitting parameters to determine physically meaningful values from the data in the experiments. Instead it is common to parameterize the decay curves with a stretched exponential

$$I = I_0 \exp(-[t/\tau]^{\beta})$$

Equation 3.8

and extract τ_{eff}, the effective lifetime and β, the stretch parameter. The effective lifetime is defined as $\tau_{eff} = \tau/\beta\ \Gamma(1/\beta)$ where Γ is the Gamma Function.

Figure 3.4 shows the stretched exponential function (Equation 3.8) fitted to data simulated using Equation 2.5 with $k_2 >> k_1$, such that the charge-carrier density $\Delta n \sim t^{-2}$. Whilst the fit will never be perfect, it does provide a useful way to parametrize the decay, where mono-exponential decay for $k_1 >> k_2$ gives $\beta = 1$, and here the fit for $k_2 >> k_1$ gives $\beta = 0.4$.

The curves are fitted by determining the time taken for the PL to drop from the maximum (initial) intensity I_0 to either I_0/e or $I_0/10$, yielding values for τ_e and τ_{10}, respectively. These values are used to pick initial parameter values for a stretched exponential fit (Equation 3.8), which gives the effective lifetime τ_{eff} and the stretch parameter β. The initial value for β is calculated by rearranging Equation 3.8 with $t = \tau_{10}$ to give

$$\beta = \frac{ln(ln\,10)}{ln\left(\frac{\tau_{10}}{\tau_e}\right)}$$

Equation 3.9

This approach is illustrated in Figure 3.5.

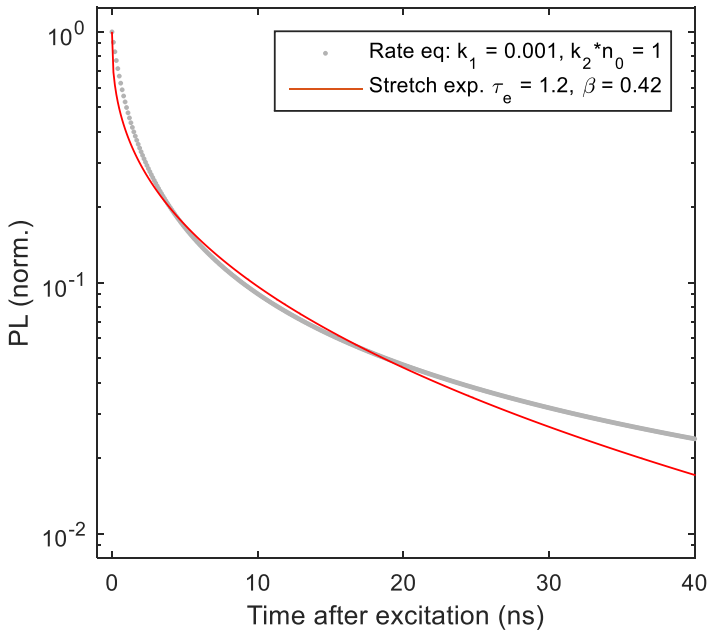

Figure 3.4. The grey line shows a simulated PL decay with the time-dependent carrier density determined by Equation 2.5, with K<<1 (i.e. the bimolecular term in Equation 2.4 dominates). The red line is a stretched exponential fit to the simulated data.

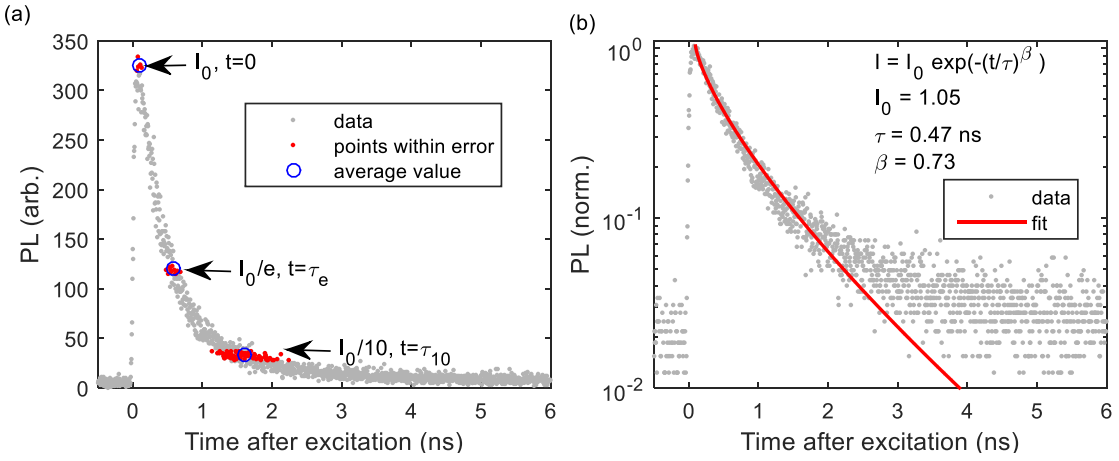

Figure 3.5. Example of (a) determination of parameters τ_e and τ_{10} and (b) stretched exponential fit for $FASn_xPb_{1-x}I_3$ with x = 0.875, excited at 14 nJ/cm^2 power, 400 nm wavelength at a temperature of 60 K.

3.2.3 Instrument response function

When the charge-carrier lifetime is very short, the time response of the system must be taken into account, known as the instrument response function (IRF). For the standard system this is limited by the response of the photodiode, whereas for the diode laser it is limited by the length of the laser pulse.

The measured decay curve (MD) is a convolution of the real decay curve (RD) and the IRF, which can be calculated using Fourier transforms:

$$F(MD) = F(IRF)F(RD)$$

Equation 3.10

where F and F^{-1} are the Fourier transform and inverse Fourier transform respectively.

If the data are being fitted with a curve, the IRF can be accounted for by convoluting the fitting function with the measured IRF according to the Equation 3.10, prior to performing a fit to the data. Alternatively, the measured decay curve and IRF can be smoothed and then deconvoluted to produce the real decay curve according to the formula

$$RD = F^{-1}\left[\frac{F(MD)}{F(IRF)}\right]$$

Equation 3.11

Both these methods are used in this thesis. In Chapter 4, the real decay curve is obtained by deconvolution, and the 1/e lifetime is found without fitting, since the functional form of the decay curve changes with temperature and a good fit could not be found across the entire temperature range. Examples of the deconvoluted curves are shown in Figure 3.6. In Chapter 5, the PL lifetimes measured were much longer, so the IRF is not accounted for in the lifetimes measured. However, this gives a slight overestimate of the lifetime for a few of the measurements - the samples with high tin content at room temperature where the lifetime is below 1 ns. The true lifetimes of these

samples are calculated by fitting an exponential decay function convoluted with the measured IRF, as shown in Figure 3.7.

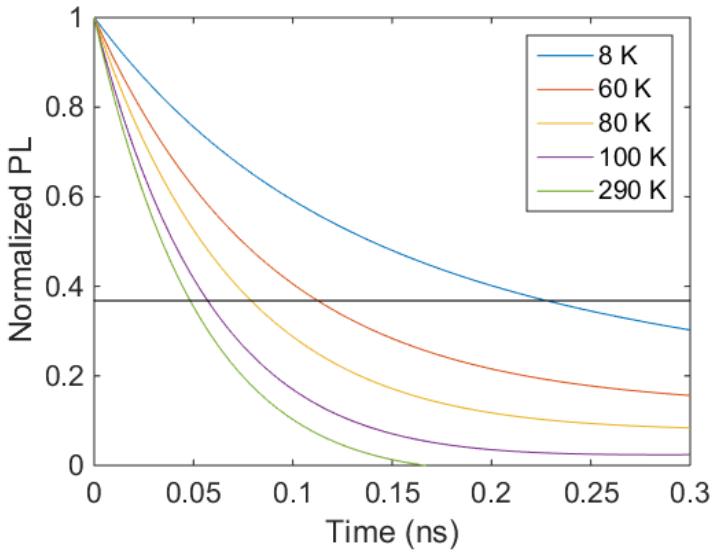

Figure 3.6. Real decay curves determined by smoothing the measured decay curves and deconvolving with the instrument response function. The horizontal line marks 1/e.

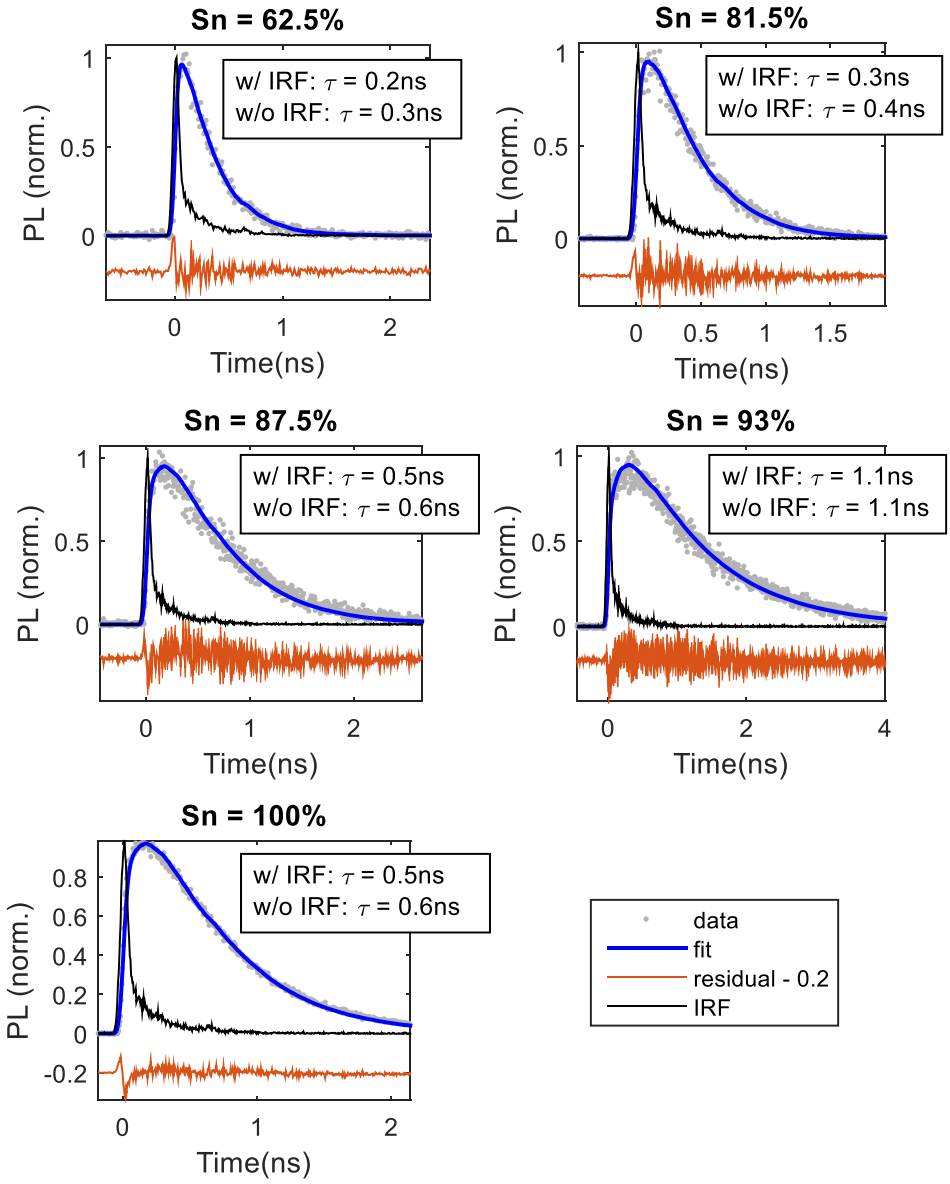

Figure 3.7. PL decay curves for two $FASn_xPb_{1-x}I_3$ compositions, excited at 400 nm, 14 nJ/cm^2. Mono-exponential curves convolved with the instrument response function (IRF) are shown in blue. The residual of the fit is shown underneath in orange, offset by -0.2.

3.3 Absorption spectra

The absorption coefficient of a semiconductor is clearly recognisable by its absorption edge, which is determined by the band gap of the material. At photon energies lower than the band gap, the absorbance will be zero, and above the band gap the absorbance will be strong and increase with photon energy.

3.3.1 Fourier transform infrared spectroscopy

In this thesis, I measure transmission and reflection of materials in the visible and near infrared using a Fourier Transform Infrared (FTIR) Spectrometer (Vertex 80v, Bruker). A tungsten halogen lamp is used as a light source, and the light passing through the sample (or reflected from the sample) is detected by a silicon diode detector (visible wavelengths) or liquid nitrogen cooled InSb detector (NIR wavelengths). A blank substrate and a silver mirror are used as references for 100% transmission and reflection respectively. Background measurements are also used to correct for any scatter from the sample holder and other optical components. The data is recorded against wavenumber (cm^{-1}), so the transformation to photon energy is straightforward and does not require the conversion in Equation 3.2.

3.3.2 Absorption and optical depth

After measuring the reflection and transmission, the proportion of incident light absorbed as a function of photon energy (A) can be calculated using

$$A = 1 - T - R$$

Equation 3.12

Alternatively, the optical depth (a), which is equal to the absorption coefficient (α) times the sample thickness (D), can be calculated from measurements of the transmission and reflection of the sample using Beer's law, rearranged to give:

$$a = \alpha D = -ln\left(\frac{T}{1-R}\right)$$

Equation 3.13

For the temperature dependent absorption spectra in Chapter 4 I was not able to measure the reflection due to the limitations of the set-up (remedied by the purchase of a gas exchange cryostat used for the measurements in Chapter 5). Assuming the reflection is zero does not change the results a great deal, but it is noticeable at photon energies lower than the band gap where non-zero absorption is calculated, which is in fact a result of the loss in measured transmission due to reflection.

3.3.3 Thickness determination

If the absorption coefficient is known, the thickness of a film can be calculated from its optical depth. When there is a small amount of scatter unaccounted for in the measurement, the measured optical depth is given by

$$a = \alpha D + b$$

Equation 3.14

where b is the measurement background, D is the film thickness, which I will call the 'optical film thickness', and α is the absorption coefficient.

To improve the accuracy, the calculated absorbance can be matched to the absorption coefficient across a range of wavelengths, instead of matching at only a single wavelength point. The measured optical depth, a, can be plotted against the known absorption coefficient α for the same values of wavelength, and fitted with a linear equation, such that the gradient of the fit gives D. The value of b can be constrained to keep the below-band gap absorption close to zero.

Figure 3.8 shows an example of this thickness determination method using measured optical depth data from Chapter 6 and absorption coefficient data calculated by Timothy Crothers, a colleague at the University of Oxford, and published in ref. 153.

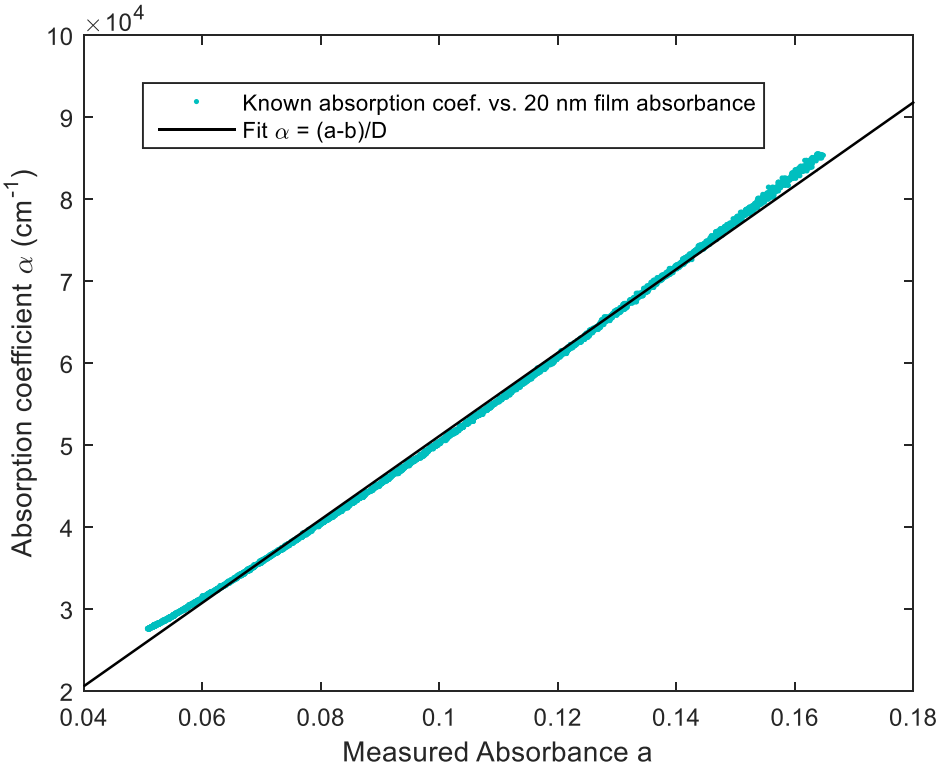

Figure 3.8. Example of fit to determine optical thickness *D* by plotting a known absorption coefficient (taken from ref. 153) against the absorption (from 550-700 nm) of a $MAPbI_3$ thin film sample from the batch with 240 s deposition time, giving $D = 20$ nm.

3.3.4 Determining absorption edge

The absorption edge is defined here as the point on the absorption curve with the steepest gradient, and is found by differentiation of the curve in the region of the absorption onset. This definition will give a slightly larger energy than that determined by a Tauc Plot, but this method is preferred since the exciton enhancement of the band edge[154] makes the Tauc Plot reading unphysical, and may be part of the reason for the wide range of band gap energies reported in some perovskite materials (see Section 2.3.1)

Here I compare the band gaps obtained by the steepest gradient method with those obtained from a Tauc plot, which is more widely used in the literature,[88,121] using absorption data for $FAPb_{1-x}Sn_xI_3$ from Chapter 5. For direct band gaps, the band gap (E_g) is determined by plotting $(\alpha E)^2$ against E and finding the intercept with the x-axis (where α is the absorption coefficient and E is the photon energy). However, this method does not take into account the influence of excitons on the shape of the absorption onset. Not only do excitons introduce discrete energy levels, they also enhance the absorption of the continuum states, such that attempting to find E_g from a Tauc plot, which assumes α to be proportional to $\sqrt{E - E_g}$ (where E is the photon energy), will give misleading results. The correct way to determine the band gap is to fit the full Elliot theory formula which includes the enhancement from excitons.[31,33] However, to apply this method correctly requires very 'clean' absorption data which have been corrected for reflection and scatter, which is often not practical experimentally, particularly when only an approximate determination of the band gap is required. The 'steepest gradient' method is therefore recommended as a more practicable alternative.

Although the steepest gradient method does not accurately determine the true band gap, it gives a more meaningful quantitative result allowing comparison of absorption onsets and is less sensitive to a number of problems encountered with Tauc plots which are illustrated in Figure 3.9. Firstly, a change in the strength of the exciton absorption will change the gradient of the 'straight line section' which influences the intercept, as shown for the $FAPb_{1-x}Sn_xI_3$ sample with Sn = 0%. Secondly, reflection or diffuse scatter from the sample which has not been accounted for will result in non-zero absorption below the band gap which can give an offset and will influence the intercept, as shown for the Sn = 87.5% sample. Finally, since the expectation of a straight line is not physically grounded, there is not always an unambiguous straight line section to fit to, with either no straight line at all or several straight sections, as shown for the Sn = 25% sample where two portions are fitted, one in black and one in grey.

To illustrate the difference in the measured band gap between the Tauc plot and this gradient method of determining the absorption onset, Figure 3.10 shows both methods applied to data from Chapter 5. For the steepest gradient method, the data fits to a single bowing parameter, whereas the Tauc plot method gives the impression of a composition dependent bowing parameter. Some of the discrepancy in the degree of bowing found in the literature may be as a result of different methods for determining band gap from absorption data, rather than being caused by differences in the material itself. As a result of this analysis, I use the steepest gradient method throughout this thesis.

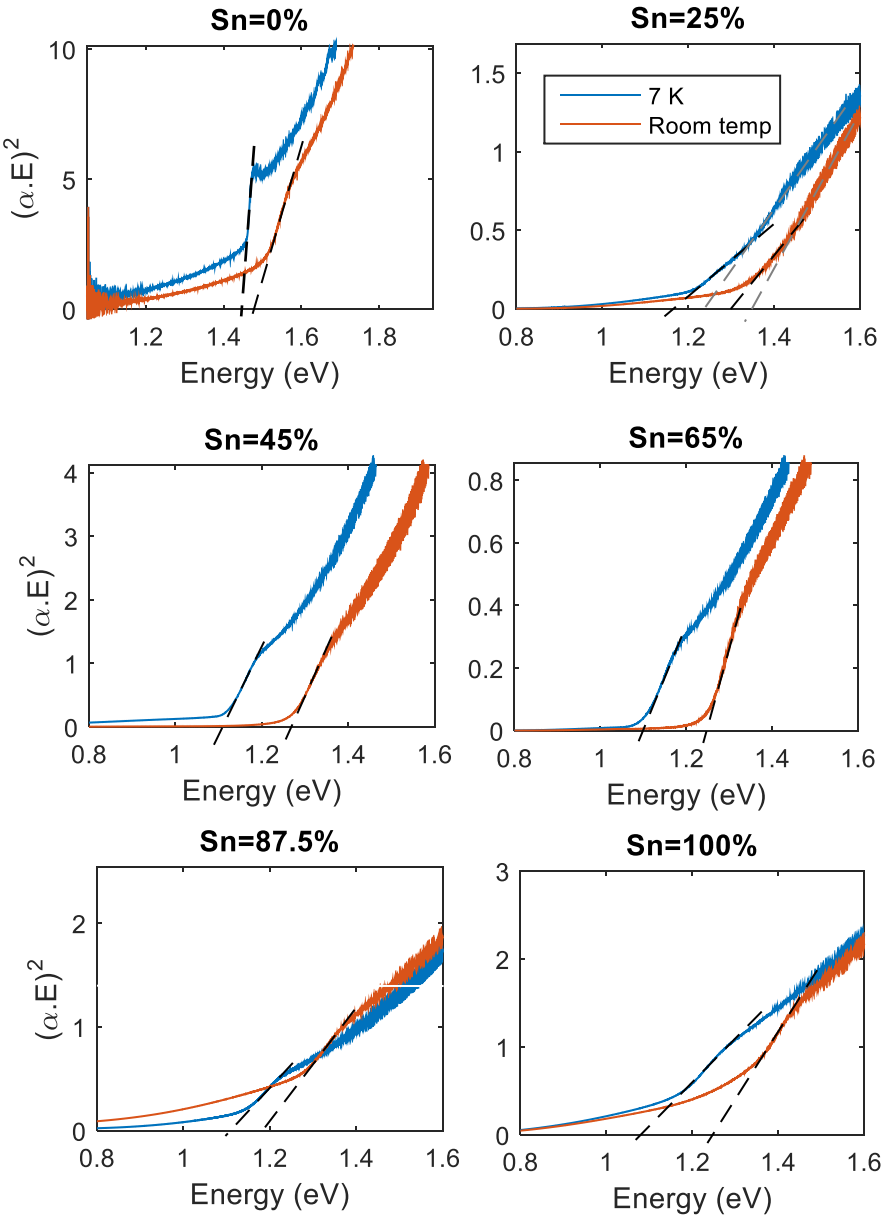

Figure 3.9. Tauc plot from absorbance of each composition of $FASn_xPb_{1-x}I_3$ at a room temperature of 295 = K (orange) and low temperature of 5-10 = K (blue). The dashed lines show fits to the straight-line portions of the curves, giving the optical band gap at the intercept.

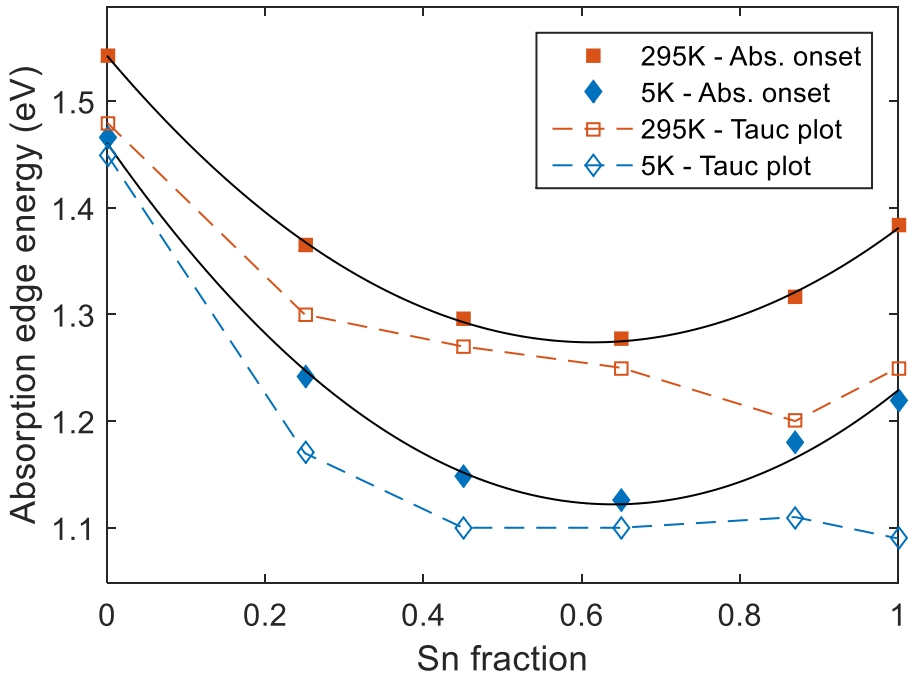

Figure 3.10. Optical band gap of $FASn_xPb_{1-x}I_3$ determined by the absorption onset (filled points) and by a Tauc plot (empty points) at 295 K (orange) and 5 K (blue) temperature. Black lines show parabolic fits to the absorption onset data, and dashed lines are guides to the eye for the Tauc plot data.

3.4 Temperature dependent measurements

Many properties of a semiconductor are temperature dependent, and therefore more insight can be gained by studying these properties at low temperature where phonons and dopants can be 'frozen out'. In addition it is interesting to study how the structural phase changes affect the optoelectronic properties. This is achieved by using liquid helium to cool the materials studied to temperatures as low as 4 K.

3.4.1 Cold finger cryostat

Samples are fabricated inside a nitrogen filled glovebox and sealed inside a cold-finger cryostat (MicrostatHe, Oxford Instruments) whilst still inside the glovebox to eliminate exposure to air. The cryostat is then transferred to the laser laboratory and evacuated, maintaining a pressure below 10^{-5} mbar, with no degradation in PL observed for the duration of the measurements. The temperature is controlled by a flow of liquid helium and an electronic temperature controller (ITC503, Oxford Instruments). The temperature is monitored with sensors both on the cryostat heat exchanger and the end of the sample holder.

3.4.2 Gas exchange cryostat

The purchase of a gas exchange cryostat enabled temperature dependent reflection measurements to be carried out in the FTIR setup. The sample is briefly exposed to air whilst it is being mounted into the chamber. The chamber is then evacuated and purged with helium gas at least three times to ensure no air remains. The temperature is controlled as above.

3.5 X-ray diffraction spectra

X-ray diffraction (XRD) measurements are performed by Jay Patel at the University of Oxford. The samples are mounted on a rotating sample holder in ambient conditions. 2θ measurements are performed using an X-ray diffractometer (Panalytical X'Pert Pro). The scan speed is 0.4 °/s for 30 minutes (Cu-Kα radiation at λ=1.54Å) operating at 40 kV and 40 mA.

3.5.1 Fitting XRD spectra

The XRD spectra are fitted by Amir-Abbas Haghighirad and Jay Patel, both at the University of Oxford. The spectra are fitted with a Pseudo-Voigt function using the general structural analysis software (GSAS) to extract the peak position and the full width at half maximum (FWHM). The angles of the peaks are corrected for sample tilt by using the quartz peak at 16.433° as a reference. The d-spacing for each thickness is found from the angle of the perovskite (100) and (200) peaks using Bragg's law:

$$2d\ sin\,\theta = n\lambda$$

Equation 3.15

where $n = \sqrt{h^2 + k^2 + l^2}$ for (hkl) is equal to 1 for (100) and 2 for (200).

The resolution of the XRD spectrometer leads to angle-dependent instrument broadening, which must be corrected for. The XRD spectrum of a silicon reference sample is measured and fitted to determine the FWHM of each of the peaks. The FWHM is plotted against angle in Figure 3.11 with a polynomial fit. From this fit, the instrument broadening at the relevant angle is found, which for the (100) peak of $MAPbI_3$ is: $\beta_{inst} = 0.062°$ at $2\theta = 14°$. The corrected FWHM is found using the equation

$$\beta^2 = \beta_{sample}{}^2 - \beta_{inst}{}^2$$

Equation 3.16

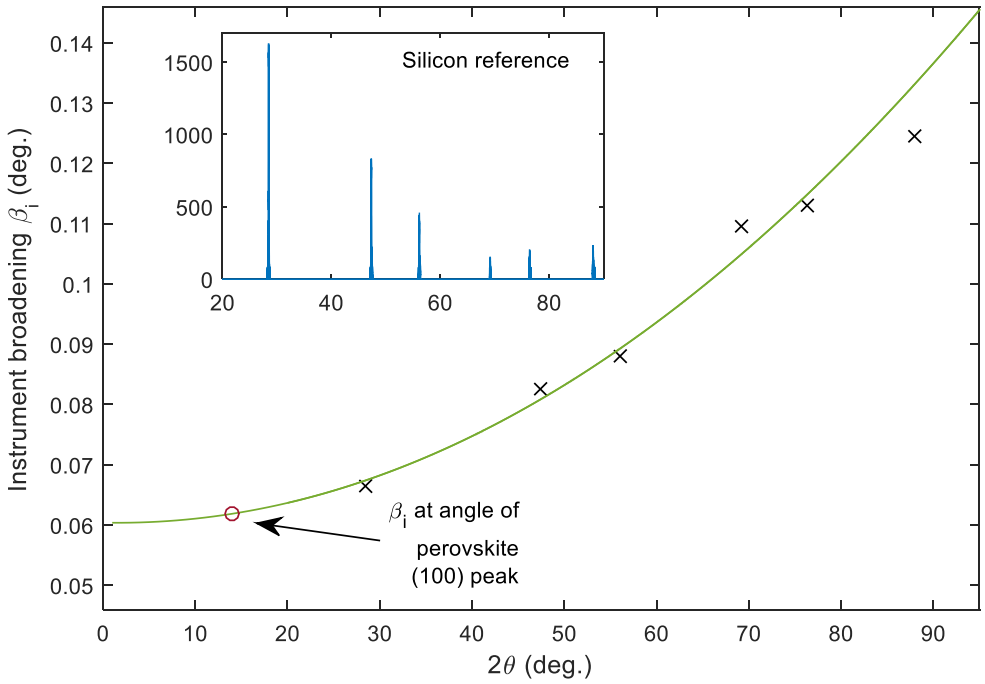

Figure 3.11. Width of the XRD diffraction peak at half maximum for each reflection from the silicon reference as a function of angle (crosses), fitted with a quadratic (green line) which gives instrument broadening as a function of angle. The instrument broadening at 14°, which is used to correct the FWHM of the perovskite (100) peak, is marked with a red circle. Inset: XRD spectrum of the silicon reference sample used to calculate instrument broadening.

3.5.2 Grain size analysis

Smaller grains lead to larger FWHM since there are fewer aligned crystal planes to contribute to diffraction. The grain size can therefore be found from the full width at half maximum (FWHM) of the perovskite peaks, using the Scherrer equation,[155]

$$H = \frac{\kappa \lambda}{\beta \cos\theta}$$

Equation 3.17

where H is the crystallite size, β is the FWHM in radians, λ = 0.15406 nm is the wavelength of the X-rays, θ is the Bragg angle, and κ is known as the shape factor which is determined by the definition of the peak breadth and the shape of the crystallite. Using the FWHM as the measure of peak breadth, κ = 0.8859 gives the height of the crystallite perpendicular to the substrate.[156]

The Scherrer formula is only valid when the crystallite size is the main contribution and broadening due to micro-strain (i.e. the distribution of lattice plane spacing in the sample) can be neglected. When microstrain is included, the formula is given by[157]

$$\beta = \frac{\kappa \lambda}{H \cos\theta} + 4\epsilon \tan\theta$$

Equation 3.18

Following the method of Williamson, the broadening terms are added linearly, since XRD peaks typically have a Lorentzian shape (for which breadth should be added linearly) as opposed to a Gaussian shape (where breadth is added in quadrature). The above expression can be rearranged to give

$$\beta \cos\theta = \frac{\kappa \lambda}{H} + 4\epsilon \sin\theta$$

Equation 3.19

By plotting a graph with y = βcosθ and x = 4sinθ, known as a Williamson-Hall Plot,[157] the strain can be determined from the gradient and the crystallite size from the intercept.

3.6 Sample fabrication

All samples are made in a nitrogen-filled glove box in the on-site clean room by colleagues at the University of Oxford. The tin containing samples are then mounted in a vacuum chamber or sealed cryostat whilst still inside the glovebox to eliminate exposure to air before transfer to the laser laboratory. This ensures the results are repeatable, since tin halide perovskites are known to easily degrade in air, and can turn visibly transparent within a day (see also previous results for samples fabricated in the same way[44]).

The substrates used for all samples are z-cut quartz disks, washed with Hellmanex®, distilled water, acetone and isopropyl alcohol followed by treatment in an oxygen plasma asher for 10 minutes.

3.6.1 $MASnI_3$

These samples were made by Thomas Stergiopolous at the University of Oxford. $MASnI_3$ perovskite thin films were formed on z-cut quartz disks by spin-coating a precursor solution. To form the precursor solution, tin(II) acetate (Sigma) and methylammonium iodide (Dyesol) were dissolved in anhydrous N,N-Dimethylformamide (DMF) at a 3:1 molar ratio with final perovskite precursor concentration of ~30 wt%. A clear yellow solution was obtained by filtering the turbid precursor solution using a PTFE filter (pore size of 0.45 μm). Following this, the solution was dropped onto a quartz disk and spin-coated at 6000 rpm (for 45 s) with a ramp-up of 6000 rpm s^{-1}. After spin-coating, the dark brown films were left to dry at room temperature for around 5 minutes and then annealed at 130°C for 2 minutes to become black.

3.6.2 $FAPb_{1-x}Sn_xI_3$

These samples were made by Thomas Green at the University of Oxford. $FAPb_{1-x}Sn_xI_3$ perovskite thin films were formed on z-cut quartz disks by spin-coating mixtures of $FASnI_3$ and $FAPbI_3$ precursor solutions in appropriate ratios. The precursor solutions were prepared at a concentration of 1M in a mixed solvent of DMF:DMSO 65:35 by volume. The two precursor solutions were dissolved at a 1:1 molar ratio of formamidinium iodide ($HC(NH_2)_2I$) to tin iodide (SnI_2) or lead iodide (PbI_2). In addition, excess SnF_2 (0.2M) was added into the $FASnI_3$ precursor (i.e. providing a 20% excess of tin). The $FASnI_3$ and $FAPbI_3$ precursors were then mixed in the appropriate ratio before spin-coating at 5000 rpm in a nitrogen-filled glovebox. After dropping the solution onto the spinning substrate the speed was ramped down to zero (~5 seconds). The wet transparent film was then immediately immersed into a small petri dish containing anisole (~5 s) and blow-dried with a nitrogen gun. Anisole was not used for the 45 and 65% Sn samples which were spin-coated for 12s including a ramp up (~6 s), blow-dried with a nitrogen-gun whilst still spinning for 16s, spin-coated for a further 8 s followed by a ramp down (~5s) which obtained more uniform film coverage for these compositions. A comparison of the films made with and without anisole for 87.5% Sn is shown in Figure 3.12. The reddish or transparent precursor films were then annealed at 70°C for 20 minutes. For the 0% and 6.25% Sn films, annealing at 170°C for 10 minutes and 1 minute respectively was necessary to form the black phase perovskite as it formed the yellow phase when heated only at 70°C.

3.6.3 $MAPbI_3$ co-evaporation

These samples were made by Jay Patel at the University of Oxford. The films were fabricated using co-evaporation of PbI_2 and CH_3NH_3I.[158] 500 mg each of CH_3NH_3I (synthesised as described in ref. 30) and PbI_2 (ultra-dry 99.999% (metals basis), Alfa

Aesar) were placed in separate crucibles, and the quartz discs were mounted on a rotating substrate holder to ensure that a uniform film was deposited. The temperature of the substrates was kept at 21 °C throughout the deposition. The chamber was allowed to reach a high vacuum ($4x10^{-6}$ mbar), before the PbI_2 and the CH_3NH_3I crucibles were heated to reach a steady rate, as monitored by the quartz crystal microbalance (QCM). Once the deposition rate had stabilized along with the pressure ($4x10^{-6}$ mbar), the substrates were exposed to the vapour. The rates of both the CH_3NH_3I and PbI_2 were calibrated, by analysis of the X-ray diffraction pattern of the thin film to ensure a 1:1 molar ratio was achieved in the final composition of the film. The deposition time was controlled by the programming of the substrate shutter to open and close after a specific time.

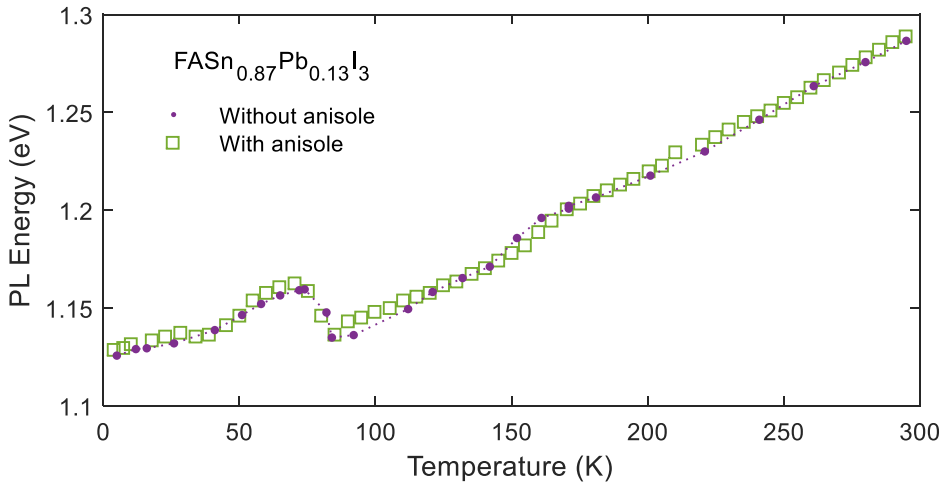

Figure 3.12. Energy at the PL peak for $FAPb_{1-x}Sn_xI_3$ with x = 0.87 made by two methods, one using an anisole dip and one without. The method makes no difference to the optical properties but does improve the surface coverage for the middle compositions.

4 $MASnI_3$: PHASE TRANSITION, CHARGE-CARRIER LIFETIMES AND DEFECTS

The results presented in this chapter have been published in:

Parrott, E. S.; Milot, R. L.; Stergiopoulos, T.; Snaith, H. J.; Johnston, M. B.; Herz, L. M. *The Journal of Physical Chemistry Letters*, 2016**,** 7 (7), pp 1321-1326

4.1 Introduction

Methylammonium tin triiodide ($MASnI_3$) is an attractive alternative to lead-based perovskites due to its lower band gap,[55] with corresponding higher maximum theoretical efficiency (see Section 2.1.2). In addition, environmental concerns have been raised related to the toxicity associated with lead containing materials.[159–162] $MASnI_3$ has been successfully employed in lead-free perovskite solar cells, but overall power-conversion efficiencies are still significantly lower than for lead-based perovskites.[55–57] Despite the importance of defects to the properties of tin-based perovskites, as discussed in Section 2.4.1, experimental studies of their nature and their effect on the optoelectronic properties are relatively scarce. In this chapter I investigate such links by monitoring the photoluminescence (PL) and absorption spectra, and the

PL lifetime of $MASnI_3$ as a function of temperature from 8-295 K. I find that at room temperature, the charge-carrier lifetime is short, and the emission linewidth is severely broadened in accordance with the presence of a sizeable density of defects that act as hole donors. As the temperature is reduced below the phase transition into the orthorhombic phase near 110 K, a significant line narrowing and recovery of charge-carrier lifetimes is observed, and an additional emission peak originating from higher-energy transitions appears. These abrupt changes coincide with a previously reported phase change[115] and a decrease in hole density,[163] which indicates that crystal structure, hole doping, disorder and carrier lifetime are intrinsically linked. Such improved understanding of links between defect chemistry and crystal structure may therefore highlight routes towards further optimization of tin-based perovskites.

4.2 Results and Discussion

First I examine the absorption and emission spectra of $MASnI_3$ thin films as a function of temperature. Figure 4.1a shows a map of the PL intensity as a function of temperature between 8-295 K. The peak emission at room temperature is found to occur at 1.3 eV, near the range of theoretical calculations[77] and previous measurements[55–57,69] of the band gap energy. As the temperature is decreased, the PL peak shifts to lower energy, similar to previously reported band gap trends in $CsSnI_3$[93] and $MAPbI_3$.[71] This gradual redshift is mirrored in the absorption spectrum (Figure 4.1c) obtained from measuring the optical transmission of $MASnI_3$ using Fourier Transform Infrared (FTIR) spectroscopy. I observe a clear absorption onset corresponding to the transition at the band gap (T1) which is centred ~200 meV above the PL peak emission energy, suggesting a sizeable Stokes shift.

$MASnI_3$ is known to exhibit phase transitions at 275 K[122,164] and 108 K[122] when cooled (but 114 K when heated), transitioning from pseudo-cubic (α) at room temperature[69] to tetragonal (β) to orthorhombic (γ) at low temperature. Interestingly, I observe no discontinuity in absorption or PL energy with temperature at the phase transitions, which suggests that the band edge states do not substantially change here. This behaviour vastly differs from that at the β to γ phase transition (160 K) in $MAPbI_3$, which results in a 100 meV shift in bandgap energy.[71,165] It is possible that the effect of the phase transitions on the band gap is masked by the large degree of disorder present, which makes both the PL linewidth and absorption edge very broad, which will be discussed in Section 4.2.2.

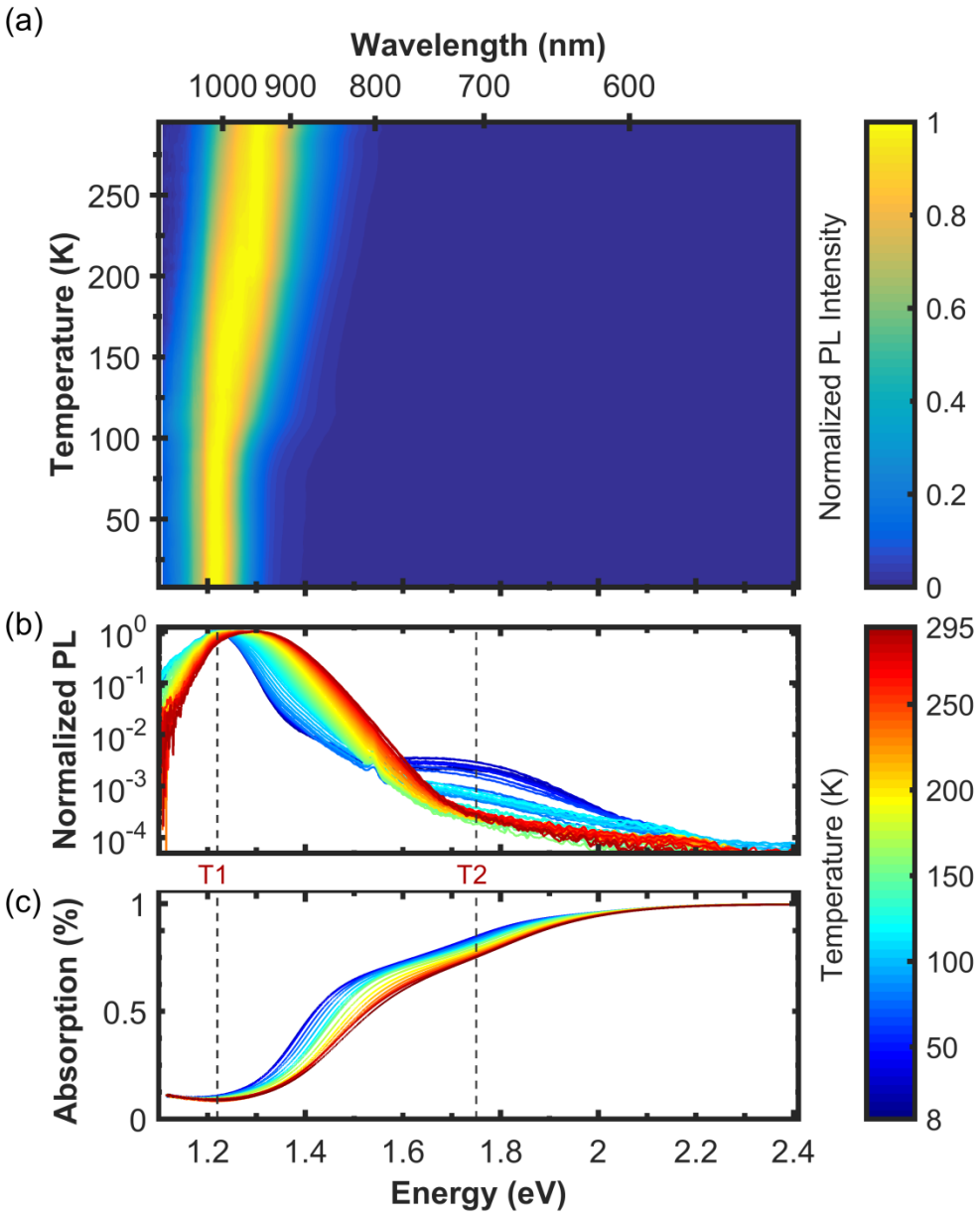

Figure 4.1. (a) Colour map of photoluminescence intensity as a function of temperature, normalized to the peak intensity at each temperature. The sample is excited with a pulsed laser at 400 nm with a fluence of 3 nJcm^{-2} and spectra are collected at intervals of 5 K, cooling the sample from room temperature. (b) Photoluminescence spectra on a semi-log scale and (c) absorption spectra (without reflection correction) from high temperature (red) to low temperature (blue) in the range 8-295 K. Dashed vertical lines mark the two peak PL energies at 8 K.

4.2.1 Secondary emission feature

Before going on to analyse the effect of disorder and impurities on the optoelectronic properties of $MASnbI_3$ it is worth noting a peculiar occurrence, which is the appearance of a secondary, higher-energy absorption and emission feature near 1.75 eV, marked as T2 in Figure 4.1b. This second PL peak is very weak in intensity (note the logarithmic scale); it emerges at 110 K and grows in intensity with respect to the main peak as the temperature is decreased further, almost reaching an intensity of one hundredth of that of the main peak at the lowest temperature. In contrast, a matching absorption feature for T2 is seen over the entire temperature range (Figure 4.1c), which red shifts in the same way as the band edge, as shown in Figure 4.2. Therefore this higher-energy transition T2 appears to be intrinsic to the band structure of $MASnI_3$, persisting over the entire temperature range but only yielding efficient emission in the orthorhombic phase at low temperature.

A similar secondary onset is also seen in the optical absorption spectrum of $MAPbI_3$ (at 2.6 eV or 480 nm) and found to coincide with a photobleach signal in transient absorption spectra,[132,166,167] but luminescence at this wavelength has never been reported. This transition has been variously attributed to an additional valence band,[132] to a different valley in the reciprocal lattice[105] or to a charge-transfer state.[166] A further photobleach signal in $MAPbI_3$ is sometimes seen at around 2.43 eV (510 nm) and attributed to excess PbI_2.[168] However SnI_2 has a band gap of 2.57 eV (at 8 K),[169] far from the peak observed at 1.75 eV, and therefore T2 cannot be caused by excess SnI_2.

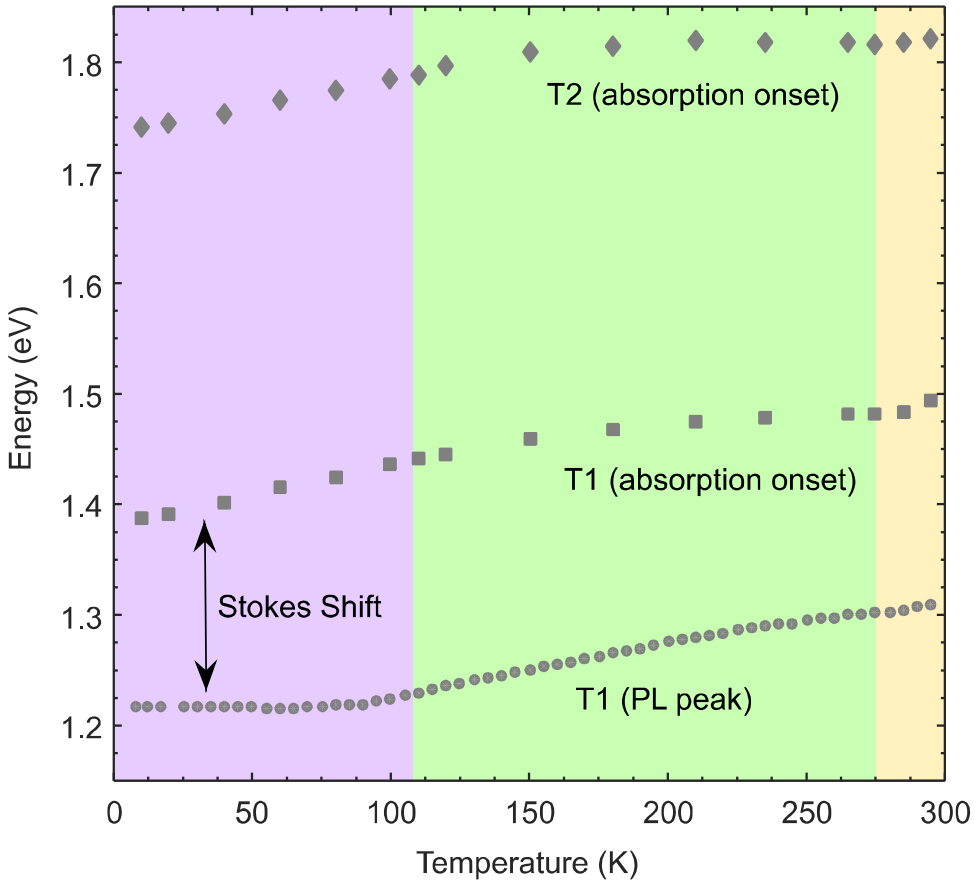

Figure 4.2. Energies of the two transitions apparent in the absorption and emission spectra of $MASnI_3$, T1 (absorption, squares; emission circles) and T2 (absorption, diamonds). Emission energies were taken from PL peaks, and absorption energies from the midpoint of the broadened absorption rise, as determined by finding the maximum gradient. Note that the midpoint is not exactly equal to the band gap but gives a direct indication of how the band gap shifts with temperature.

I therefore attribute the origin of the emission observed at ~1.7-1.8 eV to additional transitions associated with the electronic band structure of $MASnI_3$, as illustrated in Figure 4.3. Theoretical calculations predict that spin orbit coupling is important in the band structure of both lead and tin perovskites, resulting in two conduction bands, CB1 and CB2, split by the energy of the spin orbit interaction E_{SOC}.[74] For $MASnI_3$ $E_{SOC} = 0.4$ eV, compared to 1.5 eV for $MAPbI_3$.[170] Two optically allowed transitions are therefore associated with these bands – a strong transition from VB1 to CB1, associated with band gap energy $E_g = 1.3$ eV, and another weak transition from VB1 to CB2 with energy $E = E_g + E_{SOC} = 1.7$ eV.[74,170] These theoretical predictions correspond to the energies of the transitions observed, making this a likely explanation. Alternatively, these transitions could arise from different electronic bands, or different points in the Brillouin zone, however the latter would require exceptionally slow intraband carrier thermalization, which is unlikely.

Decay curves for the PL at both the main peak (T1) and the secondary peak (T2) at 8 K are shown in Figure 4.4 for two different fluences of 30 and 300 $nJcm^{-2}$ (at the lower fluence of 3 $nJcm^{-2}$ used in the rest of the measurements in this chapter, the signal-to-noise ratio for the secondary peak (T2) is too low to obtain data). At 30 $nJcm^{-2}$, the two peaks have similar decay dynamics. Increasing the fluence to 300 $nJcm^{-2}$ increases the decay rate for both transitions, likely due to an increase in bimolecular recombination as expected from Equation 2.4. T2 is affected much more by the fluence change with the initial decay limited by the IRF, suggesting it may have a larger bimolecular recombination rate constant, or that the higher fluence causes faster interband relaxation. There is also a longer lived component to this decay, which could potentially arise from overlapping PL originating from T1.

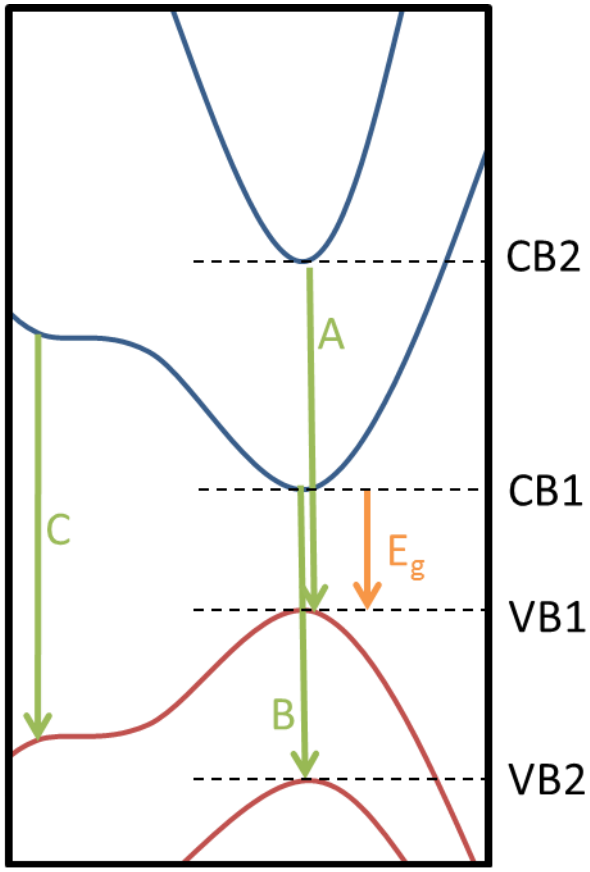

Figure 4.3. A schematic band dispersion diagram showing possible transitions responsible for T2 (illustrative, based on calculations[74,115]). Possibilities include A, a transition to the spin-orbit split conduction band, B, a transition to a second valence band and C, a transition at a different point in k-space.

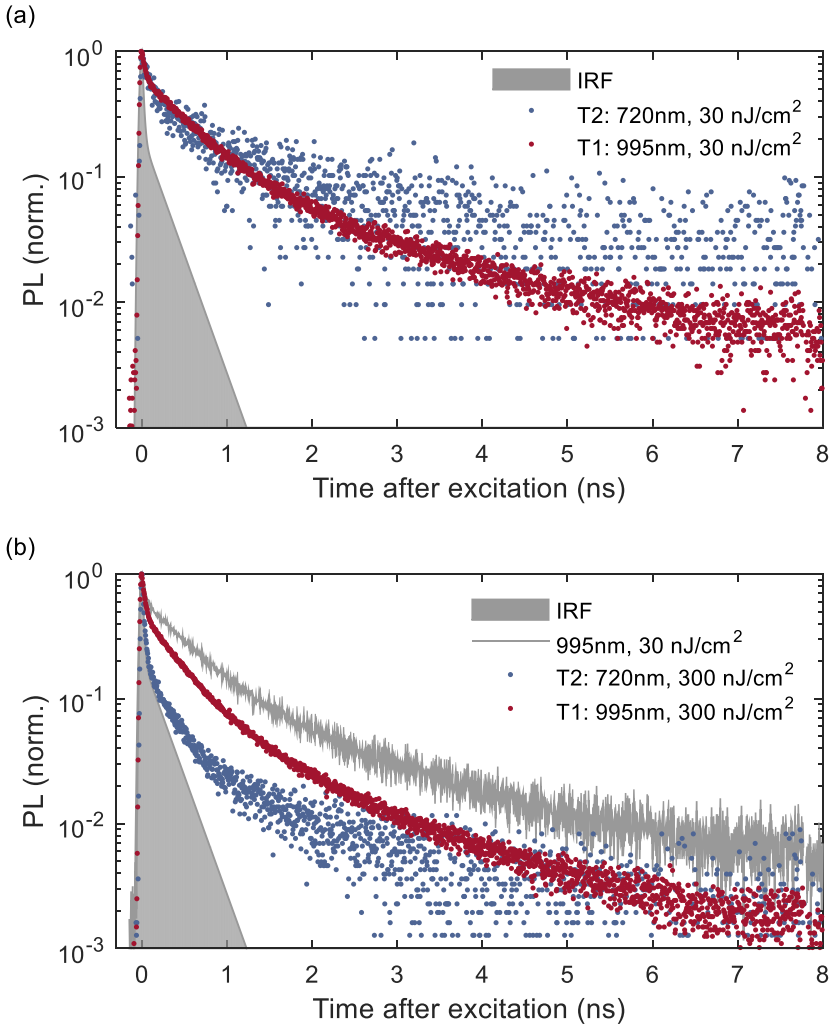

Figure 4.4. Time-resolved photoluminescence of the two PL peaks observed for $MASnI_3$ at 8K when excited with a 400 nm laser pulse with a fluence of (a) 30 $nJcm^{-2}$ and (b) 300 $nJcm^{-2}$, where the 30 $nJcm^{-2}$ decay curve is shown in grey for comparison.

The proposed mechanism of emission from charge-carrier recombination involving split-off bands has also been observed in the direct semiconductor GaAs,[171,172] which highlights the similarity of these perovskites with fully inorganic semiconducting materials.

4.2.2 Disorder

I examine the optoelectronic properties of $MASnI_3$ further by investigating changes in the emission linewidth with temperature, which reveals the influence of disorder and impurities. The PL linewidth (Γ) was determined from the full width at half maximum (FWHM) of the emission spectrum and is shown in Figure 4.5 as a function of temperature. I find Γ for $MASnI_3$ to be rather large, with a value of 180 meV at room temperature compared with 103 meV for $MAPbI_3$[173] and 50 meV for $CsSnI_3$.[174] In general, both homogeneous linewidth broadening (typically from phonons) and inhomogeneous broadening (from impurities and energetic disorder) may contribute to the overall width of the emission spectrum, as discussed in Section 2.4.3. The resulting emission linewidth is hence described by Equation 2.3. [127]

In the high-temperature range the phonon terms increase linearly with T (see Figure 2.7), which is contrary to the sub-linear dependence of the linewidth on temperature seen here. Such sub-linear behaviour is, however, accurately described by the functional form of the ionizable impurity term in Equation 2.3, suggesting that scattering of charge-carriers from ionized impurities such as tin vacancies is the predominant contribution to linewidth broadening in $MASnI_3$ above 110 K. Neglecting the phonon terms, I fit Equation 2.3 to the linewidth in the tetragonal phase for temperatures from 140-270 K. The best fit gives an impurity binding energy of 10 meV, but since the

temperature range fitted is small the value is only approximate and binding energies up to 20 meV are plausible.

The functional form of Equation 2.3 alone cannot account for the surprisingly abrupt linewidth narrowing below 110 K. I propose that since the linewidth in this material is dominated by impurities, the sudden change must be associated with a sharp decrease in number or change in binding energy of the defects below the phase transition. As mentioned previously, the most easily formed point defects in tin iodide perovskites are tin vacancies.[117,124] Removing a tin atom can contribute two holes to the valence band[117] if the resulting defect energy level lies close to the valence band, as predicted.[124] At sufficiently low temperature ($kT < E_b$) however, holes can potentially become localized to their acceptor ions (such as tin vacancies) making the defect charge-neutral and lowering the interaction with charge-carriers, as described in the above model. Hence the emission linewidth is expected to narrow as dopant charges localize. The abrupt change at the phase transition may indicate that a structural change makes it favourable for the holes to become localized, resulting in a sudden decrease in the density of holes in the valence band. This explanation agrees well with the increase in electrical resistivity that has previously been observed[115,163] when $MASnI_3$ was lowered below the transition into the orthorhombic phase at 110 K. The large change in linewidth at the phase transition, despite the absence of strong changes in band gap energy, is surprising. It suggests that relatively small changes in structure can suffice to suppress excess dopant carrier density in tin halide perovskites.

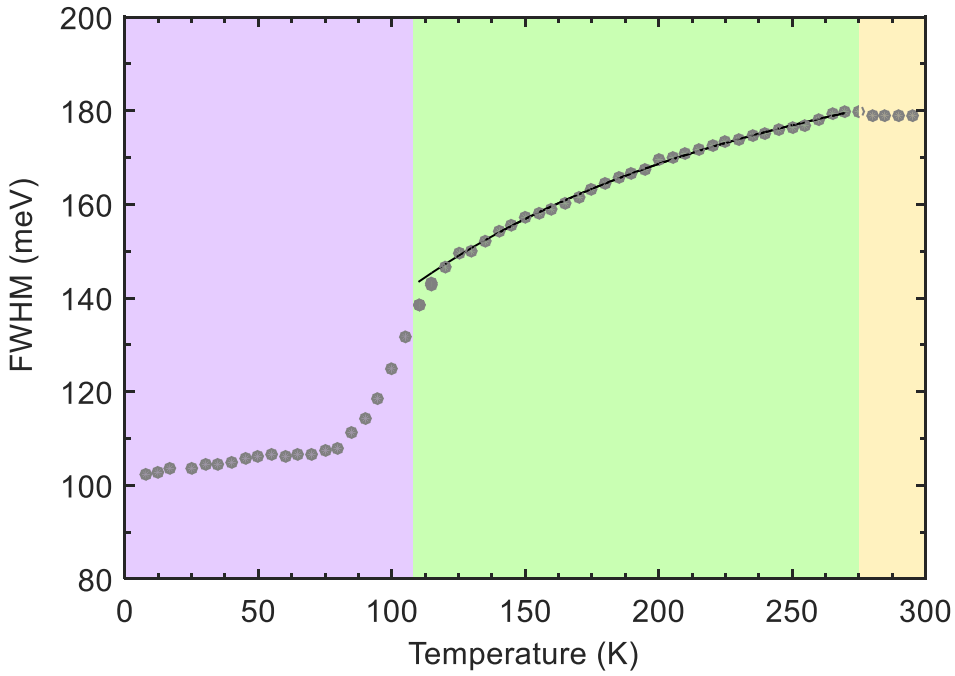

Figure 4.5. Spectral linewidth of PL emission corresponding to transition T1 in $MASnI_3$, determined by fitting a Gaussian to the PL spectra. The sample is excited with a pulsed laser at 400 nm with a fluence of 3 $nJcm^{-2}$ and spectra are collected at intervals of 5 K, cooling the sample from room temperature.

The temperature-independent inhomogeneous linewidth value (Γ_0 = 103 meV) approached at very low temperature reflects the sizeable disorder remaining in this phase, despite the improvement at the 110 K transition. The large contribution to the emission broadening in $MASnI_3$, from both ionizable defects (γ_{imp}) and temperature-independent disorder (Γ_0), is in stark contrast to $MAPbI_3$ for which the broadening is thought to be almost entirely homogeneous at room temperature.[173] Similar conclusions can be made when comparing the Stokes shifts between absorption onset and the emission peak observed for these two materials. Here, I find a large Stokes shift of almost 200 meV for $MASnI_3$ independent of temperature (Figure 4.2), whereas for $MAPbI_3$, Stokes shifts of at most 10 meV have been reported,[71] in accordance with significantly higher energetic disorder in the tin perovskite. Such contrast in defect densities has also been reported between copper indium gallium sulfide (CIGS) and copper zinc tin sulfide (CZTS), where defects in CZTS result in tail states that protrude into the band gap.[175,176] Tail states cause the peak PL energy to be considerably red-shifted from the absorption onset since carriers tend to thermalize into the tail states, which is typically accompanied by an undesirable lowering of charge-carrier mobility.

4.2.3 Charge-carrier lifetime

Finally, I investigate the effect of temperature-dependent doping and disorder on the charge-carrier lifetime. I measure time-resolved photoluminescence transients using time correlated single photon counting (TCSPC) after excitation with laser pulses of 400 nm wavelength, as shown in Figure 4.7a. Since the PL lifetime is very short, it is important to take account of the instrument response function (IRF) shown by the grey shaded area, which was obtained by measuring the response of the detector to laser pulses at 990 nm (near the detection wavelength). To obtain a corrected decay curve, I smoothed the data and IRF, and de-convoluted the two using a fast Fourier transform,

as described in Section 3.2.3. The time τ_e taken for the PL to decay to 1/e of its initial value (after IRF correction), is shown in Figure 4.7b as a function of temperature. The PL lifetime changes very little at temperatures above 110 K, remaining fixed at around 45 ps, which is considerably shorter than lifetimes for $MAPbI_3$ (typically on the order of 100-1000 μs).[63] The short carrier lifetime at room temperature is problematic for planar device architectures which require a long diffusion length for carrier extraction, although if the carrier mobilities are high enough, planar architectures will still be achievable.[55,177] In addition, the shape of the room temperature PL transients is independent of excitation fluence over a large measured range (0.3-300 $nJcm^{-2}$) as shown in Figure 4.6. This behaviour implies that monomolecular recombination is heavily dominant, rather than bi-molecular electron-hole recombination that would result in fluence-dependent dynamics.[40] Monomolecular recombination is expected to dominate when there is a high level of defects that act as recombination centers[40] (see Section 2.5.2) or there is a high background carrier density such that the photoexcited carrier density has little influence on the dynamics[55] (see Section 2.5.1). Hence the observed fast carrier recombination dynamics in this temperature region is compatible with the broad emission linewidth observed and the presence of a large tin vacancy density.

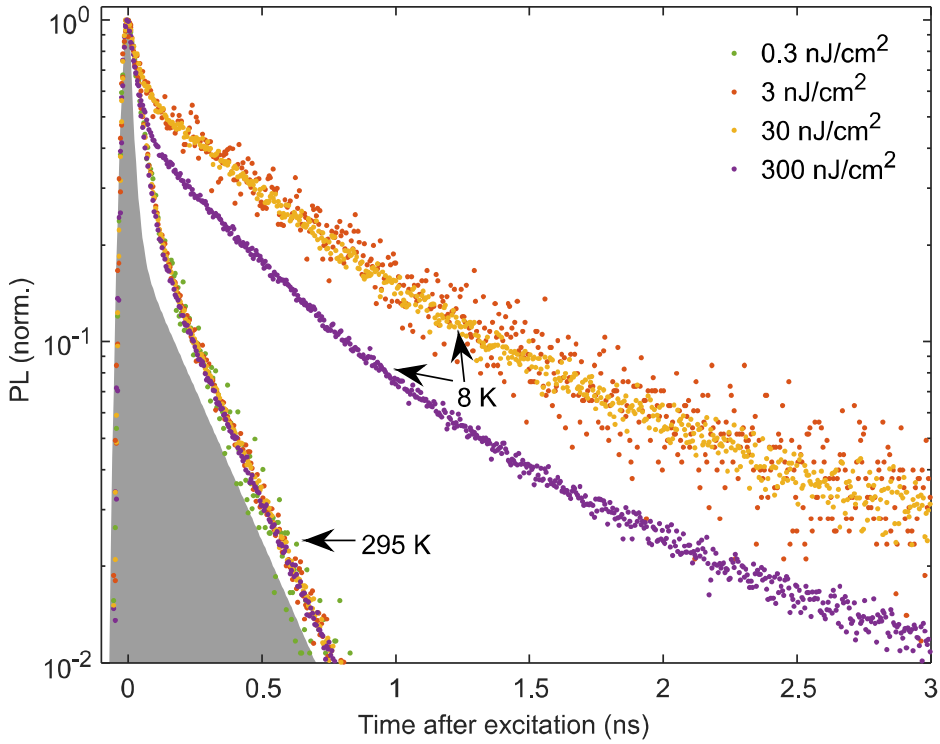

Figure 4.6. Fluence-dependence of the PL decay curve at room temperature and low temperature. The grey shaded area is the IRF.

Below ~110 K the lifetime increases steeply, reaching a value of around 275 ps at 8 K. Furthermore the dynamics become dependent on excitation fluence here (see Figure 4.6), suggesting the background carrier density is now lower. This explanation correlates well with the observed steep decline in emission linewidth discussed above. If, as already suggested, there is a change in the energy levels of the acceptor ions such that they are elevated further above the valence band maximum, it will become suddenly more favourable for the holes to be localized to these energy levels as the temperature is decreased, causing the hole density to drop. It is worth noting that a rise in lifetime at low temperature is also seen in CIGS and CZTS, with CZTS showing a thousand fold increase.[176] This is attributed to spatial electrostatic variations due to high levels of disorder or defects, which confines the carriers in different locations, providing a barrier to recombination which is overcome thermally as the temperature is increased. Hence charge-carrier lifetimes can sensitively depend on both recombination with a density of impurity-induced background carriers and the energetic disorder associated with such impurities.

Interestingly, this rise in carrier lifetime below the phase transition temperature concurs with the observed increase in intensity of the secondary PL peak T2 shown in Figure 4.7c, alluding to a common cause. This could simply be due to the interplay between the rate constants for recombination at the electronic transitions T1 and T2, which were discussed in Section 4.2.1. While T1 may be mostly dominated by electron recombination with the sizeable background hole density, T2 could be largely influenced by phonon-mediated interband transitions, e.g. between multiple conduction (or valence) bands. As a result, the relative rates may therefore be affected differently at the phase transition, imparting the observed changes in relative emission intensity (Figure 4.7c).

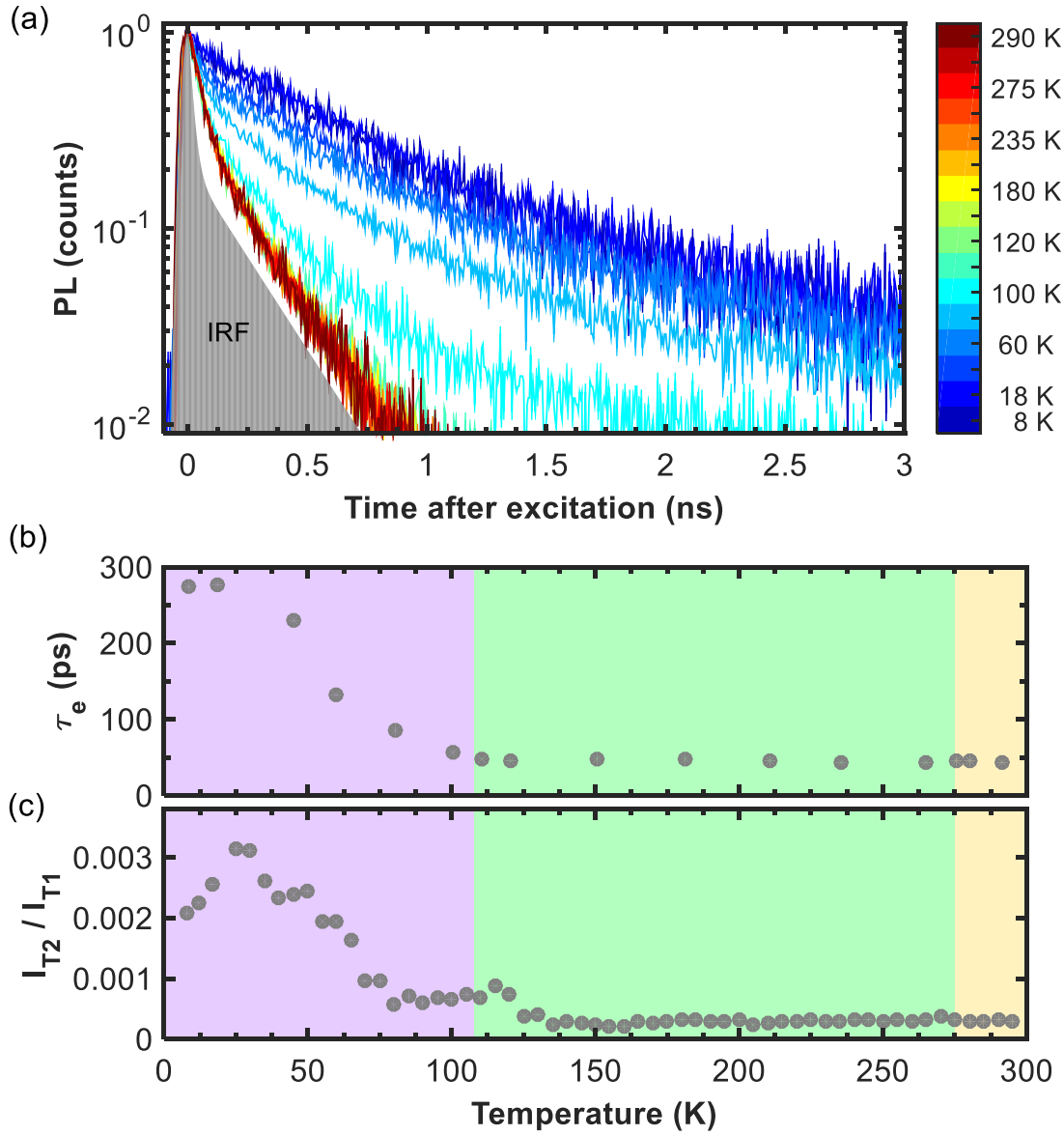

Figure 4.7. (a) Time-resolved photoluminescence (PL) as a function of time after excitation, from high temperature (red) to low temperature (blue). The instrument response function is shown by the shaded grey area. (b) PL lifetime determined as the time to reach 1/e of the maximum intensity. (c) Intensity at 1.726 eV corresponding to the second transition (T2) in comparison to the peak intensity per electron volt originating from the band gap transition (T1).

Taken together, these observations point to a significant change between the high and low temperature regime, which is induced by the phase transition at 108 K. I propose that all of these features – the increase in PL lifetime, the drop in FWHM, the appearance of PL from a secondary transition and the previously observed decrease in hole density[163] – are related to the presence of defects in the system (likely tin vacancies which have a low formation energy[117]). These defects scatter carriers, giving the photoluminescence a broad linewidth, and also p-dope the material, resulting in a large background hole density, which in turn leads to rapid charge-carrier recombination. These observations suggest that upon the transition into the orthorhombic phase, the relative alignment of the defects' energy level must change subtly with respect to the valence band edge. This change in energy level results in background holes becoming localized to defects which reduces their contribution to carrier scattering (emission linewidth decreases) and also reduces the p-doping (carrier lifetime increases). Further reduction in temperature freezes out more background holes such that the lifetime increases further. An understanding of the precise mechanisms inducing these effects is important as it may hold the clue to achieving similar effects at room temperature. Scattering between charge-carriers and impurities leads to reduced charge-carrier mobilities, whilst recombination of photoexcited electrons with background holes reduces charge-carrier lifetimes. In combination, these effects account for the significantly lowered charge-carrier diffusion length of only a few tens of nanometres observed for $MASnI_3$ at room temperature.[55] These measurements indicate that while the bandgap energy hardly changes at the phase transition near 110 K, the relative energetic alignment of defect levels with respect to the valence band edge is significantly altered. An understanding of how this favourable alignment is induced by

the structural changes could potentially allow for such effects to be replicated at room temperature through compositional changes.

4.3 Conclusion

In summary, I have evaluated the optoelectronic properties of $MASnI_3$ as a function of temperature to reveal the influence of impurities on charge-carrier scattering and recombination lifetimes. I find an abrupt improvement as the temperature is lowered into the orthorhombic phase below 108 K, where emission linewidths narrow and lifetimes increase significantly. I suggest that this effect is caused by a change to the energy level alignment of the tin vacancies with respect to the valence band maximum, leading to a reduction in background dopant density. First-principle calculations, that relate these effects to the structural changes anticipated at the phase transition, could hold the key to further material improvement. Since the perovskite structure allows for a range of organic/inorganic cations and halide anions to be combined with Sn^{2+}, a material combination may be found that replicates at room temperature the favourable change observed at the phase transition, allowing for low background hole densities. In addition, a weak but distinct above-gap luminescence peak is observed that coincides with the energy of a secondary absorption onset that is seen in similar form in many other hybrid metal halide perovskites. I propose that this emission originates from charge-carrier recombination involving a higher-lying band e.g. split off by spin-orbit coupling, similar to what has been observed for GaAs. The observation of such emission suggests that a certain fraction of charge-carriers exists for an appreciable time in a higher-energy state.

5 $FAPB_{1-x}Sn_xI_3$: CHARGE-CARRIER DYNAMICS AND BAND GAP BOWING

The results presented in this chapter have been published in:

Parrott, E. S.; Green, T.; Milot, R. L.; Johnston, M. B.; Snaith, H. J.; Herz, L. M. *Advanced Functional Materials*, 2018, 28 (33), 1802803

5.1 Introduction

In addition to holding impressive power conversion efficiency records in single-junction solar cells, metal halide perovskites have been developed for all-perovskite tandem cells with a record 4-terminal efficiency[52] of 23% and 2-terminal efficiency[53] of 18.5%. These achievements have been enabled by the widely tuneable band gap of mixed perovskites. To achieve the highest power conversion efficiencies, tandem solar cells require a narrow band gap semiconductor of around 0.8-1.2 eV to absorb the infrared portion of the solar spectrum[25] (see Section 2.1.2). To obtain such a low band gap from a metal halide perovskite, one may utilise the interesting phenomenon of band gap bowing observed when lead and tin perovskites are alloyed.[43] As discussed in section 2.3.1, there is little understanding of the cause of band gap bowing in metal halide perovskites at the present time. Clearly if these materials are to be optimized for

tandem devices, a greater understanding and control of the factors influencing the band gap are required.

Aside from the band gap, other properties of the mixed perovskites are important in determining how the material will perform in a photovoltaic cell, namely the charge-carrier lifetimes and PL quantum efficiencies. Lifetimes must be sufficiently long for carriers to be extracted before they recombine, and non-radiative recombination pathways must be minimised to achieve maximum efficiencies. All-perovskite tandem solar cells are limited in part by the poorer performance of perovskite materials containing tin.[44] For $MASnI_3$, poor device performance has been linked to very fast charge-carrier recombination, largely as a result of spontaneous p-doping due to the formation of defects such as tin vacancies (see Section 2.4.1).[55,95,122] However the presence of spontaneous doping in mixed metal perovskites is less clear as there are only a handful of reports of charge-carrier recombination lifetimes for mixed metal perovskites in the literature to date. $(FASn)_{0.6}(MAPb)_{0.4}I_3$ is shown to have a PL lifetime intermediate to that of $FASnI_3$ and $MAPbI_3$.[178] From optical pump terahertz probe spectroscopy the monomolecular and bimolecular recombination rates for $FASn_{0.5}Pb_{0.5}I_3$ also take intermediate values compared to values for 100% Sn or Pb reported elsewhere in the literature.[44] Zhao *et al.* show that metal composition has an impact on charge-carrier recombination mechanisms in $MAPb_{1-x}Sn_xI_3$, with 20-40% Sn having much weaker photoluminescence than other compositions, and all tin-rich compositions having short PL lifetimes.[88] They show that the dominant recombination mechanism at low intensity is Shockley-Read-Hall (SRH) recombination, but that at high intensity, the 60% Sn composition, which gives highest device efficiency, becomes dominated by radiative recombination (as determined from the diode ideality factor).[88] To reduce SRH recombination, a defect passivating electron transport layer can be used,

which has been shown to increase device efficiency for $MASn_{0.5}Pb_{0.5}I_3$.[53] Finally, increasing film crystallinity and thickness is reported to increase the lifetime by an order of magnitude[52]. The charge-carrier lifetimes and recombination mechanisms of $FAPb_{1-x}Sn_xI_3$ have not yet been systematically studied as a function of metal composition, although FA has been shown to be a good choice of cation in mixed tin-lead perovskites, improving stability[91] and PL lifetime,[58] and supporting single-junction photovoltaic (PV) devices that currently achieve PCEs of around 15%.[44,178]

In response to the broad lack of knowledge regarding these device-relevant materials, I investigate the optoelectronic properties of $FAPb_{1-x}Sn_xI_3$, through photoluminescence and optical absorption measurements across the tin-lead composition range at temperatures from 5 to 300 K. I highlight several key properties important for the improvement of mixed-metal halide perovskites and provide fundamental insights, through experiment and by drawing on the wealth of literature on traditional inorganic semiconductors. I report the structural phase transition temperatures as a function of composition, and show that the phase influences the magnitude of the bowing parameter and the gradient of the band gap with temperature. I show that the charge-carrier recombination dynamics can be split into two regimes – fast, mono-exponential recombination with a higher proportion of radiative recombination for tin-rich compositions and slower, stretched-exponential recombination for the lead-rich compositions. I also demonstrate that the charge-carrier recombination rate is almost temperature independent for $FASnI_3$, whereas there is strongly temperature activated non-radiative recombination in $FAPb_{0.75}Sn_{0.25}I_3$, which I attribute to multi-phonon assisted charge-carrier recombination.

5.2 Results and Discussion

5.2.1 Temperature-dependence of the band gap

I first explore the general behaviour of the band gap with temperature, for several compositions with varying tin content. I observe discontinuities in the PL and absorption edge for all compositions which I ascribe to phase transitions, similar to what has been seen in other hybrid perovskite materials.[71,149] These discontinuities are highlighted in Figure 5.1 on colour maps of the PL and in Figure 5.2 on the reflection-corrected absorption spectrum, at temperatures between 5 and 295 K. Figure 5.3c shows how the phase transition temperature changes with composition. The transitions of the end compositions agree with those reported in the literature; from PL[149] and X-ray diffraction[67] measurements for 100% lead and resistivity measurements for 100% tin[179]. The results show that the lowest phase transition temperature changes linearly with tin fraction between these end points. There is also a second discontinuity, only in $FASnI_3$, which may indicate a further phase transition at 170 K. This could correspond to the Pnma (orthorhombic) to P4/mbm (tetragonal) transition reported at around 150 K by Schueller *et al*.[68] Schueller also reports a transition to a cubic structure at 250 K which from these results appears to have no influence on the PL. Comparing the other transitions with those reported in literature, $FAPbI_3$ is thought to be in a trigonal space group at low temperature, with a gentle transition to another trigonal space group, beginning at 100 K and completing at 175 K on heating,[67,149] which is in accordance with my results. Across the compositions at room temperature there is thought to be a structural change from the space group P3m1 (trigonal) for lead rich compositions to Amm2 (orthorhombic) for tin rich compositions[69,180], in the region of 25% tin.[44]

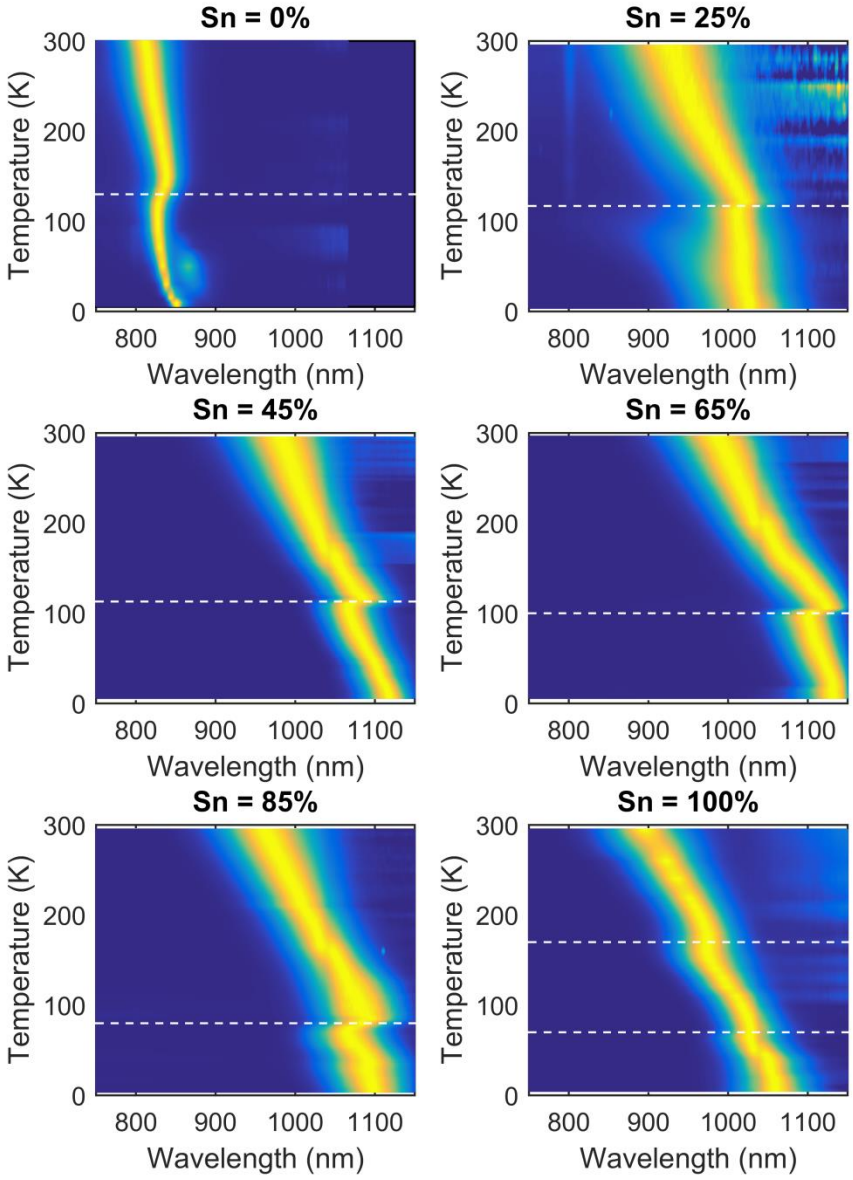

Figure 5.1. Colour plots of normalized PL intensity (yellow/lightest = 1, blue/darkest = 0) for $FASn_xPb_{1-x}I_3$ where x is given as a percentage above each figure. Samples were excited at 400 nm, 1 W cm^{-2}. Discontinuities in the PL are marked with white dashed lines and assumed to be phase transitions.

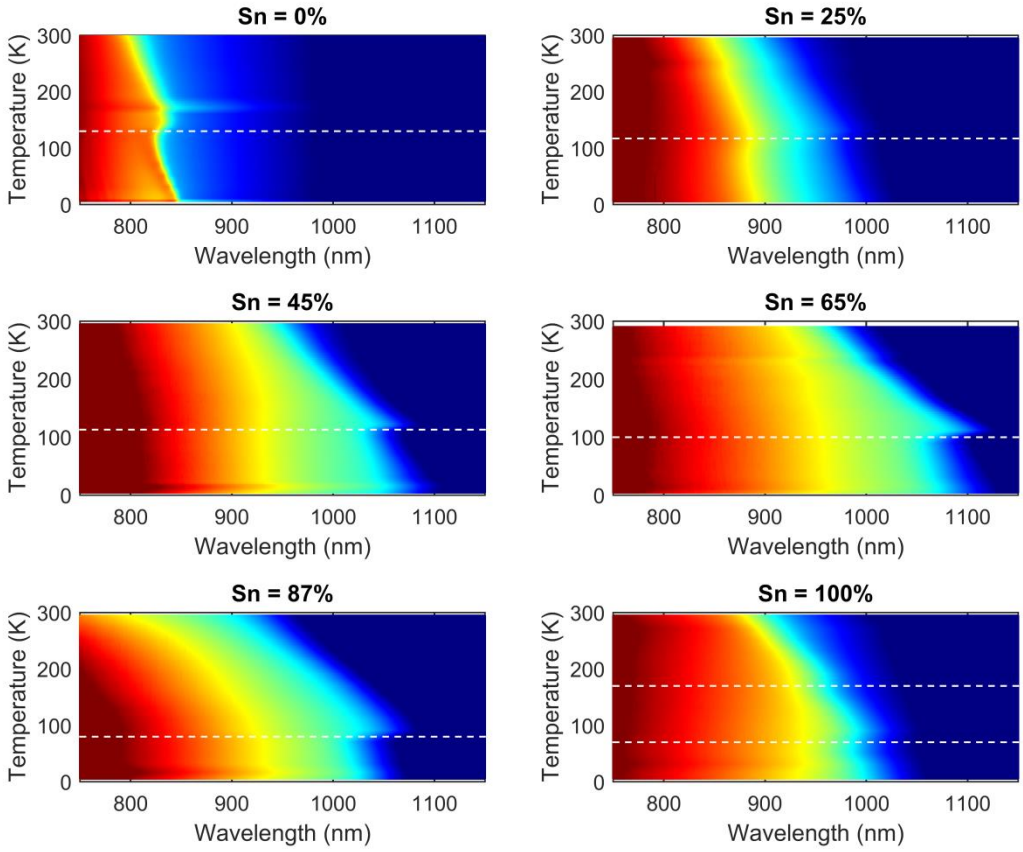

Figure 5.2. Colour plots of absorption spectra (red is highest value, blue is lowest value) for $FASn_xPb_{1-x}I_3$ where x is given as a percentage above each figure. Discontinuities in the absorption edge are marked with white dashed lines and assumed to be phase transitions.

However, in other studies $FASnI_3$ has been reported to have cubic structure ($Pm\bar{3}m$) at room temperature,[68] including in single crystals.[59,179]

Apart from the discontinuities at the phase transitions, the band gap changes linearly with temperature. For all compositions, I observed that both the PL maximum and absorption onset blue-shift as the temperature is increased, implying an increasing band gap in contrast to the Varshni formula. This has been observed for all other metal halide perovskite semiconductors, as discussed in Section 1.3.2.

Figure 5.3b shows the gradient of the band gap with respect to temperature in the highest and lowest temperature phase (as determined from linear fits to the absorption edge energy in Figure 5.4). In the room temperature phase, the band gap of the 100% tin composition is the most sensitive to temperature (steepest gradient) and 100% lead the least, with the gradients of the mixed compositions linearly interpolating between the two. However, in the low temperature phase the gradient is smallest for the 65 and 85% Sn compositions. The phonon modes are thought to be relatively constant in the different phases of $FAPbI_3$,[94] and these results show the temperature gradient is also the same in both phases measured. The tin-containing compositions all have different values of the temperature gradient for the two phases, which may indicate that the phonon modes are also different.

It is also worth noting that the minimum gradient in the low temperature phase coincides with the minimum band gap energy and seems to approximately follow the bowing in Figure 5.5a. If the main contribution to the temperature dependence of the band gap is in fact lattice expansion, this could suggest hindered thermal expansion in the mixed compositions, possibly as a result of local strain to accommodate the different metal ions, which is also a factor that causes band gap bowing.

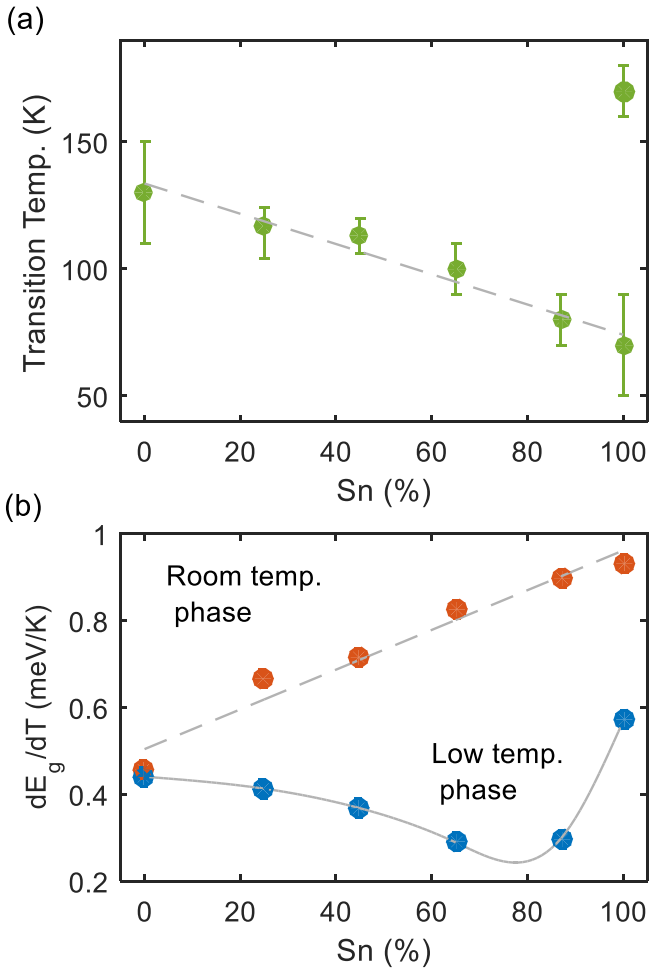

Figure 5.3. (a) Phase transition temperatures for each tin composition, found from the discontinuity in PL and absorption edge energies when heating the sample from 4 K to room temperature. The error bars indicate the temperature range over which the discontinuity is found. (b) Gradient of the absorption edge with respect to temperature for each composition in its room temperature phase and lowest temperature phase.

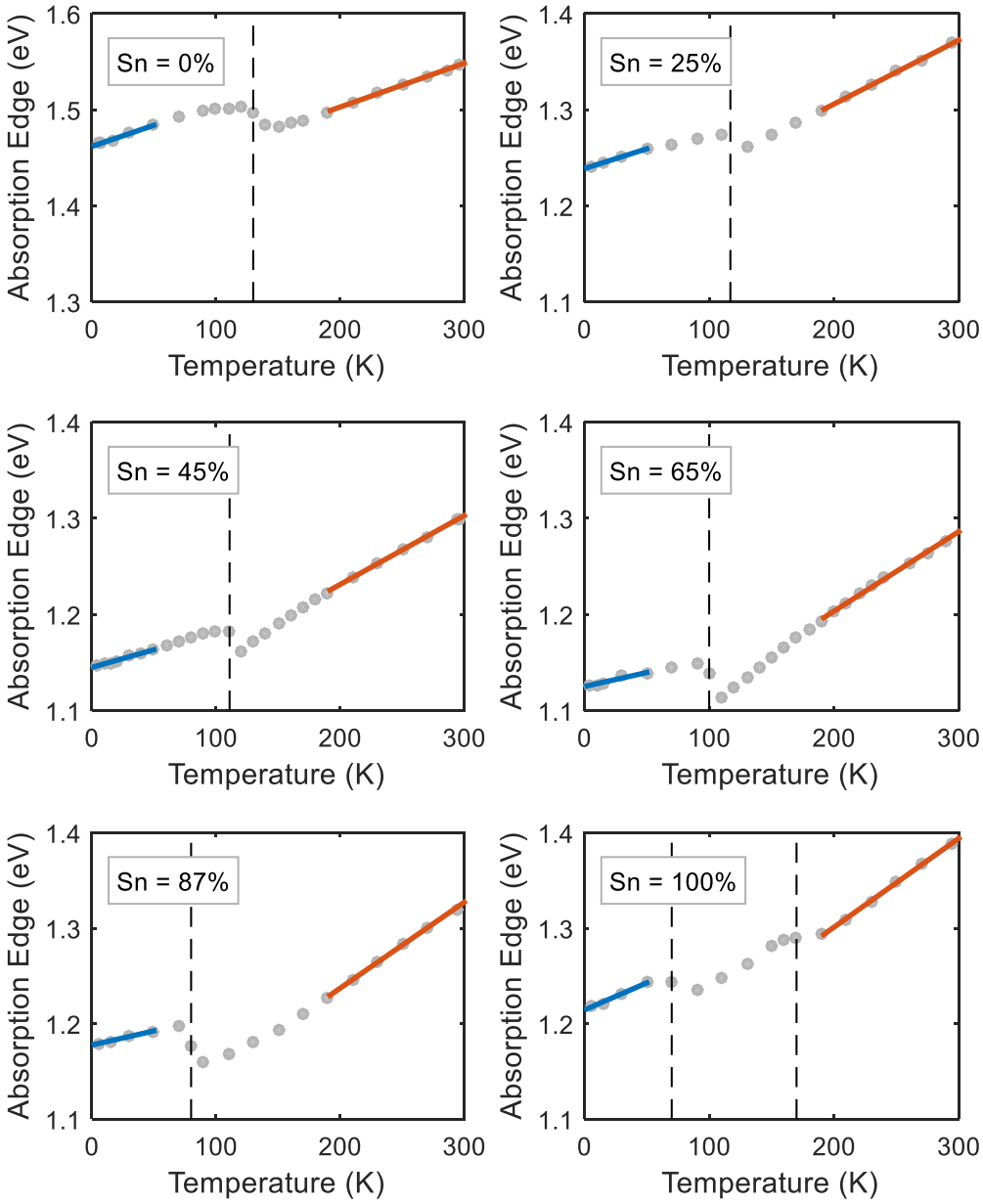

Figure 5.4. Optical band gap determined from absorption edge energies for each composition of $FASn_xPb_{1-x}I_3$. Blue and red lines show the fit used to calculate the band gap gradient shown in Figure 5.3 at high and low temperature.

5.2.2 Changes in band gap bowing with temperature

Given that both the structure and the temperature influence the band gap, it is interesting to investigate how the bowing is affected. To determine the band gap bowing parameter *b*, I fit Equation 2.1 to the absorption onset energy across the 6 compositions at a given temperature. Example fits are shown in Figure 5.5a for high and low temperature. I confirm that there is significant band gap bowing, with the middle compositions having lower energy than the pure compositions, across all temperatures. Band gap bowing has sometimes also been referred to as an 'anomalous' band gap, but in fact it is simply the result of the generally applicable equation for semiconductor band gaps (Equation 2.1), for a large value of *b*. Metal halide perovskites are essentially crystalline semiconductors, therefore it is informative to make a comparison with other materials that display band gap bowing. As discussed in Section 2.3.1, local distortions to the bond angles caused by unequally sized alloy atoms can result in band gap bowing which is approximately parabolic. In metal halide perovskites the bond angles, specifically the tilting of the octahedra, have been shown to be important in determining the band gap[46,87,181] and may provide a rationale for the large bowing parameter. DFT has been used to calculate bowing in $FAPb_{1-x}Sn_xI_3$ for a 2x2x2 supercell with some success despite the small size.[44] However, more in-depth calculations are required to allow for a full understanding of such effects in hybrid metal halide perovskites.

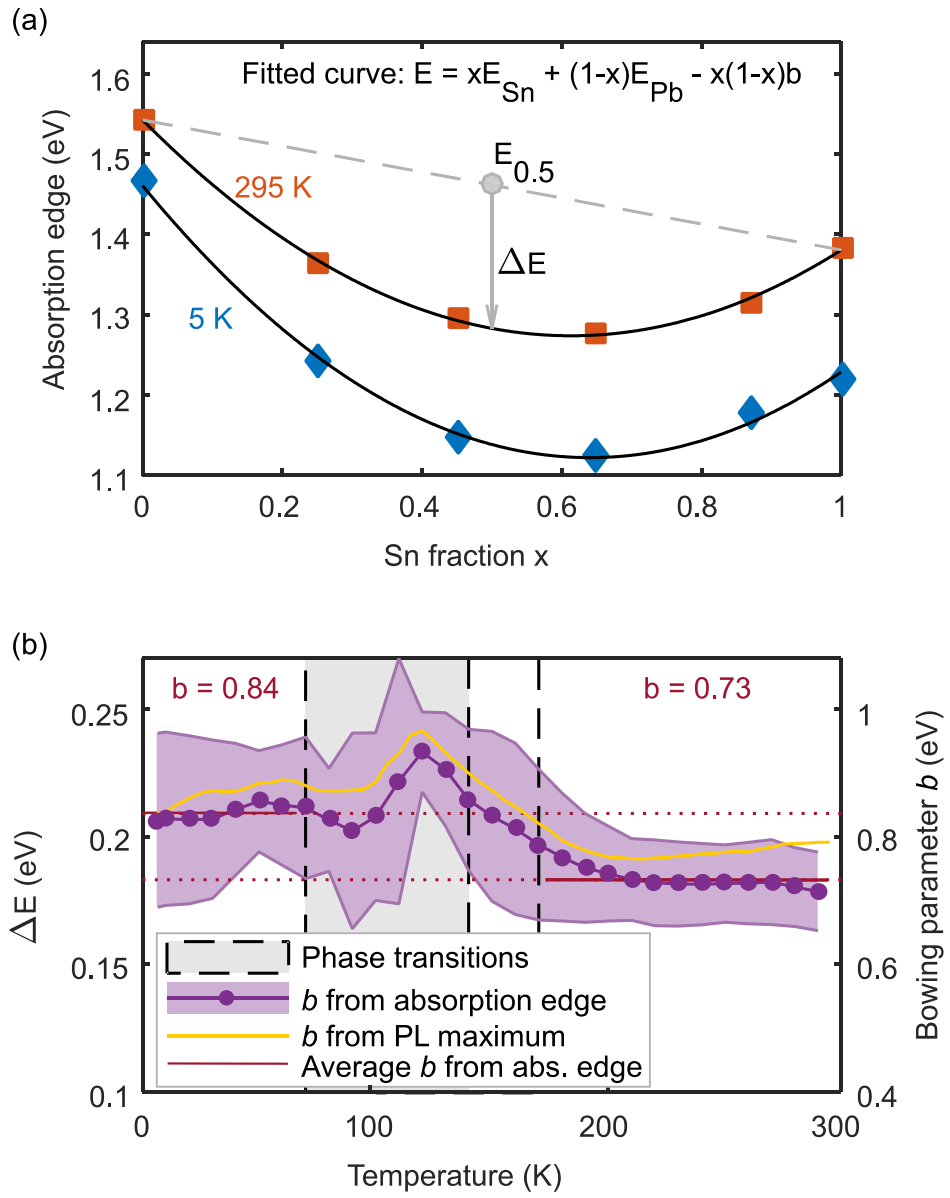

Figure 5.5. (a) Absorption edge of $FAPb_{1-x}Sn_xI_3$ at high (red squares) and low (blue diamonds) temperature. Black lines show fitted parabolas that determine the bowing parameter *b*. The dashed line shows the expected energies if the band gap changed linearly, and ΔE is the maximum deviation from linear (always at 50% Sn), which equals *b*/4. (b) Bowing parameter calculated from fitting a parabola to the absorption edge energy (purple circles), and the energy of maximum PL intensity when excited at 400 nm with a fluence of 14 $nJcm^{-2}$ (yellow line) of all compositions, at each temperature. The purple shaded area shows the 95% confidence limit of the fit to the absorption edge data at each temperature point. The black dashed lines show the temperature region in which the phase transitions of the different compositions occur, and the extra phase transition of $FASnI_3$. The red line shows the average bowing parameter in each phase.

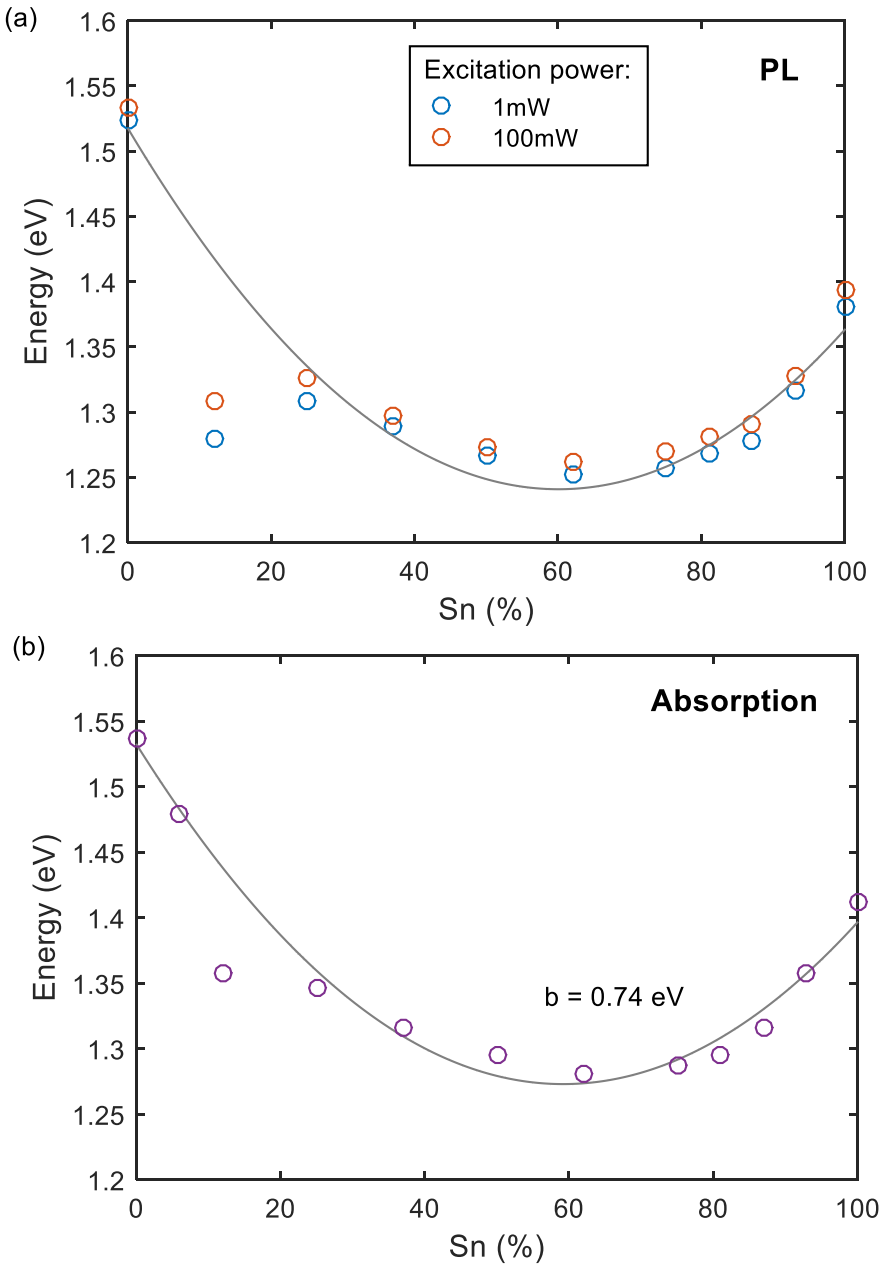

Figure 5.6. (a) PL peak energy for 12 compositions of $FASn_xPb_{1-x}I_3$, measured for 400-nm laser excitation intensities of 1 W/cm^2 (blue circles) and 110 W/cm^2 (orange circles) at 300 K. The grey line is a fitted parabola. (b) Absorption onset energy (purple circles) and a fitted parabola (grey line).

The other cause for band bowing discussed in Section 2.3.1 is the band anti-crossing model. It is worth noting that these data are well represented by the parabolic model of bowing at all temperatures. It is therefore unlikely that the band anti-crossing model of bowing is applicable here, since this characteristically results in highly non-parabolic bowing, with a sudden drop in band gap at one end of the composition range, which is not observed for the tin-lead perovskites at any composition or temperature.

To determine the effect of temperature on band gap bowing, I extract the bowing parameter *b* from both PL and absorption data, as shown in Figure 5.5b as a function of temperature. In the shaded temperature region, individual compositions undergo phase transitions at different temperature, with the corresponding jump in band gap leading to strong fluctuations of the extracted bowing parameter. However, outside of this intermediate range, I observe a roughly constant bowing parameter in both the low temperature region (~0–70 K) and the high temperature region (~170–300 K) within which no phase transitions occur. Absorption data indicate a bowing parameter of 0.73 eV for the high temperature phase and 0.84 eV for the low temperature phase as indicated in Figure 5.5, highlighting the influence of crystal structure on the extent of band gap bowing.

To confirm this result at room temperature, I measured the PL and absorption spectra for an additional batch of samples, this time containing 12 compositions with varying tin content (0, 6.25, 12.5, 25, 37.5, 50, 62.5, 75, 81.25, 87.5, 93.75 and 100%). The PL peak energy and absorption edge for these compositions are plotted in Figure 5.6. All compositions, except the 12.5% Sn sample which will be discussed in section 5.2.3, have absorption edges which approximately fit a parabola with a band gap bowing parameter of 0.74 eV, which is within the error of the room-temperature value of 0.73 eV calculated above.

Overall, I conclude that band gap bowing in tin-lead perovskites is likely to arise from bond bending to accommodate the random placement of lead and tin ions, given the parabolic nature of the large bowing observed for all temperatures. The bowing parameter is largely constant with temperature for regions in which all compositions do not exhibit structural phase transitions. However, crystal structure clearly has an effect on the magnitude of the bowing parameter, possibly through its influence on bond angles, suggesting that small structural changes, e.g. through A-cation choice, may be used to optimize desired bowing effects.

5.2.3 Changes in emission spectra with tin-lead composition

I proceed by considering the influence of composition on disorder and PL quantum efficiency, which are highly important parameters for optimized power conversion efficiency of solar cells.

In section 5.2.2 I noted that the sample containing 12.5% Sn had a lower band gap than expected, which could be due to disorder in the material. Figure 5.7 shows that this sample also has a high FWHM, large Stokes shift and low PLQE, all of which can suggest inhomogeneity. When the intensity of the excitation source is increased from 1 to 110 W/cm^2, a blue shift and an increase in FWHM is expected as states available for charge-carriers are filled. However the 12.5% Sn material shows a narrower FWHM at high power, suggesting that only sub-band-gap states are contributing to the PL at low powers. The inhomogeneity may be due to the presence of the yellow δ-phase. The Goldschmidt tolerance factor is 1.001 for $FAPbI_3$ and 0.998 for $FASnI_3$[182], suggesting that the formation of the δ-phase, which is thought to be stable for tolerance factors greater than 1,[183] is more likely for lead-rich perovskites, suggesting that alloying with tin may be beneficial in achieving a stable perovskite phase. However since material

processing routes have a large influence on the formation of the δ-phase, this is not considered to be an intrinsic property of the material. Annealing at a higher temperature may potentially eliminate the δ-phase.

Aside from the presence of sub-band-gap states in the 12.5% sample, there are several other points of interest in the spectral broadening, Stokes shift and the PLQE which I discuss below.

Spectral broadening

The PL linewidth data (Figure 5.7a) show that the 100% tin and 100% lead iodide perovskites have much sharper PL spectra than those of their alloys, indicating higher disorder for mixed metal compositions. This observation is in agreement with the model discussed above, which assumes that random placement of tin and lead atoms on metal sites in the perovskite lattice is the main cause of band gap bowing effects. From intuition and previous DFT calculations[44], one would expect the linewidth to be broadest for the 50% composition, whereas in fact I find the broadest linewidth in the mixed compositions with Sn <25% and >85%. Since many material quality factors affect material disorder, this effect is likely to arise from extrinsic factors that can be improved with further crystal growth optimization, such as ensuring there are no inclusions of the yellow δ-phase in the lead-rich compositions.[44,183] Interestingly the PL linewidth of $FASnI_3$ is similar to that of $FAPbI_3$, and much narrower than that observed in Chapter 4 for $MASnI_3$[95] suggesting that $FASnI_3$, (as prepared here with excess SnF_2) may be less disordered and therefore able to support higher device efficiencies than its MA equivalent.

Stokes Shift

The Stokes shift between emission peak and absorption edge is found to rise steeply when tin is added, then drops again and stays approximately constant for 40-100% tin content (Figure 5.7b). The large Stokes shift for materials with 6-12% Sn content

suggests that a significant fraction of the PL originates from sub-band-gap states as discussed above. Potential explanations for these sub-band-gap states could be a re-alignment of the level of trap states with respect to band edges as a small quantity of tin is added, or a structural instability (e.g. deterioration into a δ-phase) causing an energetically disordered landscape. Particle size effects can also contribute to a change in Stokes Shift for crystal sizes on the order of 10 nm and below,[184] but since the thickness and grain size for these films are in the 100-500 nm range,[44] I do not expect to see this effect.

Quantum Efficiency

The PL quantum efficiency (PLQE) is of particular interest for solar cell applications because the presence of non-radiative recombination in the semiconductor implies there will be detrimental recombination in the photovoltaic device; therefore a higher PLQE of an absorber material will generally allow for higher PCEs. Here I examine relative PLQE values by dividing the luminescence intensity by the excitation power, across the tin-lead composition range. Figure 5.7c shows that the relative PLQE drops by almost 2 orders of magnitude when only 6% tin is added to $FAPbI_3$, but then rises exponentially as the tin content is increased. The sudden drop in PLQE for small additions of tin may have similar causes to those leading to the large Stokes shift for these compositions, e.g. an unfavourable re-alignment of trap levels or increase in their density, or an increase in energetic disorder. As I show in section 2.4.1, the subsequent rise in PLQE with increasing tin content above 50% can be mainly understood in the context of an increased density of background holes present caused by spontaneous doping, which has been associated with the propensity of the material to form Sn vacancies[117,122]. As a result, $FASnI_3$ has the highest PLQE in the series, being 10 times brighter than $FAPbI_3$.

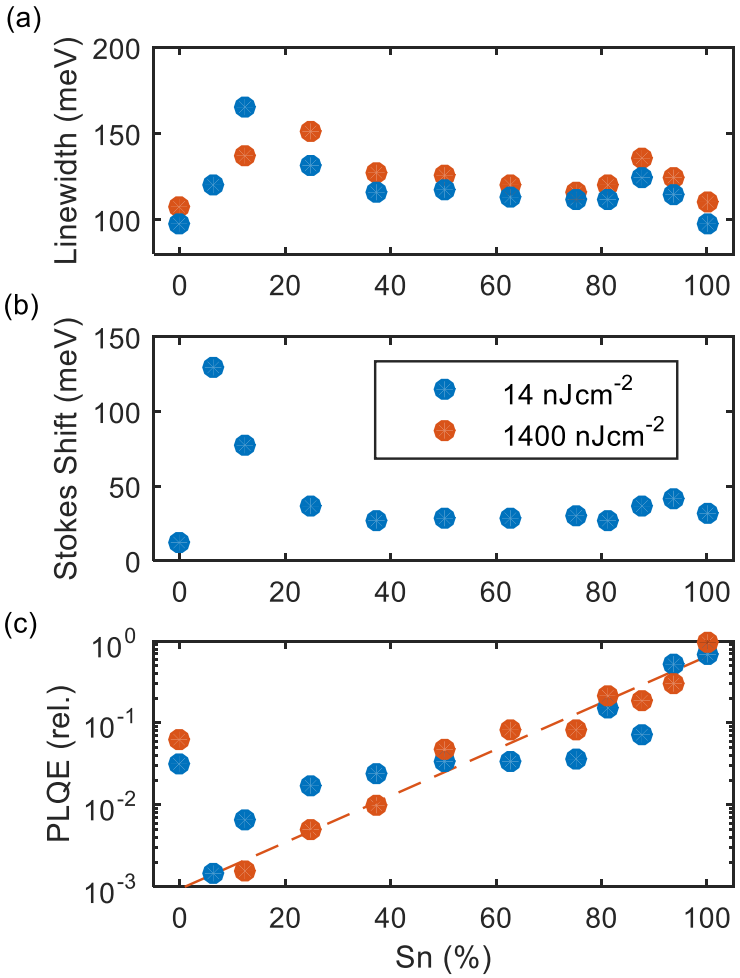

Figure 5.7. (a) Full width at half maximum of the PL spectrum for each composition of $FAPb_{1-x}Sn_xI_3$, excited at 400 nm with a fluence of 14 nJ cm^{-2} (blue) and 1400 nJ cm^{-2} (red). (b) Stokes shift of the same compositions determined by the difference between the absorption edge and the PL peak (400 nm, 14 nJ cm^{-2}). (c) Relative photoluminescence quantum efficiency (PLQE) for the same compositions, excited at 400 nm with a fluence of 14 nJ cm^{-2} (blue) and 1400 nJ cm^{-2} (red). The PLQE is normalized to the value for 100% Sn, measured at 1400 nJ cm^{-2} fluence. The dashed line shows an exponential fit to the high fluence data, excluding the 0% Sn point.

5.2.4 PL transients as a function of tin-lead composition

The PL transients of the different tin-lead compositions, fitted with a stretched exponential function, are shown in Figure 5.8. The extracted effective lifetime and stretch parameter are plotted in Figure 5.9, which demonstrates that the charge-carrier recombination kinetics fall into two distinct compositional regions: a lead rich region with Sn <50% that exhibits stretched decay curves ($\beta < 1$) and longer lifetimes, and a tin rich region with mono-exponential decay curves ($\beta = 1$) and short lifetimes. Two of the compositions luminesce too weakly to be able to measure the PL decay under the same conditions, so data was measured at higher laser fluence. Even at higher power, the exponential is considerably stretched, and the PL exhibits a fairly long lifetime, similar to the other compositions with <50% Sn content, shown in Figure 5.8.

Since the tin rich compositions have reduced lifetimes, I conclude that their higher PLQE is caused by a relative increase in radiative recombination rate, rather than a decrease in non-radiative recombination rate. A survey of the literature values reveals that the apparent radiative bimolecular recombination constant k_2 is twice as large for $FASnI_3$[135] than $FAPbI_3$[131], with an intermediate value for a composition with 50% Sn[44]. Therefore, an enhancement in radiative recombination for tin-rich samples could be partly accounted for by enhanced band-to-band recombination. However, such effects cannot fully account for the order of magnitude rise in PLQE between the lead and tin perovskites. I therefore attribute the increased luminescence of the tin-rich compositions to enhanced radiative recombination mediated by hole doping, an explanation which is consistent with Hall measurements[115,185] and other techniques[55,135] that have reported high doping densities for various tin-based perovskites, although such effects may be reduced substantially through suitable processing methods.[59,69]

In addition, analysis of the stretch-parameter β (Figure 5.9c) can yield interesting insights into the mechanisms for charge-carrier recombination. For a typical radiative bimolecular recombination value of $k_2 = 10^{-10}$ cm^3s^{-1}, an initial carrier density of 10^{19} cm^{-3} would be needed to produce a stretched curve on this time scale (see Section 2.5 and Figure 2.9). This is much larger than the maximum value of 10^{17} cm^{-3} used here, suggesting that the decay is not stretched due to radiative bimolecular recombination. In addition, I will show in Section 5.2.5 that the non-radiative recombination rate when excited with a fluence of 14 nJ cm^{-2} exceeds the radiative rate by at least a factor 100 across all compositions at room temperature and hence it is the trap-mediated recombination that determine the dynamics. The non-radiative recombination of charge-carriers in semiconductors is generally described by the Shockley-Read-Hall (SRH) model, as described in Section 2.5.2.[125] For many cases, the common assumption of a constant charge-carrier recombination rate k_1 (as in Equation 2.4) is a good approximation to SRH recombination, applicable to many situations such as extrinsically doped semiconductors, and leads to mono-exponential decay dynamics. However the full SRH formula has a more complex dependence on the photoexcited carrier density Δn that can result in non-exponential charge-carrier decay, e.g. for the case of intrinsic semiconductors with shallow traps described by Equation 2.9. Alternatively, non-exponential PL decay is also possible when the PL dynamics are determined by trap-filling rather than trap-assisted recombination (see Section 2.5.4).[136,146] For lead triiodide perovskites, theoretical calculations have previously found the typical defect states to be very shallow[138] and the doping level to be intrinsic[137], which is consistent with the stretched-exponential behaviour I observe for the lead-rich compositions. Hence the transition to mono-exponential decays for tin-rich

compositions could be caused either by the substantial increase in doping density that I have already proposed, or by an increase in trap depth.

Overall, the observation of two distinct regimes for the stretch-parameter β suggests that there is a substantial change in the nature of defect formation at around 50% Sn. Based on the enhanced PLQE and shorter lifetimes for high tin content, this change is likely to cause or be accompanied by a change in doping density. A recent study investigating the stability of $FAPb_{1-x}Sn_xI_3$ showed that compositions with less than 50% Sn were far more air-stable than tin-rich compositions, as a result of two different degradation mechanisms dominating in the two different regimes.[119] Although I did not intentionally expose the samples to air during either fabrication or measurement, spontaneous defect formation would follow similar thermodynamic considerations. Hence a switch in the nature of the defects between tin-rich ($x > 0.5$) and lead-rich perovskites ($x < 0.5$) is also the most likely explanation for the change in the shape of the decay transients I observe here.

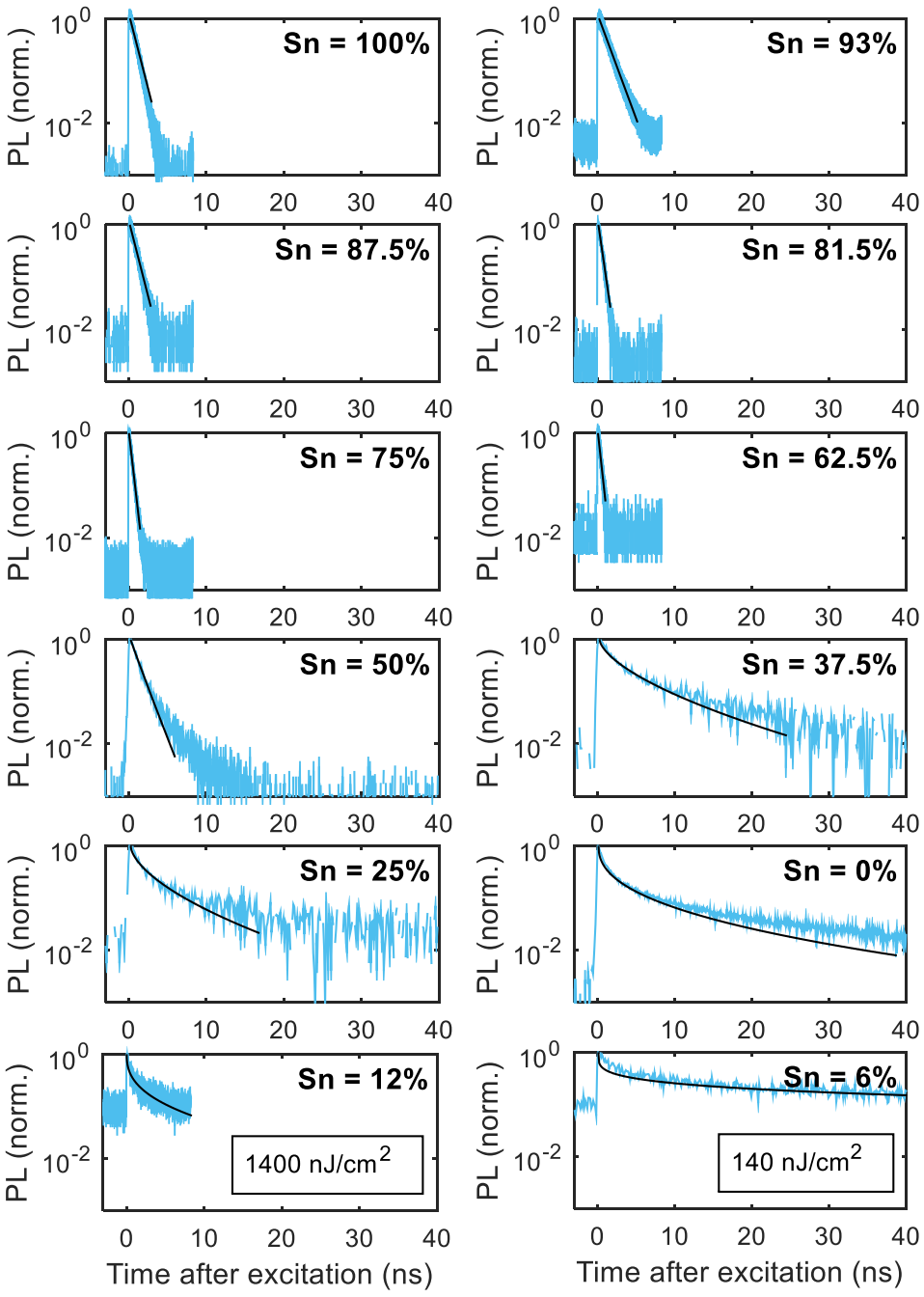

Figure 5.8. PL decay curves for a range of $FASn_xPb_{1-x}I_3$ compositions, excited at 400 nm, with 14 nJ/cm^2 per pulse, except the bottom two panels which are excited at higher fluence (labelled) since the radiative efficiency is very low. Stretched exponential fits are shown by black lines.

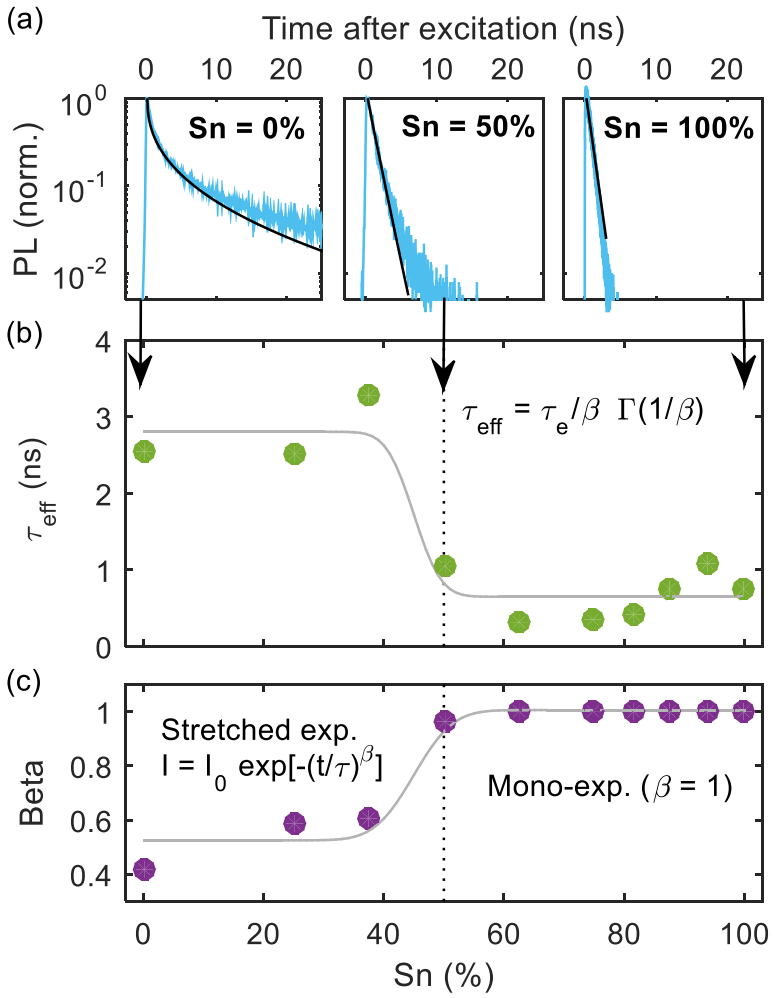

Figure 5.9. (a) Example PL decay curves (blue) of $FAPb_{1-x}Sn_xI_3$ compositions at room temperature when excited at 400 nm with 14 nJ/cm^2 excitation power, fitted (black) with a stretched exponential ($I = I_0 \exp(-(t/\tau)^{\beta})$), where beta is the stretch parameter. The rest are shown in Figure 5.8. From these fits, (b) shows the PL effective lifetime ($\tau_{eff} = \tau/\beta\ \Gamma(1/\beta)$ where Γ is the gamma function) and (c) the stretch parameter. Perovskites containing only 6.25 and 12.5% Sn were too weakly luminescent to be measured at this excitation intensity, but could be examined at a higher excitation intensity for which they also exhibit a long PL lifetime and stretched decay (Figure 5.8).

5.2.5 PL transients as a function of temperature

To allow for an identification of trap-mediated charge-carrier recombination mechanisms, I investigate the temperature dependence of the PL dynamics. PL transients were measured for two compositions (25% and 100% Sn) at temperatures between 5 and 295 K for low and high fluences of 14 nJ cm^{-2} and 1400 nJ cm^{-2} (Figure 5.10). Figure 5.11a-b show values of the extracted effective PL lifetimes as a function of temperature.

I find that the effective PL lifetime increases with decreasing temperature, for all compositions investigated, but more so for the lead-rich sample than for the 100% Sn perovskite whose PL lifetimes show only weak dependence on temperature. To investigate whether such effects are the result of changes in radiative or non-radiative decay pathways, I also recorded the relative PL quantum efficiencies as a function of temperature, shown in Figure 5.11c. The observed strong increase in relative PLQE for the 25% Sn perovskite with decreasing temperature indicates that the concomitant increase in PL lifetime is mostly related to a decrease in the non-radiative (trap-mediated) recombination rate (k_1^{nr} in Equation 2.6). Similar observations have previously been made for $MAPbI_3$ for which k_1 was shown to decrease upon cooling,[71] and for $FAPbI_3$ where the PLQE was shown to have a similarly strong temperature dependence.[149]

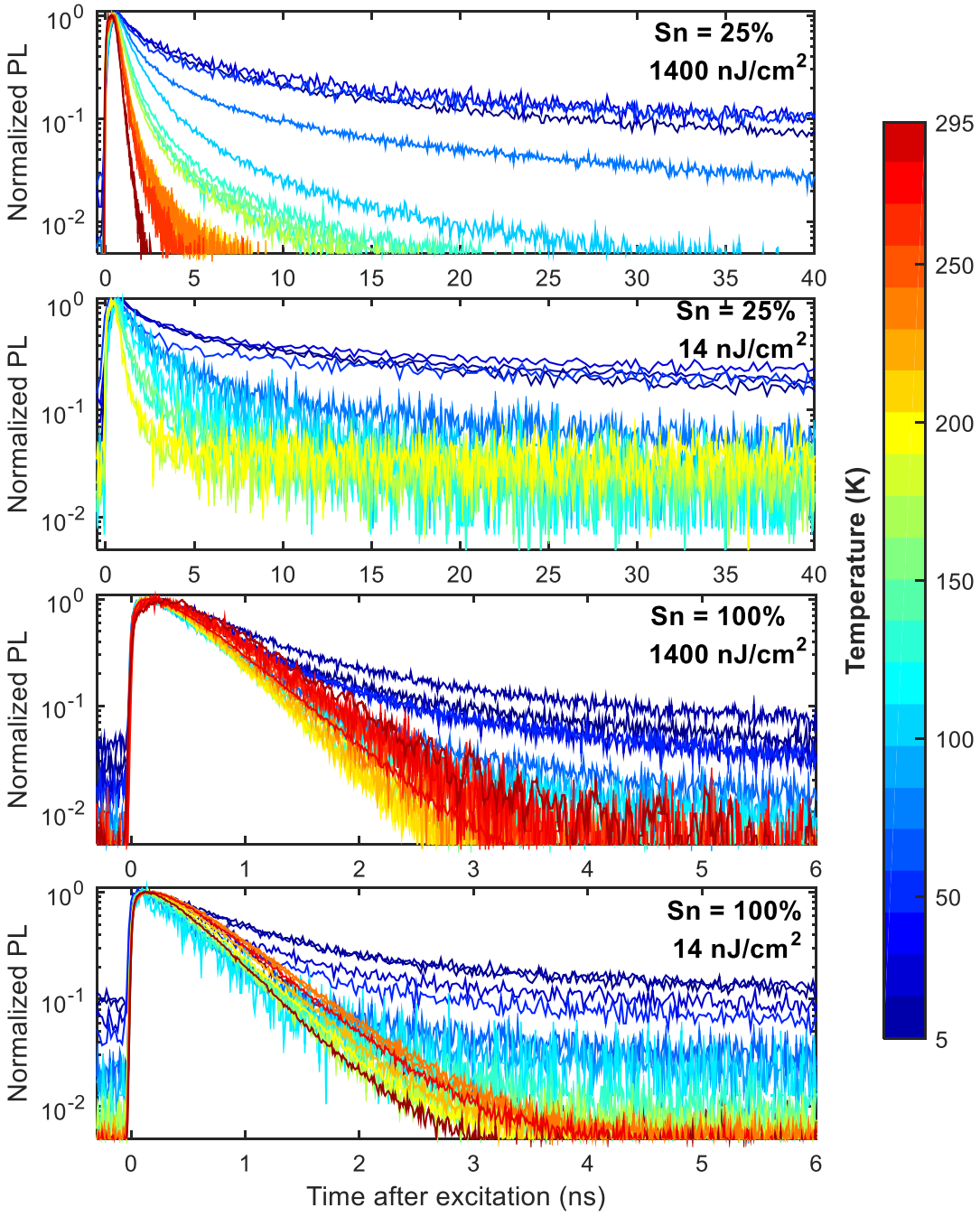

Figure 5.10. Temperature dependent PL decay curves for two $FASn_xPb_{1-x}I_3$ compositions, excited at 400 nm with a fluence of 1400 nJ/cm^2 or 14 nJ/cm^2. The temperature is indicated by the corresponding colour on the colour bar.

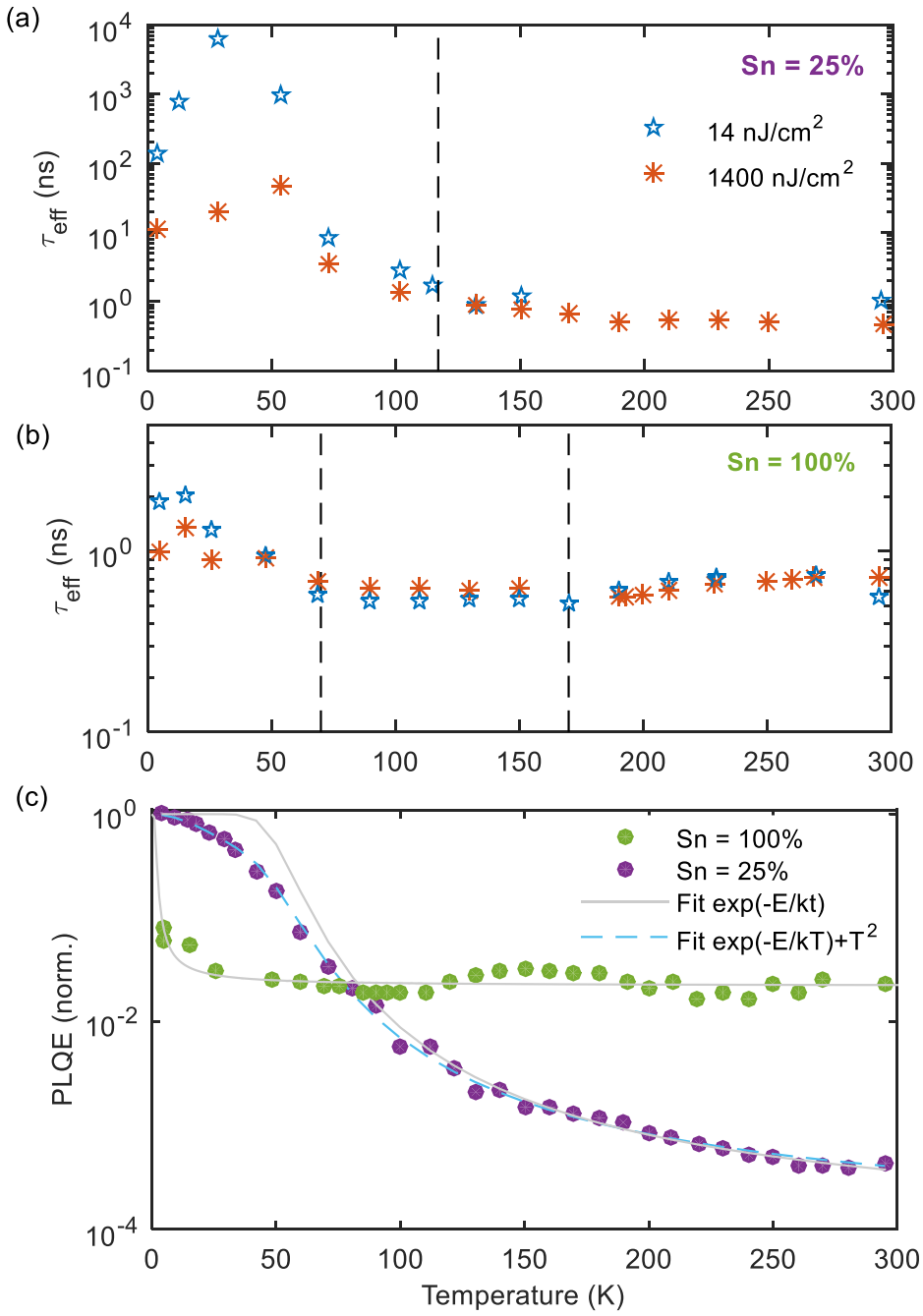

Figure 5.11. (a,b) Effective PL lifetime determined from stretched exponential fit for $FASn_xPb_{1-x}I_3$ with x = 0.25 and x = 1, excited at 14 and 1400 nJ cm^{-2}. Phase transitions are shown by black dashed lines. (c) Relative PL intensity for x = 0.25 and x = 1 when excited at 400 nm with a power of 1 W cm^{-2} pulsed at 80 MHz. PLQE for x = 1 is fixed relative to x = 0.25 at 295 K from measurements in Figure 5.7a. The PLQE is normalized by setting the intensity of the 25% Sn composition at T = 5 K to a PLQE of 1 and scaling all other data by the same factor. Grey and blue dashed lines are fits to the equations shown in the legend.

Higher radiative efficiencies at lower temperature may also result from an increase in the radiative bimolecular recombination rate constant k_2 with decreasing temperature. Such trends would be expected, as such band-to-band recombination has recently been shown to be the inverse process to absorption (by the principle of detailed balance) and therefore the enhancement at low temperature is caused by the sharpening of the photon and charge-carrier distribution functions.[33] The PL lifetimes do indeed reduce (k_2 higher) at low temperature (<60 K), where such radiative band-to-band recombination begins to play a larger role, evidenced by the higher PLQE. The difference in high and low excitation lifetimes in this temperature region also supports the larger role of k_2. However, if it were the dominant process across all temperatures at the excitation fluences used, the PL lifetimes should decrease with decreasing temperature, which is not observed. I therefore conclude, in agreement with the arguments above, that a reduction in non-radiative trap-mediated recombination rate is the primary cause of the increased lifetime and PLQE as temperature is decreased, and dominates the charge-carrier recombination processes at room temperature here.

To understand the temperature dependence of these trap-mediated charge-carrier recombination processes I consider several mechanisms within the theory of Shockley-Read-Hall recombination, as discussed in Section 2.5.3. Of these mechanisms, the strongly temperature-activated non-radiative recombination channels in the 25% perovskite are most likely the result of multi-phonon assisted SRH recombination. The relative PLQE can be fitted by Equation 2.11 to yield a characteristic activation energy of 40 meV for 25% Sn and 0.5 meV for 100% Sn. (The fitting parameter A is 1.3×10^4 for 25% Sn and 44 for 100% Sn). This can be interpreted as an upper limit to the activation energy for multi-phonon assisted recombination, since the temperature dependence of k_2 will also contribute to the 'activation energy' from the fitting. In

addition for the 100% Sn composition, p-doping will change with temperature as holes return to acceptor ions, which will introduce further contributions to the temperature dependence of both the radiative and non-radiative recombination rates. This interpretation gives a more physically grounded explanation of the temperature dependence of PLQE data for metal halide perovskites than the exciton binding energy interpretation discussed in Section 2.5.5, and also explains why the lifetime increases concomitantly with the PLQE.

A better fit, shown in Figure 5.11c, is obtained at low temperature for the 25% Sn PLQE data by including a T^2 term, such that $R = Aexp(-E_a/kT) + CT^2$ in Equation 2.10. The activation energy is fixed and A and C are fitted to give $A = 1.1x10^4$, $C = 9.3x10^{-4}$ K^{-2} and $E_a = 40$ meV as before. This may be due either to the temperature dependence of radiative recombination[33] or to the presence of a distribution of traps, which is only distinguishable at low temperature, as proposed recently for $FAPbI_3$.[144] However, such fits also have an uncertainty because they do not take photon reabsorption into account.[153]

As Figure 5.11b-c illustrate, the 100% tin composition exhibits significantly less temperature-activated behaviour, with PL lifetimes and relative PLQE only rising slightly with decreasing temperature. These data therefore suggest that, in $FASnI_3$, either trap-assisted Auger recombination or multi-phonon SRH recombination with a very small activation energy is the predominant mechanism in operation. These are both non-radiative processes, accounting for the low relative PLQE. However, as discussed above, the SRH model predicts a trap-mediated mono-exponential decay ($\beta = 1$) of charge-carrier densities in the presence of high doping levels, whereas trap-assisted Auger recombination does not,[145] making an SRH mechanism the most likely non-radiative recombination process to be in action for $FASnI_3$ here.

The 100% Sn composition also shows much less fluence dependent behaviour than the 25% Sn composition, with little difference between the PL lifetimes at high and low excitation power (Figure 5.11b). This is unsurprising given the large value of k_1 indicated by the rapid monoexponential decay, meaning a very high fluence (much higher than the maximum of 1400 nJ cm^{-2} used here) is needed to reach the carrier densities required to observe significant bimolecular recombination. For all compositions, the measurements show no direct evidence of trap saturation, which can result in an increase in lifetime at higher fluence, and therefore it is not necessary to consider the effects of carrier trapping discussed in Section 2.5.4.

To summarise these findings regarding the charge-carrier recombination channels in $FAPb_{1-x}Sn_xI_3$, I have shown that non-radiative pathways dominate for all compositions at room temperature at a fluence of 14 nJ cm^{-2}. The lead-rich composition with 25% Sn content has a temperature-activated non-radiative recombination pathway indicative of multi-phonon recombination. In contrast, charge-carrier recombination channels in $FASnI_3$ (100% Sn) are hardly affected by temperature, but the small increase in lifetime suggests multi-phonon recombination with a small activation energy. I find that at room temperature the PL decay dynamics fall into a lead-rich regime with longer lifetimes and stretched exponential decays, and a tin-rich regime with shorter lifetimes and mono-exponential decays. These observations are in agreement with a previous study showing that decomposition pathways, and hence defect formation, differ substantially in the tin- and lead-rich composition regimes.[119] I have discussed that Shockley-Read-Hall statistics predict fluence-dependent charge-carrier recombination for intrinsic semiconductors, but fluence-independent mono-exponential behaviour for heavily doped semiconductors, which underpins the difference in recombination dynamics observed for these two regimes. Doping also enhances radiative recombination which,

even if it is not the dominant mechanism in recombination dynamics, still increases the PLQE by an order of magnitude for $FASnI_3$ in comparison to $FAPbI_3$.

5.3 Conclusion

In conclusion, I have demonstrated the important influence of composition and temperature on the band gap and recombination mechanisms of $FAPb_{1-x}Sn_xI_3$, two essential properties in the design of efficient solar cells. I have reported structural phase transition temperatures for mixed compositions for the first time and a band gap bowing parameter of 0.73 and 0.84 eV for the room temperature and low temperature phases respectively, showing that crystal structure influences the magnitude of bowing. I have used a combination of temperature dependent transient PL and PLQE measurements to distinguish different recombination mechanisms, showing that there is still considerable non-radiative recombination at room temperature in both 25 and 100% Sn compositions. This strongly suggests that efforts to increase lifetimes of tin-rich perovskites should focus not only on controlling doping densities but also on reducing non-radiative recombination via trap states. For this range of compositions of $FAPb_{1-x}Sn_xI_3$ I find the perovskite with around 40% Sn to be the most promising low band gap material for use in tandem solar cells. $FAPb_{0.6}Sn_{0.4}I_3$ combines the long charge-carrier lifetime of the lead-rich materials with a PLQE approaching that of $FAPbI_3$ and a relatively small Stokes shift and PL linewidth compared to the other alloys. Its band gap of around 1.3 eV is suitable for tandem devices and fairly close to the minimum achievable for $FAPb_{1-x}Sn_xI_3$ alloys. However, this work highlights that the optoelectronic properties of these materials are still highly dominated by extrinsic effects. Therefore, more favourable properties may still be obtained across the series with additional materials engineering, such as the optimization of treatments with

compounds such as SnF_2 to increase the charge-carrier lifetime of the tin-rich compositions or addition of other cations and halides to tune the structural properties, which will influence both the band gap bowing and the charge-carrier lifetimes. This study highlights the link between such structural and optoelectronic properties, thus paving a way towards more guided materials design.

6 $MAPbI_3$: QUANTUM CONFINEMENT AND GROWTH MODE

The results presented in this chapter have been published in: Parrott, E.S.; Patel, J. B.; Haghighirad, A.-A.; Snaith, H. J.; Johnston, M. B.; Herz, L. M., Growth Modes and Quantum Confinement in Ultrathin Vapour-Deposited $MAPbI_3$ Films. *Nanoscale*. 2019, 11, 14276.

6.1 Introduction

One advantage of metal halide perovskite materials is that they can be fabricated by a variety of methods[41] including spin coating, a method which enables quick and easy fabrication of small scale samples in the laboratory. Whilst the widespread use of this technique has facilitated rapid advances in the technology, the development of techniques which can reliably reproduce high-quality films at large scale has lagged behind. This must be addressed if perovskites are to be scaled up for commercial use and reach their full potential in large scale renewable energy generation.[41]

Vapour deposition by thermal evaporation, is a technique suitable for large scale device fabrication[186] and produces uniform, smooth thin films[30] with precise control over the film thickness.[153] These qualities have proved successful in fabricating a range of metal halide perovskite materials for solar cells,[30,186–188] flexible devices,[189] and

amplified spontaneous emission.[190] It also enables uniform coating of rough surfaces such as pyramid-textured silicon for use in efficient perovskite-silicon tandem solar cells.[191] Fabricating metal halide perovskites by this method involves evaporation of solid precursors of type AX and BX_2 (such as CH_3NH_3I and PbI_2) by two possible methods; a sequential deposition method and a co-evaporation method. For the sequential deposition method,[192] the precursors are evaporated in separate layers, which diffuse into each other to form the perovskite. However this method has yielded a maximum PV device PCE of only 16% to date,[193] and requires annealing, which can introduce thermal strain.[194,195] A more successful method is the co-evaporation technique in which the precursors are simultaneously evaporated from two sources to form the perovskite directly on the substrate.[158] This method ensures the composition is the same throughout the film with no additional annealing, and has been used to make devices with a PCE of 20.3%.[196]

One factor responsible for the leap in both the efficiency and stability of solution processed devices was the use of crystal growth engineering to control the film morphology.[197,198] This has led to huge increases in grain sizes reaching the millimetre scale,[199] a development which has been linked to improved solar cell performance[34,63,200] and enhanced stability.[201,202] In contrast, thermally evaporated films still show very limited grain size on the order of 100 nm.[30,153,158,189,203] Although relatively high efficiency devices can still be fabricated even at this suboptimal grain size, their stability still requires optimization.[196] Resolving the problem of small grain sizes by understanding the early stages of film growth is therefore paramount to improvement.

An additional advantage of understanding the growth of $MAPbI_3$ thin films is its application to growing nanostructures for use in light emitting diodes (LEDs) and other

electronic devices. Metal halide perovskites have been used to make LEDs in many different architectures.[204–209] Nanocrystals and 2D perovskites are particularly attractive for this purpose since the charge-carriers exhibit quantum confinement, which boosts the radiative recombination rate, narrows the emission linewidth, and allows for wavelength tunability by controlling the size of the crystals or the thickness of quasi-2D layers.[204,210] Nanocrystals can exhibit PL quantum efficiency of over 90% in solution, yet in devices it is challenging to produce an external quantum efficiency (EQE) of over 6% due to ligands preventing good charge transport.[204] 2D perovskites have been employed in a multi-quantum-well type structure,[205] but since the thickness and arrangement of the layers cannot be fully controlled[209] this also hinders charge transport.[207] Recent breakthroughs have seen a handful of devices achieving EQE as high as 20%[206–208] but there is still some room for improvement. In traditional inorganic semiconductors confinement has been achieved by growing quantum wells by controlled deposition methods with EQE of over 80%.[211] If perovskite layers could be grown by thermal evaporation at dimensions thin enough for quantum confinement, this could combine the benefits of confinement and good charge transport. Understanding the formation of metal halide perovskite thin films could therefore provide alternative methods for fabricating efficient LEDs.

Characterisation of the early stages of thin film development can be challenging, since it requires analysis of a very small amount of material. Metal halide perovskites are soft materials and prone to degradation, which makes the use of imaging techniques challenging. For example, transmission electron microscopy (TEM) can be used to directly image the morphology of a very thin film, but requires the film to be exposed to a high energy electron beam, under which $MAPbI_3$ is liable to degrade.[212] Even atomic force microscopy (AFM) can cause changes to the film due to the interaction of the tip

and the surface.[200] Other characterisation methods can be undertaken *in situ*, using bespoke deposition chambers to take measurements in real time, or *ex situ*, by growing films of increasing thickness under the same conditions. *In situ* X-ray diffraction (XRD) measurements have been carried out during co-evaporation of several metal halide perovskites,[213,214] however the time resolution is limited by the amplitude of the signal, and so these measurements were not able to capture the early stages of growth where the signal is low. *Ex situ* XRD[215] and XPS[215–217] measurements on $MAPbI_3$ show the formation of additional species at the perovskite-substrate interface such as PbI_2[215,217] and decomposition products of MAI,[216] which prevents the growth of pure $MAPbI_3$ thin films. *In situ* measurements have also been carried out for solution processed films as the precursor film converts to perovskite.[218]

In this chapter, I report the growth of thin films of $MAPbI_3$ with optical thickness as small as 2 nm with no detectable presence of PbI_2 in the XRD spectrum. By comparing optical absorption and XRD measurements I find evidence for an island growth mode, with material in the thinnest films coalescing into crystallites with a height of around 7-8 nm, small enough to display significant PL blue-shift due to quantum confinement, which offers a simple alternative route to fabricating nanocrystals. Substrate coverage is achieved at an average thickness of 14 nm which is promising for growing quantum well structures. Even without confinement, it has been shown that reducing the thickness of the perovskite in LEDs increases the efficiency.[219] By further optimization of the deposition process and material-substrate interaction to encourage layer-by-layer deposition, there is the potential for even thinner films to be formed. Achieving layer-by-layer deposition could also be beneficial towards increasing the grain size in thicker films which could help improve the efficiency and stability of solar cells, since the island growth mode may be responsible for the limited grain size.

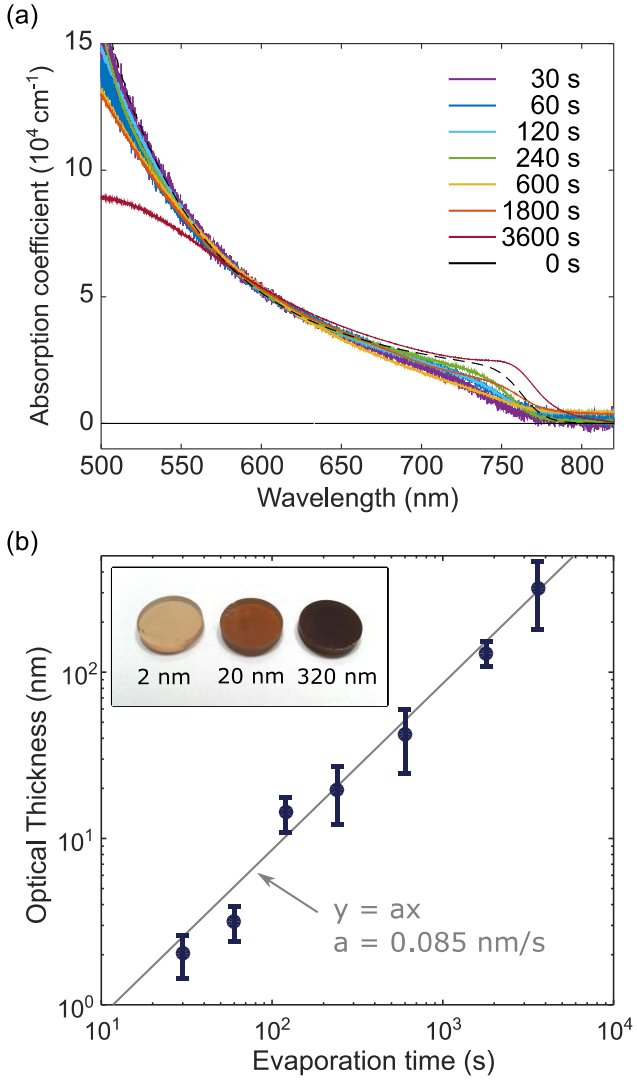

Figure 6.1. (a) Absorption coefficient for each $MAPbI_3$ thin film sample, determined by matching the measured optical depth in the range 550-700 nm to the known absorption coefficient determined by Crothers et al.[153] and shown by a black dashed line. The evaporation time of $MAPbI_3$ onto the quartz substrate is given in the legend. (b) Thickness calculated by matching the absorbance of each sample to the known absorption coefficient as shown in (a), referred to here as the optical thickness. The grey line is the fit (y = ax) to the data, giving a deposition rate of 0.085 nm s^{-1}. The inset is a photograph of the 2, 20 and 320 nm $MAPbI_3$ films on 2-mm-thick quartz substrates, showing that the difference in absorption can be seen by eye.

6.2 Results and Discussion

To investigate different stages of growth, 7 batches of $MAPbI_3$ films were evaporated at different thicknesses by changing the length of time for which the substrate was exposed to MAI and PbI_2 vapour in the evaporator. A visible colour difference was observable from almost transparent brown to opaque black as the thickness was increased (see inset to Figure 6.1). I determined the thickness (*D*) by matching the optical depth (*a*) for each sample to a known absorption coefficient (α) in the 550-700 nm range allowing for a small amount of background scatter (*b*), as described in Section 3.3.3. The absorption coefficient calculated from the fitting parameters for each sample (α = (a-b)/D) is shown in Figure 6.1a, showing there is an acceptable match. From here on I will refer to the average physical thickness of a $MAPbI_3$ film determined by this method as the 'optical thickness'. The determined optical thicknesses are shown in Figure 6.1b for each evaporation time. The fit shows that the deposition occurred approximately linearly at a rate of 0.085 nm s^{-1}.

6.2.1 Strain

I characterised the films using X-ray diffraction, with the angles referenced to the quartz reflection (shown in Figure 6.2 and marked with an asterisk in Figure 6.3a) to account for any small offset in the angle of the sample. All samples showed peaks at the expected angles for (100) and (200) crystallographic planes, with the thickest samples showing several additional peaks of lower intensity originating from other crystallographic orientations of the perovskite lattice. These orientations may be present in all samples, but the corresponding peaks would be indistinguishable in the thinner films due to the lower signal to noise ratio (Figure 6.2). The (100) and (200) peaks of the thinner films showed slight angular shifts in comparison to the thickest film,

corresponding to a global expansion of the lattice parameter. In the XRD geometry for this experiment the lattice planes contributing to the peaks are in the plane of the substrate, so the measured expansion corresponds to tensile strain perpendicular to the substrate. The cause could either be volume expansion or, more likely, compressive biaxial strain in the plane of the substrate which induces an out-of-plane expansion[195] (since the Poisson ratio has been theoretically predicted to be 0.33).[220] Since the pseudo-cubic lattice parameter of 6.275 Å measured for the thickest sample falls within the range of previously measured values for unstrained $MAPbI_3$,[221–223] the strain normal to the (100) direction is calculated relative to this value using the equation

$$\epsilon = \frac{d_s - d_0}{d_0}$$

Equation 6.1

where d_s is the lattice parameter of the sample and d_0 = 6.275 Å is the unstrained lattice parameter. The results are shown in Table 6.1 and plotted in Figure 6.3b. As the film grows, strain increases up to a maximum, then decreases and becomes small above 50 nm.

Optical thickness (nm)	Angle of (100) (deg.)	d-spacing of (100) (Å)	d-spacing of (200) (Å)	Mean d-spacing (Å)	Error: d(100) - d(200)	Strain (%)
2	14.0213	6.2956	6.2852	6.2905	0.0104	0.247
3	14.0011	6.3202	6.3157	6.318	0.0044	0.685
14	14.0417	6.302	6.3107	6.3065	0.0087	0.502
20	14.0534	6.2968	6.3023	6.2995	0.0055	0.39
42	14.1017	6.2789	6.288	6.2835	0.0091	0.135
130	14.095	6.278	6.2786	6.2784	0.0006	0.054
320	14.1018	6.2752	6.2748	6.275	0.0004	0

Table 6.1. Calculated pseudo-cubic lattice parameters for the two perovskite peaks (100) and (200) in the XRD spectra for each of the $MAPbI_3$ thin-film samples, and strain calculated from the mean lattice parameter.

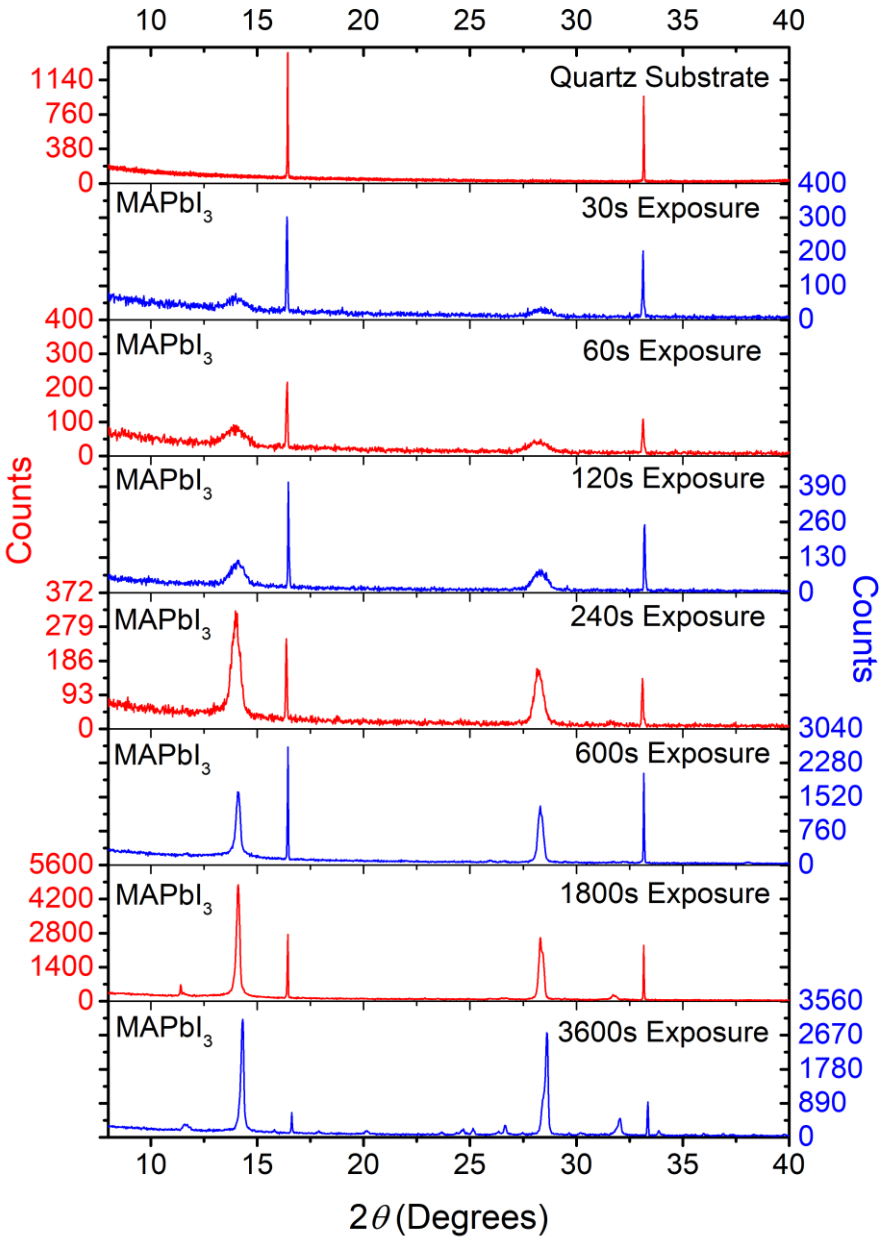

Figure 6.2. X-ray diffraction spectra of $MAPbI_3$ thin films obtained at a scan speed of 0.4 °/s for 30 minutes using a Cu-Kα radiation source at λ = 1.54 Å operating at 40 kV and 40 mA. Vapour exposure times from 300-3600 s in the evaporator correspond to perovskite optical thicknesses of 2-320 nm.

There are three main causes of strain in polycrystalline thin films: (i) misfit strain, which occurs when a film grows epitaxially on a substrate with a mismatch between the substrate and film lattice parameters; (ii) thermal strain, which occurs due to a temperature change when there is a difference between the thermal expansion coefficients of the substrate and film; and (iii) intrinsic strain, which is affected by the growth conditions and includes factors such as the energy minimisation of crystal surfaces and the effect of impurities.[224] Coherent strain is ruled out since the mismatch between the perovskite and the relevant lattice parameter of the z-cut quartz substrate (4.9 Å) is too large for epitaxial growth. Thermal strain occurs in annealed perovskite films due to the large thermal expansion coefficient and results in the out-of-plane lattice parameter shrinking,[194,195] which is a change in the opposite direction to the measurements. Thermal strain is unlikely to occur here since the substrate was held at room temperature throughout the deposition, storage and measurements. The strain we observe is therefore most likely to be intrinsic.

Intrinsic strain has been observed in metal halide perovskites made by solution methods due to intermediate complexes in the crystallisation process.[194] This cannot be the mechanism here since no solvents are used in thermal evaporation. Changes in intrinsic strain as growth progresses are commonly seen in inorganic crystalline thin films fabricated by vapour deposition methods.[224,225] For island growth, surface energy minimisation of the exposed crystal faces and material-substrate interface generates strain, usually compressive strain in the plane of the substrate.[226] As more material is deposited and the edges of the islands approach each other, the gap decreases until cohesion causes the material to elastically stretch and coalesce.[227] For a fully covered substrate, the surface stresses are no longer as important since there is less surface area, and the lattice parameter tends to its bulk value. This could be the mechanism driving

the initial rise in strain followed by relaxation, which we observe with increasing film thickness. Alternatively the strain may be induced by impurities originating from the evaporation source or from degradation products. Others have seen either an excess of PbI_2 at the substrate interface due to the superior wetability of PbI_2 in comparison to MAI,[215] or a presence of MAI degradation products due to a catalytic interaction with the substrate.[216] There is no evidence of PbI_2 in the XRD spectra and the quartz substrates used are unlikely to cause decomposition of MAI. Shifts in the Raman spectra of $MAPbI_3$ nanoplatelets grown by chemical vapour deposition have been observed at similar thicknesses, which the authors attributed to lattice distortion at the interface, a theory which may be supported by the increased strain observed.[228]

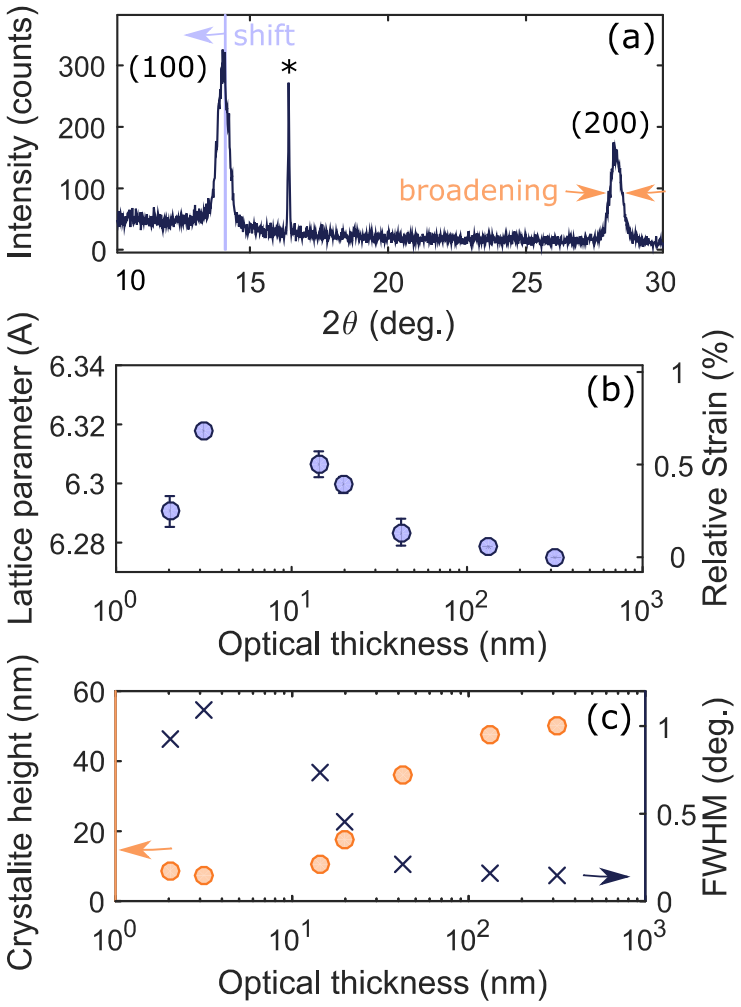

Figure 6.3. (a) Example of XRD data for 42 nm sample, showing the peak shift and broadening. (b) The lattice parameter is the mean of the lattice parameter for the (100) and (200) peaks. The error bar indicates the difference between the two values. The strain is calculated relative to that of the thickest sample. (c) The crystallite height (orange circles) is calculated from the full width at half maximum of the peak (blue crosses) using the Scherrer equation (Equation 3.17).

6.2.2 Growth mode

Next, I determine the height of the crystallites in the perovskite film from the XRD spectra by measuring the line broadening that occurs due to the finite number of lattice planes limiting the X-ray coherence length. More broadening therefore implies that the crystallite is smaller in the direction perpendicular to the substrate. A colleague determined the full width at half maximum (FWHM) of the (100) perovskite peak by fitting a pseudo-Voigt function, and I corrected this value for instrument broadening by comparison to the FWHM of the XRD peaks of a silicon reference (see Section 3.5.1). I then found the crystallite height from the corrected FWHM using the Scherrer equation (Equation 3.17), found in Table 6.2[155] These values are also plotted in Figure 6.3c.

Optical thickness (nm)	FWHM of (100) (deg.)	Corrected FWHM of (100) (deg.)	**Crystallite size (nm)**
2	0.9266	0.9245	**8.7**
3	1.0889	1.0871	**7.4**
14	0.7429	0.7403	**10.9**
20	0.4597	0.4555	**17.7**
42	0.2216	0.2127	**37.9**
130	0.1695	0.1578	**51.1**
320	0.1602	0.1477	**54.6**

Table 6.2. Full width at half maximum measured for the (100) peak for each of the samples, full width at half maximum for the same peak corrected for instrument broadening using Equation 3.16, and the crystallite size determined from Equation 3.17 using $\lambda = 0.15406$ nm, $\kappa = 0.8859$, β from the corrected FWHM in this table, and θ from Table 6.1. The FWHM is only accurate to two decimal places, but all decimal places were used in calculations before rounding the final result.

This analysis neglects any contribution to broadening of the XRD peaks from microstrain, which is a measure of the distribution of lattice parameters present in the material due to inhomogeneity. The Scherrer equation is valid for thinner films where size broadening dominates over microstrain, and is therefore often used to determine the size of nanocrystals.[210,229] However, the values for crystallite size determined by this method become inaccurate as the film thickness increases, and should be seen instead as a lower limit on the crystallite size. To achieve a more accurate value of the crystallite height, the contributions from microstrain and size broadening can be separated by determining the FWHM of multiple XRD peaks and employing the Williamson-Hall plot method as described in Section 3.5.2.[230] I have undertaken this analysis for the thickest film (optical thickness of 320 nm) for which enough peaks are distinguishable in the XRD spectrum to accurately separate the two contributions, with the resulting plot shown in Figure 6.4. The analysis yields a crystallite height of 75 nm and a microstrain of 0.16%, leading to the conclusion that the microstrain is small, and that its inclusion provides only a minor correction to the values of crystallite height obtained from the Scherrer equation alone. The value of microstrain determined here is lower than the value of 0.65% which has been previously derived by the same method for $MAPbI_3$ fabricated by solution processing.[231] If these values are intrinsic to the growth conditions, lower microstrain could be an additional benefit of fabricating $MAPbI_3$ by co-evaporation, since microstrain has been linked to poorer device performance[232] and higher risk of mechanical failure due to delamination.[233]

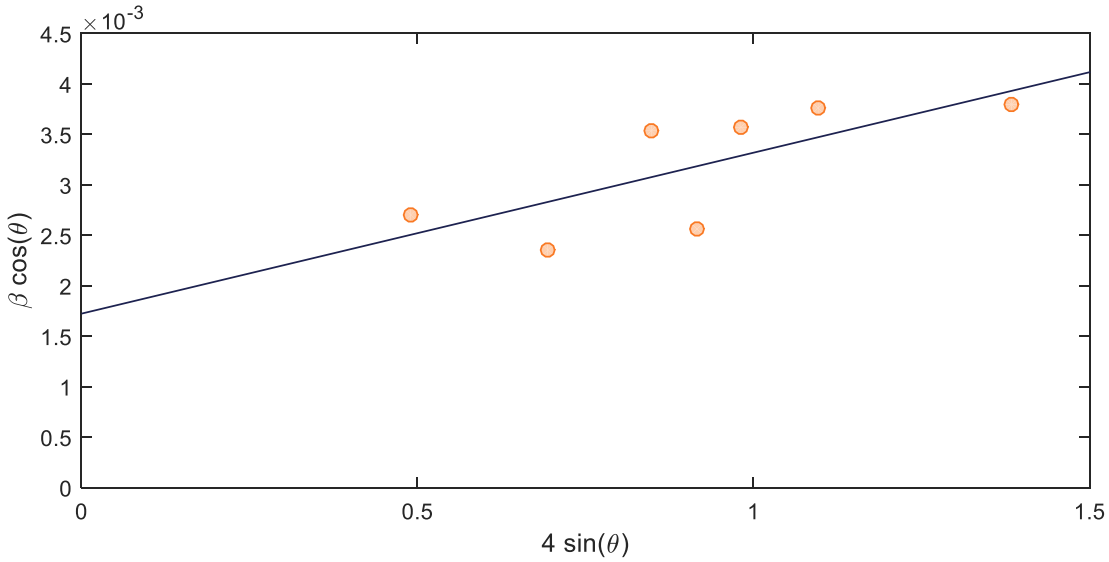

Figure 6.4. Williamson-Hall plot for the $MAPbI_3$ sample with 320 nm optical thickness. The full width at half maximum (β) and the Bragg angle (θ) are determined from Voigt functions to seven strongest peaks in the XRD spectrum, and each orange point corresponds to one peak. The blue line is a fit of Equation 3.19 to the data.

By plotting the ratio (r) of the crystallite height to the optical thickness, as shown in Figure 6.5, three stages can be deduced in the film growth of $MAPbI_3$ on quartz by thermal evaporation. In the first stage when the optical thickness is below 10 nm, the material is formed in single crystallite islands, around 7 nm in height. The ratio *r* remains below 1, since the height of the islands is larger than the average film thickness (optical thickness). Increasing the evaporation time increases the proportion of the film covered by islands, and therefore the optical thickness, but there is no change in the height of the islands at this initial stage of the growth process. In the second stage, full coverage is reached and the crystallites begin to grow upwards with the ratio *r* equal to one. In the third stage, the crystallite height plateaus but the film thickness continues to increase. Since the crystallite height is a measure of the number of coherent lattice planes, a crystallite height smaller than the optical thickness means there are multiple crystal orientations stacked on top of each other within the thin film. The ratio *r* is therefore greater than one, though the values here are slightly exaggerated by neglecting the effect of microstrain in the crystallite height determination, as discussed above. The three stages of growth outlined above also correspond to the build-up, release, and plateau of strain respectively, consistent with the suggestion of intrinsic strain being caused by island growth.

Thin films display three primary growth modes – island (Volmer-Weber), layer-by-layer (Frank-van der Merwe) and layer-plus-island (Stranski-Krastanov). Stranski-Krastanov growth requires that the substrate has a similar lattice parameter to the deposition material, allowing the initial formation of epitaxial layers up to a critical thickness followed by island formation to release strain caused by lattice misfit between the substrate and deposition material.[234] Island and layer-by-layer growth modes are not limited to materials grown on lattice matched substrates, and can occur in non-epitaxial

film growth where the initial nucleation largely depends on the minimization of surface energy. Volmer-Weber type growth typically occurs when the cohesion energy (between the material and itself) is larger than the adhesion energy (between substrate and material).[235] It is therefore energetically favourable for the material to cluster, rather than forming a uniform layer on the substrate. Frank-van der Merwe type growth occurs under the opposite condition, when the adhesion energy is larger than the cohesion energy.[235] The Volmer-Weber type island growth mode observed here could explain why the grain size of vapour deposited perovskites is small (around 100 nm) compared to solution deposited thin films, since the lateral grain size is determined by the initial nucleation of the crystals. A detailed study investigating different growth parameters such as temperature and substrate may therefore be beneficial. For example, increasing the substrate temperature could increase the grain size, since the ad-atom mobility is increased, usually resulting in fewer islands per area,[235] though excessive heating could introduce thermal strain. Alternatively, using a different substrate or a substrate coating with increased adhesion energy could change the growth mode to a layer-by-layer deposition.[235] Epitaxial growth on a substrate with a matched lattice parameter could also be an interesting avenue to explore.

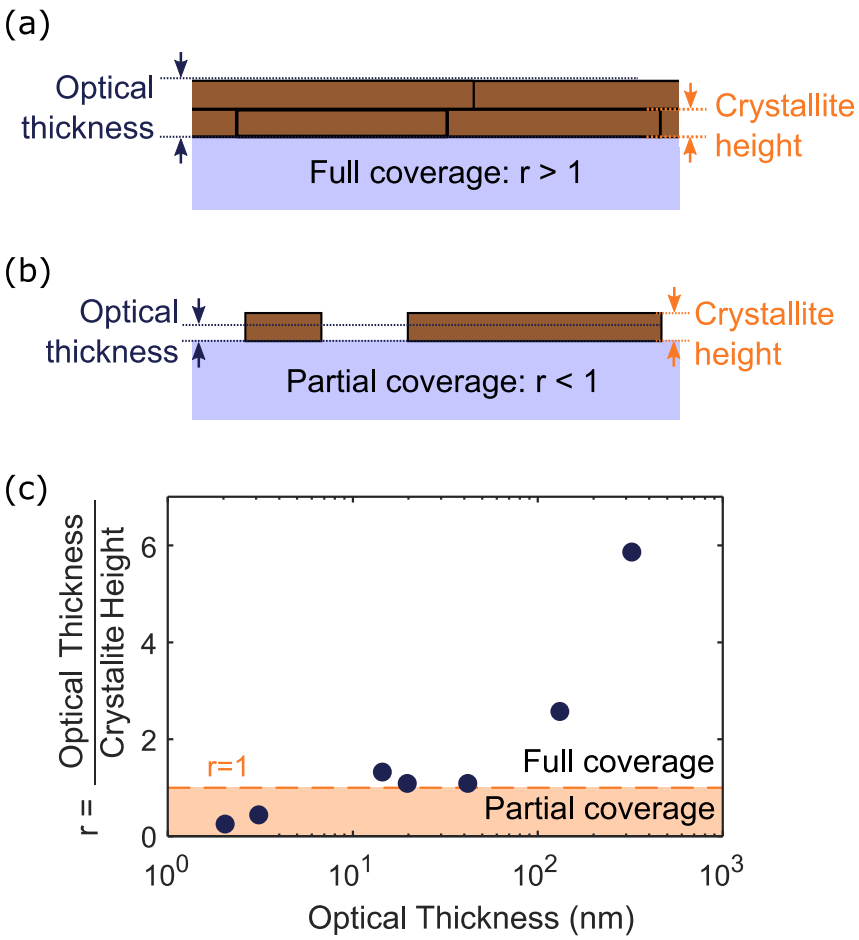

Figure 6.5 (a) Diagram showing the relevant thicknesses when the ratio r is greater than 1. (b) Diagram showing the relevant thicknesses when the ratio r is greater than 1. (c) Ratio of the thickness determined from the absorption coefficient (optical thickness), and the grain height calculated from XRD FWHM.

6.2.3 Quantum confinement

Finally, I investigate the effect of thickness on the photoluminescence (PL) of the perovskite film. The PL spectra for these samples show a strong blue-shift in the PL emission with decreasing thickness, shown in Figure 6.6a. First, the effect of self-absorption must be accounted for. Since the absorption edge overlaps the PL emission, the higher energy photons will be reabsorbed in the thicker films, which therefore red shifts the PL intensity maximum.[153] Equation 3.7 outlined in Section 3.1.3 is used to correct the PL spectra for the five samples where the substrate was fully covered, accounting for reflection from the interfaces and the absorbance of the film. The effect of reabsorption is assumed to be negligible for the thinnest two samples, since the island structure and the fact that these samples are less than 10 nm in thickness should enable light to escape easily and not be reabsorbed. From the corrected spectra, I found the energy of maximum PL intensity for each thickness, averaged over multiple measurements for samples of the same thickness. Following the same procedure without the self-absorption correction for comparison shows that self-absorption is substantial only for the thickest of the films (130 and 320 nm), as shown in Figure 6.6b.

Even when self-absorption has been corrected for, the PL peak energy still shows considerable dependence on film thickness. Similar dependence has been observed in perovskites and attributed to quantum confinement, as discussed in Section 2.3.3. The quantum confinement effect in $MAPbI_3$ has already been shown to be strong in comparison to the equivalent Br and Cl perovskites due to its smaller effective exciton mass μ,[109] and a value of 1.69 eV at 7 nm diameter has been reported,[109] similar to this result, so it seems likely that this is the reason for the shifts observed.

Figure 6.6 shows the dependence of the peak PL energy on film height, fitted with an equation for a quantum confined electronic system (Equation 2.2). I take the

confinement to be in one dimension only, perpendicular to the film, which assumes that the diameter of the islands is greater than their height. The relevant dimension for confinement, *d*, is therefore the crystallite height for the films consisting of islands, and the optical thickness for the other films, which are distinguished by different markers in Figure 6.6b.

The fit of Equation 2.2 to the data gives a band gap energy of 1.605 eV and a value of *B* of 5 eV nm^2. Since $MAPbI_3$ has a small exciton binding energy, the carriers should be free at room temperature. Although dielectric confinement can increase the binding energy when the dimensions are small, this should not be significant for the films which all have a confinement dimension greater than 7 nm. In a regime where the carriers are free, $B = \hbar^2\pi^2/2\mu$ giving an effective mass of $\mu = 0.075m_e$. Theoretical results have predicted a value of $B = 1$ eV nm^2 for $MAPbI_3$,[236] and PL measurements for $MAPbBr_3$[229] and $CsPbBr_3$[111] have yielded $B = 12$ eV nm^2 and $B = 2.6$ eV nm^2 respectively. These values are not directly comparable since they are for nanocrystals so charge-carriers are confined in three dimensions and *d* is the radius of the nanocrystal sphere, however they confirm that this result falls close to the expected order of magnitude.

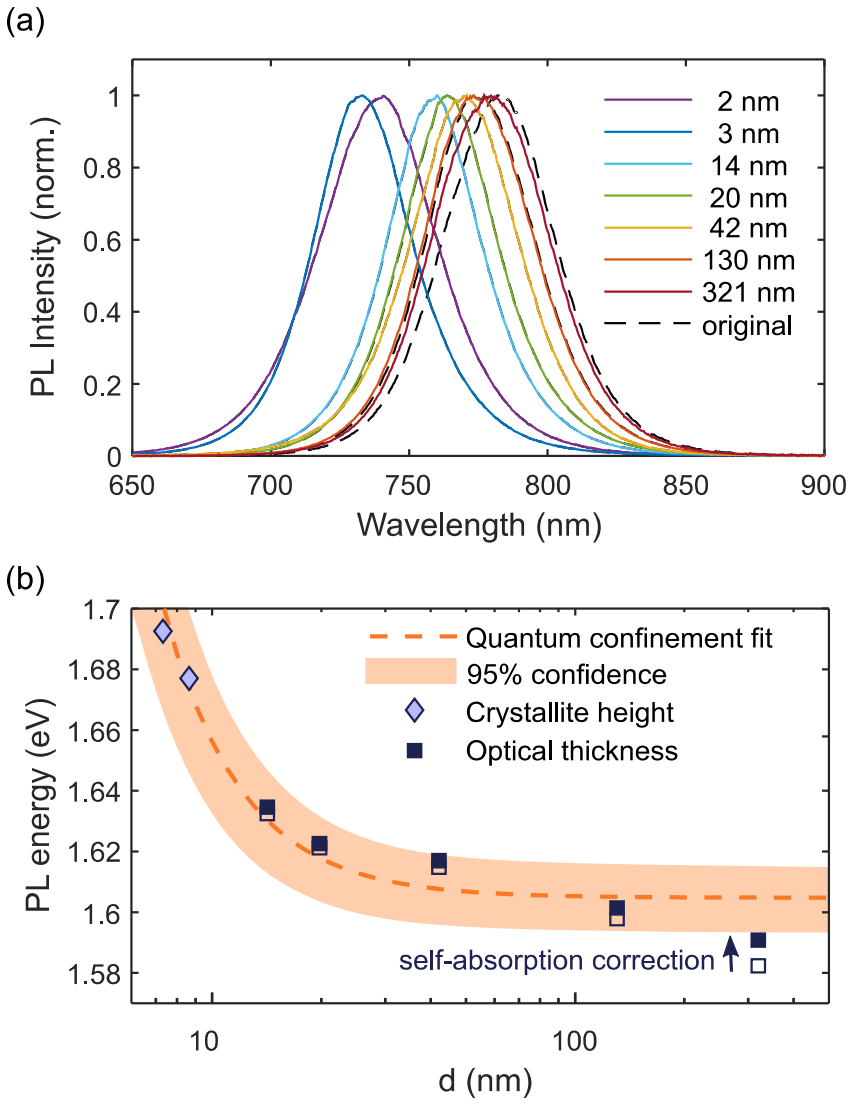

Figure 6.6. (a) Averaged PL spectra prior to self-absorption correction (black dashed lines) and after correction (solid coloured lines) for each sample, normalized to 1. (b) Peak PL energy with self-absorption correction (filled symbols) and without self-absorption correction (empty symbols) as a function of the relevant film height d, which is crystallite height for partially covered samples (diamonds) and optical thickness for fully covered samples (squares). The data are fitted with an equation for quantum confinement $E = E_g + B/d^2$. The dashed line is the fit, and the shaded area is the 95% confidence limit.

There are two additional considerations which could affect the band gap energy – strain and chemical composition. DFT calculations have predicted a linear change in band gap with strain.[64,237] A volume expansion corresponding to the change in lattice parameter between the least strained and most strained films is calculated to produce a band gap shift of 0.03 eV.[64] This is much less than the change of over 0.1 eV observed, and therefore the effect of strain cannot fully explain the blue shift observed. Photo-induced degradation can also cause a blue shift in PL wavelength, indicating a change in the lattice eventually leading to a conversion to PbI_2.[238] However, the XRD data show the films still had the perovskite structure at the time of measurement with no presence of PbI_2.

6.3 Conclusion

In conclusion, I have monitored the incipient steps in the formation of $MAPbI_3$ thin films fabricated by dual-source co-evaporation from an optical thickness of 2 nm to 320 nm. I find that the material initially forms crystallite islands of around 8 nm in height, which coalesce and build up strain. Once the substrate is completely covered, the crystallites grow in height uniformly and strain is released. I have demonstrated that photoluminescence from the thinnest $MAPbI_3$ films is dominated by quantum confinement, which opens an alternative pathway towards the fabrication of nanoscale structures for efficient LEDs. With the growth procedure used in this work, light-emitting $MAPbI_3$ films could be employed in an architecture incorporating 8 nm thick islands or a uniform layer of 14 nm or more. I note however that uniform growth of even thinner films should be easily within reach, e.g. through an optimization of perovskite-substrate interactions and growth conditions such as substrate temperature. Attempting epitaxial growth on a lattice matched substrate by vapour deposition would also provide a promising route towards ultra-thin layers suitable for multiple quantum wells or other heterostructures. Finally, I suggest that the Volmer-Weber type island growth mode observed in the early stages of the film growth may well be the cause of the small grain size that is typically encountered in co-evaporated perovskite films. Hence the development of a method suitable for producing layer-by-layer growth may hold the key towards increasing crystallite grain size, thus improving the efficiency and stability of solar cells fabricated though vapour deposition.

7 CONCLUSION

7.1 Summary

The investigations detailed in this thesis serve to clarify and expand the knowledge of the optoelectronic properties of organic-metal-triiodide perovskites by photoluminescence spectroscopy. The results show that adjusting the composition, the structural phase and the dimensions of the material, enables control over the band gap and charge-carrier dynamics which can be exploited to optimize their photovoltaic performance.

In Chapter 4, temperature dependent photoluminescence spectra and time-resolved PL measurements for $MASnI_3$ show a marked increase in carrier lifetime and a substantial reduction in PL linewidth below ~110 K at the tetragonal to orthorhombic phase transition. In addition, I observe an above-gap emission feature that may arise from higher-lying inter-band transitions, suggesting a relatively long-lived population of charge-carriers in a higher energy state.

Chapter 5 contains key structural and electronic properties of the $FAPb_{1-x}Sn_xI_3$ perovskite as a function of tin:lead content and temperature across the alloy series, from photoluminescence and optical absorption measurements. Tin-rich compositions exhibit fast, mono-exponential recombination that is almost temperature independent. Lead-

rich compositions show slower, stretched-exponential charge-carrier recombination. The phase transition temperature and room temperature gradient (dE_g/dT) of the band gap depend linearly on composition, whereas the relationship between the low temperature gradient and composition is non-linear. The large band gap bowing parameter, a crucial element for the attainment of low band gaps in this system, depends on the structural phase, taking a value of 0.84 eV in the low-temperature phase and 0.73 eV at room temperature.

In Chapter 6, $MAPbI_3$ films with optical thicknesses from 2 – 320 nm are fabricated by co-evaporation and characterised using X-ray diffraction, optical absorption and photoluminescence (PL). The perovskite initially forms crystallite islands of around 8 nm in height. As more material is added, islands coalesce until full coverage of the substrate is reached at around 14 nm average thickness. Substantial shifts to the PL wavelength are achieved when the optical thickness is below 40 nm due to quantum confinement, offering an alternative method of fabricating nanoscale structures for LEDs and other devices.

7.2 Discussion and Outlook

7.2.1 Charge-carrier dynamics

The first aim of this thesis was to provide an understanding of the rapid charge-carrier recombination of tin halide perovskites. Previous work had suggested the presence of spontaneous hole doping as the reason for the short PL lifetime, in which case as the temperature of the material is lowered, the lifetime should increase and the PLQE decrease as holes in the valence band return to their acceptor ions. The results in Chapter 4 show that this increase in lifetime only occurs in the orthorhombic phase, where the PL linewidth indicates that a portion of defects have been deactivated. These defects are likely to be ionizable defects contributing to doping, suggesting that the phase transition is responsible for a realignment of the acceptor levels, resulting in a reduction in p-doping which lengthens the PL lifetime and also reduces charge-carrier scattering from acceptor ions. Despite the improvement, the lifetime is still less than 1 ns and the PL linewidth is over 100 meV at the lowest temperature, suggesting that there is still sizeable disorder in the material. This is likely due to other defects not responsible for doping, which are likely to cause non-radiative recombination, and shows that further research should focus more widely than the problem of reducing p-doping.

In Chapter 5, improvements have been made to the PL lifetime and linewidth of the tin-based perovskite by replacing the MA cation with FA, thus changing the structure, and by adding 20% molar excess of SnF_2 during fabrication. The PL lifetime is no longer limited by the recombination of electrons with doped holes, but by trap-mediated recombination, described by Shockley-Read-Hall statistics. The doping is still of importance however, as within SRH recombination, it is doping which causes the short-lived mono-exponential decays observed for tin-rich compositions. The longer-lived

stretched decays observed for the lead-rich compositions are still dominated by trap-mediated recombination, but have slower charge-carrier recombination due to the lack of doping and the shallow defect levels. The temperature activation shown in the PLQE and lifetime strongly suggest a phonon-assisted channel for non-radiative recombination.

It is important to note that this work is not commenting on the fundamental properties of these materials, but those related to their defects. These properties will depend heavily on the fabrication process and are therefore likely to improve as fabrication methods are advanced. However the relative ease with which high performance lead halide perovskite solar cells can be made has been linked to the high defect tolerance of the material, due to the shallow energy levels of the defects which are most likely to form. My work highlights that this is not the case for tin halide perovskites. Whilst there is still hope that improved fabrication methods can increase performance, success may also be achieved by modifying the properties to increase the defect tolerance.

Two strategies for increasing the defect tolerance of tin-based perovskites for low band gap absorber materials are presented in this thesis, providing openings for further work. Firstly, the discovery that defect tolerance is increased in the orthorhombic phase of $MASnI_3$ points to the possibility of improving the properties by engineering structural changes to the perovskite crystal. The desired structure could be achieved by using mixed-cation or mixed-halide perovskites. Secondly, the observation that the recombination dynamics of lead-tin perovskite alloys can be split into two regimes shows that mixed-metal compositions are likely to offer more efficient low band gap solar cells.

7.2.2 Band gap

The second aim was to investigate the tunability of the band gap. There have been various differing reports of band gap bowing in lead-tin halide perovskites. The large bowing parameter in $FAPb_{1-x}Sn_xI_3$ calculated from measurements of the absorption edge confirms that the lead-rich compositions, which have superior charge-carrier recombination dynamics, can have lower band gaps than an unmixed tin perovskite. The dependence of the bowing parameter on structural phase also shows that the band gap may be tuned further by engineering structural changes. The observation that the band gap bowing is parabolic at all temperatures is compatible with a mechanism arising from bond bending to accommodate the random placement of unevenly sized lead and tin ions, causing large changes to the band gap due to its sensitivity to octahedral tilt. DFT calculations using large super cells could elucidate the mechanism behind the band gap bowing further. The experimental measurements of the band gap for a range of compositions and temperatures will be useful to confirm any conclusions drawn by theoretical predictions. Calculations may also be of interest to investigate the nature of the temperature dependence of the band gap. Data across a range of compositions is therefore useful for confirming predictions and opening further lines of enquiry, such as why the gradient is steeper for $FASnI_3$ than $FAPbI_3$. The phase transition temperatures uncovered by discontinuities in the PL and absorption edge are also useful for characterisation of the material, since there are still many basic parameters that are unknown.

In Chapter 6, reduction of the perovskite film thickness is demonstrated to change the band gap by quantum confinement, this time to higher energies. Quantum confinement has been observed in $MAPbI_3$ nanocrystals but not in vapour deposited films, which provides a very simple route towards the fabrication of nanostructures. In particular, the

lack of ligands and the uniformity of films once the substrate is covered make the implementation in a device structure much easier. Hence these thin layers are promising for use in LEDs where the confinement has the additional advantage of increasing the radiative recombination rate. Further work is needed to implement this design. The island growth mode may be the cause of the persistent small grain sizes reported for evaporated metal halide perovskites, hindering efficiency and stability. Thus further work to optimize conditions for layer-by-layer growth could advance the development of stable and efficient vapour-deposited perovskite solar cells.

REFERENCES

(1) International Energy Agency, World Energy Outlook, www.iea.org/weo.

(2) US Energy Information Administration, *International Energy Outlook 2017*, 2017

(3) Perez, R.; Perez, M. A Fundamental Look at Supply Side Energy Reserves for the Planet. *Sol. Updat.* **2015**, *62*, 4–6.

(4) Department for Business Energy and Industrial Strategy. *Energy Consumption in the UK*; 2018.

(5) World Bank Group, Global Solar Atlas, https://globalsolaratlas.info.

(6) Green, M. A.; Hishikawa, Y.; Dunlop, E. D.; Levi, D. H.; Hohl-Ebinger, J.; Yoshita, M.; Ho-Baillie, A. W. Y. Solar Cell Efficiency Tables (Version 53). *Prog. Photovoltaics* **2019**, *27*, 3–12.

(7) Yang, W. S.; Noh, J. H.; Jeon, N. J.; Kim, Y. C.; Ryu, S.; Seo, J.; Seok, S. Il. High-Performance Photovoltaic Perovskite Layers Fabricated through Intramolecular Exchange. *Science* **2015**, *348*, 1234–1237.

(8) Bi, D.; Tress, W.; Dar, M. I.; Gao, P.; Luo, J.; Renevier, C.; Schenk, K.; Abate, A.; Giordano, F.; Baena, J. C.; et al. Efficient Luminescent Solar Cells Based on Tailored Mixed-Cation Perovskites. *Sci. Adv.* **2016**, *2* (1), e1501170.

(9) Saliba, M.; Matsui, T.; Seo, J.-Y.; Domanski, K.; Correa-Baena, J.-P.; Mohammad K., N.; Zakeeruddin, S. M.; Tress, W.; Abate, A.; Hagfeldt, A.; et al. Cesium-Containing Triple Cation Perovskite Solar Cells: Improved Stability, Reproducibility and High Efficiency. *Energy Environ. Sci.* **2016**, *9*, 1989–1997.

(10) Yang, W. S.; Park, B.-W.; Jung, E. H.; Jeon, N. J.; Kim, Y. C.; Lee, D. U.; Shin, S. S.; Seo, J.; Kim, E. K.; Noh, J. H.; et al. Iodide Management in Formamidinium-Lead-Halide–based Perovskite Layers for Efficient Solar Cells. *Science* **2017**, *356* (6345), 1376–1379.

(11) Chapin, D. M.; Fuller, C. S.; Pearson, G. L. A New Silicon p-n Junction Photocell for Converting Solar Radiation into Electrical Power. *J. Appl. Phys.* **1954**, *25*, 676–677.

(12) Green, M. A.; Emery, K.; Hishikawa, Y.; Warta, W.; Dunlop, E. D. Solar Cell Efficiency Tables. *Prog Photovolt Res Appl.* **2018**, *26*, 427–436.

(13) Jordan, D. C.; Kurtz, S. R. Photovoltaic Degradation Rates — An Analytical Review. *Prog. Photovoltaics Res. Appl.* **2013**, *21* (1), 12–29.

(14) Rajkanan, K.; Singh, R.; Shewchun, J. Absorption Coefficient of Silicon for Solar Cell Calculations. *Solid State Electron.* **1979**, *22*, 793–795.

(15) de Wild-Scholten, M. J. M. Solar Energy Materials & Solar Cells Energy Payback Time and Carbon Footprint of Commercial Photovoltaic Systems. *Sol. Energy Mater. Sol. Cells* **2013**, *119*, 296–305.

(16) Chopra, K. L.; Paulson, P. D.; Dutta, V. Thin-Film Solar Cells: An Overview. *Prog. Photovoltaics Res. Appl.* **2004**, *12*, 69–92.

(17) Yan, J.; Saunders, B. R. Third-Generation Solar Cells: A Review and Comparison of Polymer:Fullerene, Hybrid Polymer and Perovskite Solar Cells. *RSC Adv.* **2014**, *4*, 43286–43314.

(18) Zhang, Y.; Samuel, I. D. W.; Wang, T.; Lidzey, D. G. Current Status of Outdoor Lifetime Testing of Organic Photovoltaics. *Adv. Sci.* **2018**, *5*, 1800434.

(19) Shockley, W.; Queisser, H. J. Detailed Balance Limit of Efficiency of p-n Junction Solar Cells. *J. Appl. Phys.* **1961**, *32* (3), 510–519.

(20) Rühle, S. Tabulated Values of the Shockley-Queisser Limit for Single Junction Solar Cells. *Sol. Energy* **2016**, *130*, 139–147.

(21) Brown, A. S.; Green, M. A. Detailed Balance Limit for the Series Constrained Two Terminal Tandem Solar Cell. *Phys. E* **2002**, *14*, 96–100.

(22) De Vos, A. Detailed Balance Limit of the Efficiency of p-n Junction Solar Cells. *J. Phys. D. Appl. Phys.* **1980**, *13*, 839–846.

(23) Hörantner, M. T.; Leijtens, T.; Ziffer, M. E.; Eperon, G. E.; Christoforo, M. G.; McGehee, M. D.; Snaith, H. J. The Potential of Multijunction Perovskite Solar Cells. *ACS Energy Lett.* **2017**, *2* (10), 2506–2513.

(24) Essig, S.; Allebé, C.; Remo, T.; Geisz, J. F.; Steiner, M. A.; Horowitz, K.; Barraud, L.; Ward, J. S.; Schnabel, M.; Descoeudres, A.; et al. Raising the One-Sun Conversion Efficiency of III-V/Si Solar Cells to 32.8% for Two Junctions

and 35.9% for Three Junctions. *Nat. Energy* **2017**, *2*, 17144.

(25) Eperon, G. E.; Hörantner, M. T.; Snaith, H. J. Metal Halide Perovskite Tandem and Multiple-Junction Photovoltaics. *Nat. Rev. Chem.* **2017**, *1*, 0095.

(26) Weber, D. $CH_3NH_3PbX_3$, Ein Pb(II)-System Mit Kubischer Perowskitstruktur. *Zeitschrift fur Naturforsch.* **1978**, *33b*, 1443–1445.

(27) Kojima, A.; Teshima, K.; Shirai, Y.; Miyasaka, T. Organometal Halide Perovskites as Visible-Light Sensitizers for Photovoltaic Cells. *J. Am. Chem. Soc.* **2009**, *131* (17), 6050–6051.

(28) Lee, M. M.; Teuscher, J.; Miyasaka, T.; Murakami, T. N.; Snaith, H. J. Efficient Hybrid Solar Cells Based on Meso-Superstructured Organometal Halide Perovskites. *Science* **2012**, *338*, 643–648.

(29) Kim, H.-S.; Lee, C.-R.; Im, J.-H.; Lee, K.-B.; Moehl, T.; Marchioro, A.; Moon, S.-J.; Humphry-Baker, R.; Yum, J.-H.; Moser, J. E.; et al. Lead Iodide Perovskite Sensitized All-Solid-State Submicron Thin Film Mesoscopic Solar Cell with Efficiency Exceeding 9%. *Sci. Rep.* **2012**, *2*, 591.

(30) Liu, M.; Johnston, M. B.; Snaith, H. J. Efficient Planar Heterojunction Perovskite Solar Cells by Vapour Deposition. *Nature* **2013**, *501* (7467), 395–398.

(31) Green, M. A.; Ho-Baillie, A.; Snaith, H. J. The Emergence of Perovskite Solar Cells. *Nat. Photonics* **2014**, *8* (7), 506–514.

(32) Egger, D. A.; Bera, A.; Cahen, D.; Hodes, G.; Kirchartz, T.; Kronik, L.; Lovrincic, R.; Rappe, A. M.; Reichman, D. R.; Yaffe, O. What Remains Unexplained about the Properties of Halide Perovskites? *Adv. Mater.* **2018**, 1800691.

(33) Davies, C. L.; Filip, M. R.; Patel, J. B.; Crothers, T. W.; Verdi, C.; Wright, A. D.; Milot, R. L.; Giustino, F.; Johnston, M. B.; Herz, L. M. Bimolecular Recombination in Methylammonium Lead Triiodide Perovskite Is an Inverse Absorption Process. *Nat. Commun.* **2018**, *9* (1), 293.

(34) Herz, L. M. Charge-Carrier Mobilities in Metal Halide Perovskites: Fundamental Mechanisms and Limits. *ACS Energy Lett.* **2017**, *2* (7), 1539–1548.

(35) Stranks, S. D.; Eperon, G. E.; Grancini, G.; Menelaou, C.; Alcocer, M. J. P.;

Leijtens, T.; Herz, L. M.; Petrozza, A.; Snaith, H. J. Electron-Hole Diffusion Lengths Exceeding 1 Micrometer in an Organometal Trihalide Perovskite Absorber. *Science* **2013**, *342* (6156), 341–344.

(36) Wehrenfennig, C.; Eperon, G. E.; Johnston, M. B.; Snaith, H. J.; Herz, L. M. High Charge Carrier Mobilities and Lifetimes in Organolead Trihalide Perovskites. *Adv. Mater.* **2014**, *26* (10), 1584–1589.

(37) Yablonovitch, E. Lead Halides Join the Top Optoelectronic League. *Science* **2016**, *351* (6280), 1401.

(38) Snaith, H. J. Present Status and Future Prospects of Perovskite Photovoltaics. *Nat. Mater.* **2018**, *17* (5), 372–376.

(39) Yin, W.-J.; Shi, T.; Yan, Y. Unusual Defect Physics in $CH_3NH_3PbI_3$ Perovskite Solar Cell Absorber. *Appl. Phys. Lett.* **2014**, *104* (6), 063903.

(40) Herz, L. M. Charge-Carrier Dynamics in Organic-Inorganic Metal Halide Perovskites. *Annu. Rev. Phys. Chem.* **2016**, *67*, 65–89.

(41) Razza, S.; Castro-Hermosa, S.; Di Carlo, A.; Brown, T. M. Research Update: Large-Area Deposition, Coating, Printing, and Processing Techniques for the Upscaling of Perovskite Solar Cell Technology. *APL Mater.* **2016**, *4*, 091508.

(42) Bishop, J. E.; Routledge, T. J.; Lidzey, D. G. Advances in Spray-Cast Perovskite Solar Cells. *J. Phys. Chem. Lett.* **2018**, *9*, 1977–1984.

(43) Hao, F.; Stoumpos, C. C.; Chang, R. P. H.; Kanatzidis, M. G. Anomalous Band Gap Behavior in Mixed Sn and Pb Perovskites Enables Broadening of Absorption Spectrum in Solar Cells. *J. Am. Chem. Soc.* **2014**, *136* (22), 8094–8099.

(44) Eperon, G. E.; Leijtens, T.; Bush, K. A.; Prasanna, R.; Green, T.; Wang, Jacob Tse-Wei Mcmeekin, D. P.; Volonakis, G.; Milot, R. L.; May, R.; Palmstrom, A.; et al. Perovskite-Perovskite Tandem Photovoltaics with Optimized Band Gaps. *Science* **2016**, *364* (6314), 861–864.

(45) Weber, O. J.; Charles, B.; Weller, M. T. Phase Behaviour and Composition in the Formamidinium–methylammonium Hybrid Lead Iodide Perovskite Solid Solution. *J. Mater. Chem. A* **2016**, *4* (40), 15375–15382.

(46) Prasanna, R.; Gold-Parker, A.; Leijtens, T.; Conings, B.; Babayigit, A.; Boyen, H. G.; Toney, M. F.; McGehee, M. D. Band Gap Tuning via Lattice Contraction and Octahedral Tilting in Perovskite Materials for Photovoltaics. *J. Am. Chem. Soc.* **2017**, *139* (32), 11117–11124.

(47) Rehman, W.; McMeekin, D. P.; Patel, J. B.; Milot, R. L.; Johnston, M. B.; Snaith, H. J.; Herz, L. M. Photovoltaic Mixed-Cation Lead Mixed-Halide Perovskites: Links between Crystallinity, Photo-Stability and Electronic Properties. *Energy Environ. Sci.* **2017**, *10* (1), 361–369.

(48) Xing, G.; Mathews, N.; Lim, S. S.; Yantara, N.; Liu, X.; Sabba, D.; Grätzel, M.; Mhaisalkar, S.; Sum, T. C. Low-Temperature Solution-Processed Wavelength-Tunable Perovskites for Lasing. *Nat. Mater.* **2014**, *13* (5), 476–480.

(49) Noh, J. H.; Im, S. H.; Heo, J. H.; Mandal, T. N.; Seok, S. Il. Chemical Management for Colorful, Efficient, and Stable Inorganic-Organic Hybrid Nanostructured Solar Cells. *Nano Lett.* **2013**, *13* (4), 1764–1769.

(50) Eperon, G. E.; Stranks, S. D.; Menelaou, C.; Johnston, M. B.; Herz, L. M.; Snaith, H. J. Formamidinium Lead Trihalide: A Broadly Tunable Perovskite for Efficient Planar Heterojunction Solar Cells. *Energy Environ. Sci.* **2014**, *7* (3), 982–988.

(51) Sutton, R. J.; Eperon, G. E.; Miranda, L.; Parrott, E. S.; Kamino, B. A.; Patel, J. B.; Hörantner, M. T.; Johnston, M. B.; Haghighirad, A. A.; Moore, D. T.; et al. Bandgap-Tunable Cesium Lead Halide Perovskites with High Thermal Stability for Efficient Solar Cells. *Adv. Energy Mater.* **2016**, *6* (8), 1502458.

(52) Zhao, D.; Yu, Y.; Wang, C.; Liao, W.; Shrestha, N.; Grice, C. R.; Cimaroli, A. J.; Guan, L.; Ellingson, R. J.; Zhu, K.; et al. Low-Bandgap Mixed Tin–lead Iodide Perovskite Absorbers with Long Carrier Lifetimes for All-Perovskite Tandem Solar Cells. *Nat. Energy* **2017**, *2*, 17018.

(53) Rajagopal, A.; Yang, Z.; Jo, S. B.; Braly, I. L.; Liang, P. W.; Hillhouse, H. W.; Jen, A. K. Y. Highly Efficient Perovskite–Perovskite Tandem Solar Cells Reaching 80% of the Theoretical Limit in Photovoltage. *Adv. Mater.* **2017**, *29* (34), 1702140.

(54) NREL. Best Research-Cell Efficiencies 2019

https://www.nrel.gov/pv/assets/pdfs/pv-efficiency-chart.20190103.pdf.

(55) Noel, N. K.; Stranks, S. D.; Abate, A.; Wehrenfennig, C.; Guarnera, S.; Haghighirad, A.; Sadhanala, A.; Eperon, G. E.; Pathak, S. K.; Johnston, M. B.; et al. Lead-Free Organic-Inorganic Tin Halide Perovskites for Photovoltaic Applications. *Energy Environ. Sci.* **2014**, *7*, 3061–3068.

(56) Hao, F.; Stoumpos, C. C.; Cao, D. H.; Chang, R. P. H.; Kanatzidis, M. G. Lead-Free Solid-State Organic–inorganic Halide Perovskite Solar Cells. *Nat. Photonics* **2014**, *8* (6), 489–494.

(57) Hao, F.; Stoumpos, C. C.; Guo, P.; Zhou, N.; Marks, T. J.; Chang, R. P. H.; Kanatzidis, M. G. Solvent-Mediated Crystallization of $CH_3NH_3SnI_3$ Films for Heterojunction Depleted Perovskite Solar Cells. *J. Am. Chem. Soc.* **2015**, *137* (35), 11445–11452.

(58) Zhao, Z.; Gu, F.; Li, Y.; Sun, W.; Ye, S.; Rao, H.; Liu, Z.; Bian, Z.; Huang, C. Mixed-Organic-Cation Tin Iodide for Lead-Free Perovskite Solar Cells with an Efficiency of 8.12%. *Adv. Sci.* **2017**, *4* (11), 1700204.

(59) Dang, Y.; Zhou, Y.; Liu, X.; Ju, D.; Xia, S.; Xia, H.; Tao, X. Formation of Hybrid Perovskite Tin Iodide Single Crystals by Top-Seeded Solution Growth. *Angew. Chemie - Int. Ed.* **2016**, *55* (10), 3447–3450.

(60) Liu, X.; Yang, Z.; Chueh, C.-C.; Rajagopal, A.; Williams, S. T.; Sun, Y.; Jen, A. K.-Y. Improved Efficiency and Stability of Pb-Sn Binary Perovskite Solar Cells by Cs Substitution. *J. Mater. Chem. A* **2016**, *4*, 17939–17945.

(61) Noel, N. K.; Abate, A.; Stranks, S. D.; Parrott, E. S.; Burlakov, V. M.; Goriely, A.; Snaith, H. J. Enhanced Photoluminescence and Solar Cell Performance via Lewis Base Passivation of Organic-Inorganic Lead Halide Perovskites. *ACS Nano* **2014**, *8* (10), 9815–9821.

(62) Yamada, K.; Matsui, T.; Tsuritani, T.; Okuda, T.; Ichiba, S. ^{127}I-NQR , ^{119}Sn Mössbauer Effect , and Electrical Conductivity of $MSnI_3$ (M = K, NH_4, Rb, Cs, and CH_3NH_3). *Zeitschrift für Naturforsch.* **1990**, *45A*, 307–312.

(63) Stranks, S. D.; Snaith, H. J. Metal-Halide Perovskites for Photovoltaic and Light-Emitting Devices. *Nat. Nanotechnol.* **2015**, *10* (5), 391–402.

(64) Dar, M. I.; Jacopin, G.; Meloni, S.; Mattoni, A.; Arora, N.; Boziki, A.; Zakeeruddin, S. M.; Rothlisberger, U.; Gratzel, M. Origin of Unusual Bandgap Shift and Dual Emission in Organic-Inorganic Lead Halide Perovskites. *Sci. Adv.* **2016**, *2* (10), e1601156.

(65) Kim, J.; Lee, S.-C.; Lee, S.-H.; Hong, K.-H. Importance of Orbital Interactions in Determining Electronic Band Structures of Organo-Lead Iodide. *J. Phys. Chem. C* **2015**, *119* (9), 4627–4634.

(66) Glazer, A. M. The Classification of Tilted Octahedra in Perovskites. *Acta Crystallogr. Sect. B Struct. Crystallogr. Cryst. Chem.* **1972**, *28* (11), 3384–3392.

(67) Chen, T.; Foley, B. J.; Park, C.; Brown, C. M.; Harriger, L. W.; Lee, J.; Ruff, J.; Yoon, M.; Choi, J. J.; Lee, S.-H. Entropy-Driven Structural Transition and Kinetic Trapping in Formamidinium Lead Iodide Perovskite. *Sci. Adv.* **2016**, *2*, e1601650.

(68) Schueller, E. C.; Laurita, G.; Fabini, D. H.; Stoumpos, C. C.; Kanatzidis, M. G.; Seshadri, R. Crystal Structure Evolution and Notable Thermal Expansion in Hybrid Perovskites Formamidinium Tin Iodide and Formamidinium Lead Bromide. *Inorg. Chem.* **2018**, *57* (2), 695–701.

(69) Stoumpos, C. C.; Malliakas, C. D.; Kanatzidis, M. G. Semiconducting Tin and Lead Iodide Perovskites with Organic Cations: Phase Transitions, High Mobilities, and near-Infrared Photoluminescent Properties. *Inorg. Chem.* **2013**, *52* (15), 9019–9038.

(70) Travis, W.; Glover, E. N. K.; Bronstein, H.; Scanlon, D. O.; Palgrave, R. G. On the Application of the Tolerance Factor to Inorganic and Hybrid Halide Perovskites: A Revised System. *Chem. Sci.* **2016**, *7*, 4548–4556.

(71) Milot, R. L.; Eperon, G. E.; Snaith, H. J.; Johnston, M. B.; Herz, L. M. Temperature-Dependent Charge-Carrier Dynamics in $CH_3NH_3PbI_3$ Perovskite Thin Films. *Adv. Funct. Mater.* **2015**, *25* (39), 6218–6227.

(72) Yin, W.-J.; Yang, J.-H.; Kang, J.; Yan, Y.; Wei, S.-H. Halide Perovskite Materials for Solar Cells: A Theoretical Review. *J. Mater. Chem. A* **2015**, *3* (17), 8926–8942.

(73) da Silva, E. L.; Skelton, J. M.; Parker, S. C.; Walsh, A. Phase Stability and

Transformations in the Halide Perovskite CsSnI3. *Phys. Rev. B* **2015**, *91* (14), 144107.

(74) Even, J.; Pedesseau, L.; Katan, C.; Kepenekian, M.; Lauret, J.-S.; Sapori, D.; Deleporte, E. Solid State Physics Perspective on Hybrid Perovskite Semiconductors. *J. Phys. Chem. C* **2015**, *119* (19), 10161–10177.

(75) Mosconi, E.; Amat, A.; Nazeeruddin, K.; Gra, M.; Angelis, F. De. First-Principles Modeling of Mixed Halide Organometal Perovskites for Photovoltaic Applications. *J. Phys. Chem. C* **2013**, *117*, 13902–13913.

(76) Filip, M. R.; Verdi, C.; Giustino, F. GW Band Structures and Carrier Effective Masses of $CH_3NH_3PbI_3$ and Hypothetical Perovskites of the Type $APbI_3$: A = NH_4, PH_4, AsH_4 and SbH_4. *J. Phys. Chem. C* **2015**, *119* (45), 25209.

(77) Umari, P.; Mosconi, E.; De Angelis, F. Relativistic GW Calculations on $CH_3NH_3PbI_3$ and $CH_3NH_3SnI_3$ Perovskites for Solar Cell Applications. *Sci. Rep.* **2014**, *4*, 4467.

(78) Van Vechten, J. A.; Bergstresser, T. K. Electronic Structures of Semiconductor Alloys. *Phys. Rev. B* **1970**, *1* (8), 3351–3358.

(79) Vurgaftman, I.; Meyer, J. R.; Ram-Mohan, L. R. Band Parameters for III-V Compound Semiconductors and Their Alloys. *J. Appl. Phys.* **2001**, *89* (11), 5815–5875.

(80) Vegard, L. Die Konstitution Der Mischkristalle Und Die Raumfullung Der Atome. *Zeitschrift fur Phys.* **1921**, *5* (1), 17–26.

(81) Hernandez-Calderon, I. Optical Properties and Electronic Structure of Wide Band Gap II-VI Semiconductors. In *II-VI Semiconductor Materials and Their Applications*; Tamargo, M. C., Ed.; Taylor and Francis New York, 2002; pp 113–170.

(82) Schnohr, C. S. Compound Semiconductor Alloys: From Atomic-Scale Structure to Bandgap Bowing. *Appl. Phys. Rev.* **2015**, *2*, 031304.

(83) Boyce, J. B.; Mikkelsen, J. C. Local Structure of Pseudobinary Semiconductor Alloys: An X-Ray Absorption Fine Structure Study. *J. Cryst. Growth* **1989**, *98*, 37–43.

(84) Shan, W.; Walukiewicz, W.; Ager, J.; Haller, E.; Geisz, J.; Friedman, D.; Olson, J.; Kurtz, S. Band Anticrossing in GaInNAs Alloys. *Phys. Rev. Lett.* **1999**, *82* (6), 1221–1224.

(85) Wu, J.; Shan, W.; Walukiewicz, W. Band Anticrossing in Highly Mismatched III-V Semiconductor Alloys. *Semicond. Sci. Technol.* **2002**, *17* (8), 860.

(86) Yu, K. M.; Novikov, S. V.; Broesler, R.; Levander, A. X.; Liliental-Weber, Z.; Luckert, F.; Martin, R. W.; Dubon, O.; Wu, J.; Walukiewicz, W.; et al. GaNAs Alloys over the Whole Composition Range Grown on Crystalline and Amorphous Substrates. *Phys. Status Solidi C* **2011**, *8* (7–8), 2503–2505.

(87) Im, J.; Stoumpos, C. C.; Jin, H.; Freeman, A. J.; Kanatzidis, M. G. Antagonism between Spin-Orbit Coupling and Steric Effects Causes Anomalous Bandgap Evolution in the Perovskite Photovoltaic Materials $CH_3NH_3Sn_{1-x}Pb_xI_3$. *J. Phys. Chem. Lett.* **2015**, *6*, 3203–3509.

(88) Zhao, B.; Abdi-Jalebi, M.; Tabachnyk, M.; Glass, H.; Kamboj, V. S.; Nie, W. A.; Pearson, J.; Puttisong, Y.; Gödel, K. C.; Beere, H. E.; et al. High Open-Circuit Voltages in Tin-Rich Low-Bandgap Perovskite-Based Planar Heterojunction Photovoltaics. *Adv. Mater.* **2016**, *29* (2), 1604744.

(89) Anaya, M.; Correa-Baena, J. P.; Lozano, G.; Saliba, M.; Anguita, P.; Roose, B.; Abate, A.; Steiner, U.; Grätzel, M.; Calvo, M. E.; et al. Optical Analysis of $CH_3NH_3Sn_xPb_{1-x}I_3$ Absorbers: A Roadmap for Perovskite-on-Perovskite Tandem Solar Cells. *J. Mater. Chem. A* **2016**, *4* (29), 11214–11221.

(90) Liu, C.; Fan, J.; Li, H.; Zhang, C.; Mai, Y. Highly Efficient Perovskite Solar Cells with Substantial Reduction of Lead Content. *Sci. Rep.* **2016**, *6*, 35705.

(91) Yang, Z.; Rajagopal, A.; Chueh, C.; Jo, S. B.; Liu, B.; Zhao, T.; Jen, A. K. Stable Low-Bandgap Pb-Sn Binary Perovskites for Tandem Solar Cells. *Adv. Mater.* **2016**, *28* (40), 8990–8997.

(92) Stoumpos, C. C.; Kanatzidis, M. G. The Renaissance of Halide Perovskites and Their Evolution as Emerging Semiconductors. *Acc. Chem. Res.* **2015**, *48*, 2791–2802.

(93) Yu, C.; Chen, Z.; Wang, J.; Pfenninger, W.; Vockic, N.; Kenney, J. T.; Shum, K. Temperature Dependence of the Band Gap of Perovskite Semiconductor

Compound $CsSnI_3$. *J. Appl. Phys.* **2011**, *110* (6), 063526.

(94) Wright, A. D.; Verdi, C.; Milot, R. L.; Eperon, G. E.; Pérez-Osorio, M. A.; Snaith, H. J.; Giustino, F.; Johnston, M. B.; Herz, L. M. Electron–phonon Coupling in Hybrid Lead Halide Perovskites. *Nat. Commun.* **2016**, *7*, 11755.

(95) Parrott, E. S.; Milot, R. L.; Stergiopoulos, T.; Snaith, H. J.; Johnston, M. B.; Herz, L. M. Effect of Structural Phase Transition on Charge-Carrier Lifetimes and Defects in $CH_3NH_3SnI_3$ Perovskite. *J. Phys. Chem. Lett.* **2016**, *7*, 1321–1326.

(96) Varshni, Y. P. Temperature Dependence of the Energy Gap in Semiconductors. *Physica* **1967**, *34* (1), 149–154.

(97) Allen, P. B.; Heine, V. Theory of the Temperature Dependence of Electronic Band Structures. *J. Phys. C Solid State Phys.* **1976**, *9* (12), 2305–2312.

(98) Fan, H. Y. Temperature Dependence of the Energy Gap in Semiconductors. *Phys. Rev.* **1951**, *82* (6), 900–905.

(99) Göbel, A.; Ruf, T.; Cardona, M.; Lin, C. T.; Wrzesinski, J.; Steube, M.; Reimann, K.; Merle, J.-C.; Joucla, M. Effects of the Isotopic Composition on the Fundamental Gap of CuCl. *Phys. Rev. B* **1998**, *57* (24), 15183–15190.

(100) Whalley, L. D.; Skelton, J. M.; Frost, J. M.; Walsh, A. Phonon Anharmonicity, Lifetimes, and Thermal Transport in $CH_3NH_3PbI_3$ from Many-Body Perturbation Theory. *Phys. Rev. B* **2016**, *94* (22), 220301.

(101) Kim, H.; Hunger, J.; Cánovas, E.; Karakus, M.; Mics, Z.; Grechko, M.; Turchinovich, D.; Parekh, S. H.; Bonn, M. Direct Observation of Mode-Specific Phonon-Band Gap Coupling in Methylammonium Lead Halide Perovskites. *Nat. Commun.* **2017**, *8* (1), 687.

(102) Wu, K.; Bera, A.; Ma, C.; Du, Y.; Yang, Y.; Li, L.; Wu, T. Temperature-Dependent Excitonic Photoluminescence of Hybrid Organometal Halide Perovskite Films. *Phys. Chem. Chem. Phys.* **2014**, *16* (41), 22476–22481.

(103) Kayanuma, Y. Quantum-Size Effects of Interacting Electrons and Holes in Semiconductor Microcrystals with Spherical Shape. *Phys. Rev. B* **1988**, *38* (14), 9797–9805.

(104) Miyata, A.; Mitioglu, A.; Plochocka, P.; Portugall, O.; Wang, J. T.-W.; Stranks, S. D.; Snaith, H. J.; Nicholas, R. J. Direct Measurement of the Exciton Binding Energy and Effective Masses for Charge Carriers in Organic-Inorganic Tri-Halide Perovskites. *Nat. Phys.* **2015**, *11*, 582–587.

(105) Even, J.; Pedesseau, L.; Katan, C. Analysis of Multivalley and Multibandgap Absorption and Enhancement of Free Carriers Related to Exciton Screening in Hybrid Perovskites. *J. Phys. Chem. C* **2014**, *118* (22), 11566–11572.

(106) Keldysh, L. V. Coulomb Interaction in Thin Semiconductor and Semimetal Films. *Sov. J. Exp. Theor. Phys. Lett.* **1979**, *29* (11), 658.

(107) Tanaka, K.; Takahashi, T.; Kondo, T.; Umebayashi, T.; Asai, K.; Ema, K. Image Charge Effect on Two-Dimensional Excitons in an Inorganic-Organic Quantum-Well Crystal. *Phys. Rev. B* **2005**, *71*, 045312.

(108) Malgras, V.; Henzie, J.; Takei, T.; Yamauchi, Y. Hybrid Methylammonium Lead Halide Perovskite Nanocrystals Confined in Gyroidal Silica Templates. *Chem. Commun.* **2017**, *53* (15), 2359–2362.

(109) Demchyshyn, S.; Roemer, J. M.; Groiß, H.; Heilbrunner, H.; Ulbricht, C.; Apaydin, D.; Böhm, A.; Rütt, U.; Bertram, F.; Hesser, G.; et al. Confining Metal-Halide Perovskites in Nanoporous Thin Films. *Sci. Adv.* **2017**, *3* (8), e1700738.

(110) Wang, L.; Williams, N. E.; Malachosky, E. W.; Otto, J. P.; Hayes, D.; Wood, R. E.; Guyot-Sionnest, P.; Engel, G. S. Scalable Ligand-Mediated Transport Synthesis of Organic-Inorganic Hybrid Perovskite Nanocrystals with Resolved Electronic Structure and Ultrafast Dynamics. *ACS Nano* **2017**, *11* (3), 2689–2696.

(111) Protesescu, L.; Yakunin, S.; Bodnarchuk, M. I.; Krieg, F.; Caputo, R.; Hendon, C. H.; Yang, R. X.; Walsh, A.; Kovalenko, M. V. Nanocrystals of Cesium Lead Halide Perovskites ($CsPbX_3$, X = Cl, Br, and I): Novel Optoelectronic Materials Showing Bright Emission with Wide Color Gamut. *Nano Lett.* **2015**, *15*, 3692–3696.

(112) Ball, J. M.; Petrozza, A. Defects in Perovskite-Halides and Their Effects in Solar Cells. *Nat. Energy* **2016**, *1* (11), 16149.

(113) Kruger, F. A.; Vink, H. J. Relations Between the Concentrations of

Imperfections in Solids. *J. Phys. Chem. Solids* **1958**, *5*, 208–223.

(114) Zunger, A. Practical Doping Principles. *Appl. Phys. Lett.* **2003**, *83* (1), 57–59.

(115) Takahashi, Y. Y.; Hasegawa, H.; Takahashi, Y. Y.; Inabe, T. Hall Mobility in Tin Iodide Perovskite $CH_3NH_3SnI_3$: Evidence for a Doped Semiconductor. *J. Solid State Chem.* **2013**, *205*, 39–43.

(116) Kumar, M. H.; Dharani, S.; Leong, W. L.; Boix, P. P.; Prabhakar, R. R.; Baikie, T.; Shi, C.; Ding, H.; Ramesh, R.; Asta, M.; et al. Lead-Free Halide Perovskite Solar Cells with High Photocurrents Realized Through Vacancy Modulation. *Adv. Mater.* **2014**, *26*, 7122–7127.

(117) Chung, I.; Song, J. H.; Im, J.; Androulakis, J.; Malliakas, C. D.; Li, H.; Freeman, A. J.; Kenney, J. T.; Kanatzidis, M. G. $CsSnI_3$: Semiconductor or Metal? High Electrical Conductivity and Strong Near-Infrared Photoluminescence from a Single Material. High Hole Mobility and Phase-Transitions. *J. Am. Chem. Soc.* **2012**, *134* (20), 8579–8587.

(118) Koh, T. M.; Krishnamoorthy, T.; Yantara, N.; Shi, C.; Leong, W. L.; Boix, P. P.; Grimsdale, A. C.; Mhaisalkar, S. G.; Mathews, N. Formamidinium Tin-Based Perovskite with Low E_g for Photovoltaic Applications. *J. Mater. Chem. A* **2015**, *3*, 14996–15000.

(119) Leijtens, T.; Prasanna, R.; Gold-Parker, A.; Toney, M. F.; McGehee, M. D. Mechanism of Tin Oxidation and Stabilization by Lead Substitution in Tin Halide Perovskites. *ACS Energy Lett.* **2017**, *2* (9), 2159–2165.

(120) Konstantakou, M.; Stergiopoulos, T. A Critical Review on Tin Halide Perovskite Solar Cells. *J. Mater. Chem. A* **2017**, *5*, 11518–11549.

(121) Song, T. Bin; Yokoyama, T.; Stoumpos, C. C.; Logsdon, J.; Cao, D. H.; Wasielewski, M. R.; Aramaki, S.; Kanatzidis, M. G. Importance of Reducing Vapor Atmosphere in the Fabrication of Tin-Based Perovskite Solar Cells. *J. Am. Chem. Soc.* **2017**, *139* (2), 836–842.

(122) Takahashi, Y. Y.; Obara, R.; Lin, Z.-Z.; Takahashi, Y. Y.; Naito, T.; Inabe, T.; Ishibashi, S.; Terakura, K. Charge-Transport in Tin-Iodide Perovskite $CH_3NH_3SnI_3$: Origin of High Conductivity. *Dalton Trans.* **2011**, *40* (20), 5563–

5568.

(123) Marshall, K. P.; Walton, R. I.; Hatton, R. A. Tin Perovskite / Fullerene Planar Layer Photovoltaics: Improving the Efficiency and Stability of Lead-Free Devices. *J. Mater. Chem. A* **2015**, *3*, 11631–11640.

(124) Xu, P.; Chen, S.; Xiang, H.; Gong, X.; Wei, S. Influence of Defects and Synthesis Conditions on the Photovoltaic Performance of Perovskite Semiconductor $CsSnI_3$. *Chem. Mater.* **2014**, *26*, 6068–6072.

(125) Shockley, W.; Read, W. T. Statistics of the Recombination of Holes and Electrons. *Phys. Rev.* **1952**, *87* (46), 835–842.

(126) Meggiolaro, D.; Motti, S. G.; Mosconi, E.; Barker, A. J.; Ball, J.; Andrea Riccardo Perini, C.; Deschler, F.; Petrozza, A.; De Angelis, F. Iodine Chemistry Determines the Defect Tolerance of Lead-Halide Perovskites. *Energy Environ. Sci.* **2018**, *11* (3), 702–713.

(127) Chen, Y.; Kothiyal, G. P.; Singh, J.; Bhattacharya, P. K. Absorption and Photoluminescence Studies of the Temperature Dependence of Exciton Life Time in Lattice-Matched and Strained Quantum Well Systems. *Superlattices Microstruct.* **1987**, *3* (6), 657–664.

(128) Richter, J. M.; Abdi-Jalebi, M.; Sadhanala, A.; Tabachnyk, M.; Rivett, J. P. H.; Pazos-Outón, L. M.; Gödel, K. C.; Price, M.; Deschler, F.; Friend, R. H. Enhancing Photoluminescence Yields in Lead Halide Perovskites by Photon Recycling and Light Out-Coupling. *Nat. Commun.* **2016**, *7*, 13941.

(129) Milot, R. L.; Sutton, R. J.; Eperon, G. E.; Haghighirad, A. A.; Martinez Hardigree, J.; Miranda, L.; Snaith, H. J.; Johnston, M. B.; Herz, L. M. Charge-Carrier Dynamics in 2D Hybrid Metal-Halide Perovskites. *Nano Lett.* **2016**, *16* (11), 7001–7007.

(130) Wehrenfennig, C.; Liu, M.; Snaith, H. J.; Johnston, M. B.; Herz, L. M. Charge-Carrier Dynamics in Vapour-Deposited Films of the Organolead Halide Perovskite $CH_3NH_3PbI_{3-x}Cl_X$. *Energy Environ. Sci.* **2014**, *7*, 2269.

(131) Rehman, W.; Milot, R. L.; Eperon, G. E.; Wehrenfennig, C.; Boland, J. L.; Snaith, H. J.; Johnston, M. B.; Herz, L. M. Charge-Carrier Dynamics and Mobilities in Formamidinium Lead Mixed-Halide Perovskites. *Adv. Mater.* **2015**,

27 (48), 7938–7944.

(132) Xing, G.; Mathews, N.; Sun, S.; Lim, S. S.; Lam, Y. M.; Grätzel, M.; Mhaisalkar, S.; Sum, T. C. Long-Range Balanced Electron- and Hole-Transport Lengths in Organic-Inorganic $CH_3NH_3PbI_3$. *Science* **2013**, *342* (6156), 344–347.

(133) Herz, L. M. How Lattice Dynamics Moderate the Electronic Properties of Metal-Halide Perovskites. *J. Phys. Chem. Lett.* **2018**, *9*, 6853–6863.

(134) Milot, R. L.; Klug, M. T.; Davies, C. L.; Wang, Z.; Kraus, H.; Snaith, H. J.; Johnston, M. B.; Herz, L. M. The Effects of Doping Density and Temperature on the Optoelectronic Properties of Formamidinium Tin Triiodide Thin Films. *Adv. Matterials* **2018**, *20*, 1804506.

(135) Milot, R. L.; Eperon, G. E.; Green, T.; Snaith, H. J.; Johnston, M. B.; Herz, L. M. Radiative Monomolecular Recombination Boosts Amplified Spontaneous Emission in $HC(NH_2)_2SnI_3$ Perovskite Films. *J. Phys. Chem. Lett.* **2016**, *7* (20), 4178–4184.

(136) Wertheim, G. K. Transient Recombination of Excess Carriers in Semiconductors. *Phys. Rev.* **1958**, *109* (4), 1086–1091.

(137) Huang, J.; Yuan, Y.; Shao, Y.; Yan, Y. Understanding the Physical Properties of Hybrid Perovskites for Photovoltaic Applications. *Nat. Rev. Mater.* **2017**, *2*, 17042.

(138) Kim, J.; Lee, S.-H.; Lee, J. H.; Hong, K.-H. The Role of Intrinsic Defects in Methylammonium Lead Iodide Perovskite. *J. Phys. Chem. Lett.* **2014**, *5* (8), 1312–1317.

(139) Hall, R. N. Recombination Processes in Semiconductors. *Proc. IEE - Part B Electron. Commun. Eng.* **1959**, *106* (17S), 923–931.

(140) Alkauskas, A.; Yan, Q.; Van De Walle, C. G. First-Principles Theory of Nonradiative Carrier Capture via Multiphonon Emission. *Phys. Rev. B - Condens. Matter Mater. Phys.* **2014**, *90*, 075202.

(141) Bonch-Bruevich, V. L.; Landsberg, E. G. Recombination Mechanisms. *Phys. Status Solidi* **1968**, *29* (1), 9–43.

(142) Lax, M. Giant Traps. *J. Phys. Chem. Solids* **1959**, *8*, 66–73.

(143) Monroe, D. Hopping in Exponential Band Tails. *Phys. Rev. Lett.* **1985**, *54* (2), 146–149.

(144) Wright, A. D.; Milot, R. L.; Eperon, G. E.; Snaith, H. J.; Johnston, M. B.; Herz, L. M. Band-Tail Recombination in Hybrid Lead Iodide Perovskite. *Adv. Funct. Mater.* **2017**, *27*, 1700860.

(145) Robbins, D. J.; Landsberg, P. T. Impact Ionisation and Auger Recombination Involving Traps in Semiconductors. *J. Phys. C Solid State Phys.* **1980**, *13*, 2425–2439.

(146) Stranks, S. D.; Burlakov, V. M.; Leijtens, T.; Ball, J. M.; Goriely, A.; Snaith, H. J. Recombination Kinetics in Organic-Inorganic Perovskites: Excitons, Free Charge, and Subgap States. *Phys. Rev. Appl.* **2014**, *2* (3), 034007.

(147) Leijtens, T.; Eperon, G.; Barker, A.; Grancini, G.; Zhang, W.; Ball, J.; Srimath Kandada, A. R.; Snaith, H.; Petrozza, A. Carrier Trapping and Recombination: The Role of Defect Physics in Enhancing the Open Circuit Voltage of Metal Halide Perovskite Solar Cells. *Energy Environ. Sci.* **2016**, *9* (11), 3472–3481.

(148) Leroux, M.; Grandjean, N.; Beaumont, B.; Nataf, G.; Semond, F.; Massies, J.; Gibart, P. Temperature Dependence of Photoluminescence Intensities of Undoped and Doped GaN. *Phys. Status Solidi Basic Res.* **1999**, *216* (1), 605–608.

(149) Fang, H.; Wang, F.; Adjokatse, S.; Zhao, N.; Even, J.; Loi, M. A. Photoexcitation Dynamics in Solution- Processed Formamidinium Lead Iodide Perovskite Thin Films for Solar Cell Applications. *Light Sci. Appl.* **2016**, *5*, e16056.

(150) Sun, S.; Salim, T.; Mathews, N.; Duchamp, M.; Boothroyd, C.; Xing, G.; Sum, T. C.; Lam, Y. M. The Origin of High Efficiency in Low-Temperature Solution-Processable Bilayer Organometal Halide Hybrid Solar Cells. *Energy Environ. Sci.* **2014**, *7* (1), 399.

(151) Savenije, T. J.; Ponseca, C. S.; Kunneman, L.; Abdellah, M.; Zheng, K.; Tian, Y.; Zhu, Q.; Canton, S. E.; Scheblykin, I. G.; Pullerits, T.; et al. Thermally Activated Exciton Dissociation and Recombination Control the Carrier Dynamics in Organometal Halide Perovskite. *J. Phys. Chem. Lett.* **2014**, *5*, 2189–2194.

(152) Steiner, M. A.; Geisz, J. F.; García, I.; Friedman, D. J.; Duda, A.; Kurtz, S. R. Optical Enhancement of the Open-Circuit Voltage in High Quality GaAs Solar Cells. *J. Appl. Phys.* **2013**, *113*, 123109.

(153) Crothers, T. W.; Milot, R. L.; Patel, J. B.; Parrott, E. S.; Schlipf, J.; Müller-Buschbaum, P.; Johnston, M. B.; Herz, L. M. Photon Reabsorption Masks Intrinsic Bimolecular Charge-Carrier Recombination in $CH_3NH_3PbI_3$ Perovskite. *Nano Lett.* **2017**, *17* (9), 5782–5789.

(154) Elliott, R. J. Intensity of Optical Absorption by Excitons. *Phys. Rev.* **1957**, *108* (6), 1384–1389.

(155) Scherrer, P. Estimation of the Size and Internal Structure of Colloidal Particles by Means of Röntgen. *Göttinger Nachrichten Math. Phys.* **1918**, *26*, 98–100.

(156) Langford, J. I.; Wilson, A. J. C. Scherrer after Sixty Years: A Survey and Some New Results in the Determination of Crystallite Size. *J. Appl. Cryst.* **1978**, *11*, 102–113.

(157) Williamson, G. .; Hall, W. . X-Ray Line Broadening from Filed Aluminium and Wolfram. *Acta Metall.* **1953**, *1* (1), 22–31.

(158) Patel, J. B.; Wong-Leung, J.; Van Reenen, S.; Sakai, N.; Wang, J. T. W.; Parrott, E. S.; Liu, M.; Snaith, H. J.; Herz, L. M.; Johnston, M. B. Influence of Interface Morphology on Hysteresis in Vapor-Deposited Perovskite Solar Cells. *Adv. Electron. Mater.* **2017**, *3* (2), 1600470.

(159) Benmessaoud, I. R.; Mahul-Mellier, A.-L.; Horvath, E.; Maco, B.; Spina, M.; Lashuel, H.; Forro, L. Health Hazard of the Methylammonium Lead Iodide Based Perovskites: Cytotoxicity Studies. *Toxicol. Res.* **2016**, *5* (2), 357–720.

(160) Espinosa, N.; Serrano-Luian, L.; Urbina, A.; Krebs, F. C. Solution and Vapour Deposited Lead Perovskite Solar Cells: Ecotoxicity from a Life Cycle Assessment Perspective. *Sol. Energy Mater. Sol. Cells* **2015**, *137*, 303–310.

(161) Zhang, J.; Gao, X.; Deng, Y.; Li, B.; Yuan, C. Life Cycle Assessment of Titania Perovskite Solar Cell Technology for Sustainable Design and Manufacturing. *ChemSusChem* **2015**, *8* (22), 3882–3891.

(162) Babayigit, A.; Duy Thanh, D.; Ethirajan, A.; Manca, J.; Muller, M.; Boyen, H.-

G.; Conings, B. Assessing the Toxicity of Pb- and Sn-Based Perovskite Solar Cells in Model Organism Danio Rerio. *Sci. Rep.* **2016**, *6*, 18721.

(163) Mitzi, D.; Feild, C. Transport, Optical and Magnetic Properties of the Conducting Halide Perovskite $CH_3NH_3SnI_3$. *J. Solid State Chem.* **1995**, *114*, 159–163.

(164) Yamada, K.; Nakada, K.; Takeuchi, Y.; Nawa, K.; Yamane, Y. Tunable Perovskite Semiconductor $CH_3NH_3SnX_3$ (X: Cl, Br, or I) Characterized by X-Ray and DTA. *Bull. Chem. Soc. Jpn.* **2011**, *84* (9), 926–932.

(165) Wehrenfennig, C.; Liu, M.; Snaith, H. J.; Johnston, M. B.; Herz, L. M. Charge Carrier Recombination Channels in the Low-Temperature Phase of Organic-Inorganic Lead Halide Perovskite Thin Films. *APL Mater.* **2014**, *2* (8), 081513.

(166) Stamplecoskie, K. G.; Manser, J. S.; Kamat, P. V. Dual Nature of the Excited State in Organic–inorganic Lead Halide Perovskites. *Energy Environ. Sci.* **2015**, *8* (1), 208–215.

(167) Christians, J. A.; Manser, J. S.; Kamat, P. V. The Multifaceted Excited State of $CH_3NH_3PbI_3$. Charge Separation, Recombination, and Trapping. *J. Phys. Chem. Lett.* **2015**, *6*, 2086–2095.

(168) Wang, L.; Mccleese, C.; Kovalsky, A.; Zhao, Y.; Burda, C. Femtosecond Time-Resolved Transient Absorption Spectroscopy of $CH_3NH_3PbI_3$ Perovskite Films: Evidence for Passivation Effect of PbI_2. *J. Am. Chem. Soc.* **2014**, *136*, 12205–12208.

(169) Yoshida, H.; Ohno, N.; Fujita, M. Exciton Transition of SnI_2 at the Fundamental Absorption Edge. *Phys. Status Solidi B* **1997**, *203*, 281–286.

(170) Even, J.; Pedesseau, L.; Jancu, J.-M.; Katan, C. DFT and $\boldsymbol{k} \cdot \boldsymbol{p}$ Modelling of the Phase Transitions of Lead and Tin Halide Perovskites for Photovoltaic Cells. *Phys. status solidi - Rapid Res. Lett.* **2014**, *8* (1), 31–35.

(171) Fluegel, B.; Francoeur, S.; Mascarenhas, A.; Tixier, S.; Young, E. C.; Tiedje, T. Giant Spin-Orbit Bowing in $GaAs_{1-x}Bi_X$. *Phys. Rev. Lett.* **2006**, *97* (6), 067205.

(172) Fluegel, B.; Mascarenhas, A.; Ptak, A. J.; Tixier, S.; Young, E. C.; Tiedje, T. E+ Transition in $GaAs_{1-x}N_x$ and $GaAs_{1-x}Bi_x$ Due to Isoelectronic-Impurity-Induced Perturbation of the Conduction Band. *Phys. Rev. B* **2007**, *76* (15), 155209.

(173) Wehrenfennig, C.; Liu, M.; Snaith, H. J.; Johnston, M. B.; Herz, L. M. Homogeneous Emission Line Broadening in the Organo Lead Halide Perovskite $CH_3NH_3PbI_{3-x}Cl_X$. *J. Phys. Chem. Lett.* **2014**, *5*, 1300–1306.

(174) Shum, K.; Chen, Z.; Qureshi, J.; Yu, C.; Wang, J. J.; Pfenninger, W.; Vockic, N.; Midgley, J.; Kenney, J. T. Synthesis and Characterization of $CsSnI_3$ Thin Films. *Appl. Phys. Lett.* **2010**, *96*, 221903.

(175) Siebentritt, S.; Rey, G.; Finger, A.; Regesch, D.; Sendler, J.; Weiss, T. P.; Bertram, T. What Is the Bandgap of Kesterite? *Sol. Energy Mater. Sol. Cells* **2016**, *158* (2), 126–129.

(176) Gokmen, T.; Gunawan, O.; Todorov, T. K.; Mitzi, D. B. Band Tailing and Efficiency Limitation in Kesterite Solar Cells. *Appl. Phys. Lett.* **2013**, *103* (10), 103506.

(177) Johnston, M. B.; Herz, L. M. Hybrid Perovskites for Photovoltaics: Charge-Carrier Recombination, Diffusion, and Radiative Efficiencies. *Acc. Chem. Res.* **2015**, *49* (1), 146–154.

(178) Liao, W.; Zhao, D.; Yu, Y.; Shrestha, N.; Ghimire, K.; Grice, C. R.; Wang, C.; Xiao, Y.; Cimaroli, A. J.; Ellingson, R. J.; et al. Fabrication of Efficient Low-Bandgap Perovskite Solar Cells by Combining Formamidinium Tin Iodide with Methylammonium Lead Iodide. *J. Am. Chem. Soc.* **2016**, *138* (38), 12360–12363.

(179) Mitzi, D. B.; Liang, K. Synthesis, Resistivity, and Thermal Properties of the Cubic Perovskite $NH_2CH{=}NH_2SnI_3$ and Related Systems. *J. Solid State Chem.* **1997**, *381* (134), 376–381.

(180) Koh, T. M.; Krishnamoorthy, T.; Yantara, N.; Shi, C.; Leong, W. L.; Boix, P. P.; Grimsdale, A. C.; Mhaisalkar, S. G.; Mathews, N. Formamidinium Tin-Based Perovskite with Low Eg for Photovoltaic Applications. *J. Mater. Chem. A* **2015**, *3*, 14996–15000.

(181) Amat, A.; Mosconi, E.; Ronca, E.; Quarti, C.; Umari, P.; Nazeeruddin, M. K.; Grätzel, M.; De Angelis, F. Cation-Induced Band-Gap Tuning in Organohalide Perovskites: Interplay of Spin-Orbit Coupling and Octahedra Tilting. *Nano Lett.* **2014**, *14* (6), 3608–3616.

(182) Kieslich, G.; Sun, S.; Cheetham, T. An Extended Tolerance Factor Approach for Organic-Inorganic Perovskites. *Chem. Sci.* **2015**, *6*, 3430–3433.

(183) Li, Z.; Yang, M.; Park, J. S.; Wei, S. H.; Berry, J. J.; Zhu, K. Stabilizing Perovskite Structures by Tuning Tolerance Factor: Formation of Formamidinium and Cesium Lead Iodide Solid-State Alloys. *Chem. Mater.* **2016**, *28* (1), 284–292.

(184) Brennan, M. C.; Zinna, J.; Kuno, M. Existence of a Size-Dependent Stokes Shift in $CsPbBr_3$ Perovskite Nanocrystals. *ACS Energy Lett.* **2017**, *2*, 1487−1488.

(185) Sabba, D.; Mulmudi, H. K.; Prabhakar, R. R.; Krishnamoorthy, T.; Baikie, T.; Boix, P. P.; Mhaisalkar, S. G.; Mathews, N. Impact of Anionic Br- Substitution on Open Circuit Voltage in Lead Free Perovskite ($CsSnI_{3-x}Br_x$) Solar Cells. *J. Phys. Chem. C* **2015**, *119* (4), 1763–1767.

(186) Borchert, J.; Milot, R. L.; Patel, J. B.; Davies, C. L.; Wright, A. D.; Martínez Maestro, L.; Snaith, H. J.; Herz, L. M.; Johnston, M. B. Large-Area, Highly Uniform Evaporated Formamidinium Lead Triiodide Thin Films for Solar Cells. *ACS Energy Lett.* **2017**, *2* (12), 2799–2804.

(187) Patel, J. B.; Lin, Q.; Zadvorna, O.; Davies, C. L.; Herz, L. M.; Johnston, M. B. Photocurrent Spectroscopy of Perovskite Solar Cells over a Wide Temperature Range from 15 to 350 K. *J. Phys. Chem. Lett.* **2018**, *9* (1), 263–268.

(188) Roldán-Carmona, C.; Malinkiewicz, O.; Betancur, R.; Longo, G.; Momblona, C.; Jaramillo, F.; Camacho, L.; Bolink, H. J. High Efficiency Single-Junction Semitransparent Perovskite Solar Cells. *Energy Environ. Sci.* **2014**, *7* (9), 2968–2973.

(189) Roldán-Carmona, C.; Malinkiewicz, O.; Soriano, A.; Mínguez Espallargas, G.; Garcia, A.; Reinecke, P.; Kroyer, T.; Dar, M. I.; Nazeeruddin, M. K.; Bolink, H. J. Flexible High Efficiency Perovskite Solar Cells. *Energy Environ. Sci.* **2014**, *7* (3), 994–997.

(190) Zhang, L.; Yuan, F.; Dong, H.; Jiao, B.; Zhang, W.; Hou, X.; Wang, S.; Gong, Q.; Wu, Z. One-Step Co-Evaporation of All-Inorganic Perovskite Thin Films with Room Temperature Ultralow Amplified Spontaneous Emission Threshold and Air-Stability. *ACS Appl. Mater. Interfaces* **2018**, *10* (47), 40661–40671.

(191) Sahli, F.; Werner, J.; Kamino, B. A.; Bräuninger, M.; Monnard, R.; Paviet-Salomon, B.; Barraud, L.; Ding, L.; Leon, J. J. D.; Sacchetto, D.; et al. Fully Textured Monolithic Perovskite/Silicon Tandem Solar Cells with 25.2% Power Conversion Efficiency. *Nat. Mater.* **2018**, *17*, 820–826.

(192) Patel, J. B.; Milot, R. L.; Wright, A. D.; Herz, L. M.; Johnston, M. B. Formation Dynamics of $CH_3NH_3PbI_3$ Perovskite Following Two-Step Layer Deposition. *J. Phys. Chem. Lett.* **2016**, *7* (1), 96–102.

(193) Yang, D.; Yang, Z.; Qin, W.; Zhang, Y.; Liu, S.; Li, C. Alternating Precursor Layer Deposition for Highly Stable Perovskite Films towards Efficient Solar Cells Using Vacuum Deposition. *J. Mater. Chem. A* **2015**, *3* (18), 9401–9405.

(194) Bush, K. A.; Rolston, N.; Gold-Parker, A.; Manzoor, S.; Hausele, J.; Yu, Z.; Raiford, J. A.; Cheacharoen, R.; Holman, Z. C.; Toney, M. F.; et al. Controlling Thin Film Stress and Wrinkling During Perovskite Film Formation. *ACS Energy Lett.* **2018**, *3*, 1225–1232.

(195) Zhao, J.; Deng, Y.; Wei, H.; Zheng, X.; Yu, Z.; Shao, Y.; Shield, J. E.; Huang, J. Strained Hybrid Perovskite Thin Films and Their Impact on the Intrinsic Stability of Perovskite Solar Cells. *Sci. Adv.* **2017**, *3* (11), eaao5616.

(196) Momblona, C.; Gil-Escrig, L.; Bandiello, E.; Hutter, E. M.; Sessolo, M.; Lederer, K.; Blochwitz-Nimoth, J.; Bolink, H. J. Efficient Vacuum Deposited p-i-n and n-i-p Perovskite Solar Cells Employing Doped Charge Transport Layers. *Energy Environ. Sci.* **2016**, *9* (11), 3456–3463.

(197) Heo, J. H.; Song, D. H.; Im, S. H. Planar $CH_3NH_3PbBr_3$ Hybrid Solar Cells with 10.4% Power Conversion Efficiency, Fabricated by Controlled Crystallization in the Spin-Coating Process. *Adv. Mater.* **2014**, *26* (48), 8179–8183.

(198) Jiang, Q.; Chu, Z.; Wang, P.; Yang, X.; Liu, H.; Wang, Y.; Yin, Z.; Wu, J.; Zhang, X.; You, J. Planar-Structure Perovskite Solar Cells with Efficiency beyond 21%. *Adv. Mater.* **2017**, *29* (46), 1703852.

(199) Bi, C.; Wang, Q.; Shao, Y.; Yuan, Y.; Xiao, Z.; Huang, J. Non-Wetting Surface-Driven High-Aspect-Ratio Crystalline Grain Growth for Efficient Hybrid Perovskite Solar Cells. *Nat. Commun.* **2015**, *6*, 7747.

(200) Rothmann, M. U.; Li, W.; Etheridge, J.; Cheng, Y. B. Microstructural Characterisations of Perovskite Solar Cells - From Grains to Interfaces: Techniques, Features, and Challenges. *Adv. Energy Mater.* **2017**, *7* (23), 1700912.

(201) Chiang, C. H.; Wu, C. G. Film Grain-Size Related Long-Term Stability of Inverted Perovskite Solar Cells. *ChemSusChem* **2016**, *9* (18), 2666–2672.

(202) Chu, Z.; Yang, M.; Schulz, P.; Wu, D.; Ma, X.; Seifert, E.; Sun, L.; Li, X.; Zhu, K.; Lai, K. Impact of Grain Boundaries on Efficiency and Stability of Organic-Inorganic Trihalide Perovskites. *Nat. Commun.* **2017**, *8* (1), 2230.

(203) Ioakeimidis, A.; Christodoulou, C.; Lux-Steiner, M.; Fostiropoulos, K. Effect of PbI_2 Deposition Rate on Two-Step PVD/CVD All-Vacuum Prepared Perovskite. *J. Solid State Chem.* **2016**, *244*, 20–24.

(204) Wang, H.; Bao, Z.; Tsai, H.; Tang, A.; Liu, R. Perovskite Quantum Dots and Their Application. *Small* **2017**, *14* (1), 1702433.

(205) Wang, N.; Cheng, L.; Ge, R.; Zhang, S.; Miao, Y.; Zou, W.; Yi, C.; Sun, Y.; Cao, Y.; Yang, R.; et al. Perovskite Light-Emitting Diodes Based on Solution-Processed Self-Organized Multiple Quantum Wells. *Nat. Photonics* **2016**, *10* (11), 699–704.

(206) Lin, K.; Xing, J.; Quan, L. N.; de Arquer, F. P. G.; Gong, X.; Lu, J.; Xie, L.; Zhao, W.; Zhang, D.; Yan, C.; et al. Perovskite Light-Emitting Diodes with External Quantum Efficiency Exceeding 20 Percent. *Nature* **2018**, *562* (7726), 245–248.

(207) Ban, M.; Zou, Y.; Rivett, J. P. H.; Yang, Y.; Thomas, T. H.; Tan, Y.; Song, T.; Gao, X.; Credington, D.; Deschler, F.; et al. Solution-Processed Perovskite Light Emitting Diodes with Efficiency Exceeding 15% through Additive-Controlled Nanostructure Tailoring. *Nat. Commun.* **2018**, *9*, 3892.

(208) Zhang, X.; Lu, M.; Zhang, Y.; Wu, H.; Shen, X.; Zhang, W.; Zheng, W.; Colvin, V. L.; Yu, W. W. PbS Capped $CsPbI_3$ Nanocrystals for Efficient and Stable Light-Emitting Devices Using *p-i-n* Structures. *ACS Cent. Sci.* **2018**, *4*, 1352–159.

(209) Quintero-Bermudez, R.; Gold-Parker, A.; Proppe, A. H.; Munir, R.; Yang, Z.;

Kelley, S. O.; Amassian, A.; Toney, M. F.; Sargent, E. H. Compositional and Orientational Control in Metal Halide Perovskites of Reduced Dimensionality. *Nat. Mater.* **2018**, *17* (10), 900–907.

(210) Polavarapu, L.; Nickel, B.; Feldmann, J.; Urban, A. S. Advances in Quantum-Confined Perovskite Nanocrystals for Optoelectronics. *Adv. Energy Mater.* **2017**, *7* (16), 1700267.

(211) Narukawa, Y.; Ichikawa, M.; Sanga, D.; Sano, M.; Mukai, T. White Light Emitting Diodes with Super-High Luminous Efficacy. *J. Phys. D. Appl. Phys.* **2010**, *43*, 354002.

(212) Yang, B.; Dyck, O.; Ming, W.; Du, M.-H.; Das, S.; Rouleau, C. M.; Duscher, G.; Geohegan, D. B.; Xiao, K. Observation of Nanoscale Morphological and Structural Degradation in Perovskite Solar Cells by in Situ TEM. *ACS Appl. Mater. Interfaces* **2016**, *8* (47), 32333–32340.

(213) Pistor, P.; Borchert, J.; Fra, W.; Csuk, R.; Scheer, R. Monitoring the Phase Formation of Coevaporated Lead Halide Perovskite Thin Films by in Situ X-Ray Diffraction. *J. Phys. Chem. Lett.* **2014**, *5*, 3308–3312.

(214) Pistor, P.; Burwig, T.; Brzuska, C.; Weber, B.; Fränzel, W. Thermal Stability and Miscibility of Co-Evaporated Methyl Ammonium Lead Halide ($MAPbX_3$, X = I, Br, Cl) Thin Films Analysed by in Situ X-Ray Diffraction. *J. Mater. Chem. A* **2018**, *6*, 11496–11506.

(215) Xu, H.; Wu, Y.; Cui, J.; Ni, C.; Xu, F.; Cai, J.; Hong, F.; Fang, Z.; Wang, W.; Zhu, J.; et al. Formation and Evolution of the Unexpected PbI_2 Phase at the Interface during the Growth of Evaporated Perovskite Films. *Phys. Chem. Chem. Phys.* **2016**, *18* (27), 18607–18613.

(216) Olthof, S.; Meerholz, K. Substrate-Dependent Electronic Structure and Film Formation of $MAPbI_3$ Perovskites. *Sci. Rep.* **2017**, *7*, 40267.

(217) Zhou, X.; Li, X.; Liu, Y.; Huang, F.; Zhong, D. Interface Electronic Properties of Co-Evaporated $MAPbI_3$ on ZnO(0001): In Situ X-Ray Photoelectron Spectroscopy and Ultraviolet Photoelectron Spectroscopy Study. *Appl. Phys. Lett.* **2016**, *108*, 121601.

(218) Alsari, M.; Bikondoa, O.; Bishop, J.; Abdi-Jalebi, M.; Lutfiye, O. Y.; Hampton, M.; Thompson, P.; Horantner, M. T.; Mahesh, S.; Greenland, C.; et al. In Situ Simultaneous Photovoltaic and Structural Evolution of Perovskite Solar Cells during Film. *Energy Environ. Sci.* **2018**, *11*, 383–393.

(219) Zhao, L.; Lee, K. M.; Roh, K.; Khan, S. U. Z.; Rand, B. P. Improved Outcoupling Efficiency and Stability of Perovskite Light-Emitting Diodes Using Thin Emitting Layers. *Adv. Mater.* **2018**, 1805836.

(220) Feng, J. Mechanical Properties of Hybrid Organic-Inorganic $CH_3NH_3BX_3$ (B = Sn, Pb; X = Br, I) Perovskites for Solar Cell Absorbers. *APL Mater.* **2014**, *2* (8), 081801.

(221) Baikie, T.; Fang, Y.; Kadro, J. M.; Schreyer, M.; Wei, F.; Mhaisalkar, S. G.; Graetzel, M.; White, T. J. Synthesis and Crystal Chemistry of the Hybrid Perovskite $(CH_3NH_3)PbI_3$ for Solid-State Sensitised Solar Cell Applications. *J. Mater. Chem. A* **2013**, *1* (18), 5628.

(222) Liu, Y.; Yang, Z.; Cui, D.; Ren, X.; Sun, J.; Liu, X.; Zhang, J.; Wei, Q.; Fan, H.; Yu, F.; et al. Two-Inch-Sized Perovskite $CH_3NH_3PbX_3$ (X = Cl, Br, I) Crystals: Growth and Characterization. *Adv. Mater.* **2015**, *27* (35), 5176–5183.

(223) Dang, Y.; Liu, Y.; Sun, Y.; Yuan, D.; Liu, X.; Lu, W.; Liu, G.; Xia, H.; Tao, X. Bulk Crystal Growth of Hybrid Perovskite Material $CH_3NH_3PbI_3$. *CrystEngComm* **2015**, *17* (3), 665–670.

(224) Cammarata, R. C.; Trimble, T. M.; Srolovitz, D. J. Surface Stress Model for Intrinsic Stresses in Thin Films. *J. Mater. Res.* **2000**, *15* (11), 2468–2474.

(225) Thornton, J. A. Stress-Related Effects in Thin Films. *Thin Solid Films* **1989**, *171*, 5–31.

(226) Cammarata, R. C. Surface and Interface Stress Effects on the Growth of Thin Films. *Prog. Surf. Sci.* **1994**, *46* (1), 1–38.

(227) Chason, E.; Guduru, P. R. Tutorial: Understanding Residual Stress in Polycrystalline Thin Films through Real-Time Measurements and Physical Models. *J. Appl. Phys.* **2016**, *119*, 191101.

(228) Niu, L.; Zeng, Q.; Shi, J.; Cong, C.; Wu, C.; Liu, F.; Zhou, J.; Fu, W.; Fu, Q.; Jin, C.; et al. Controlled Growth and Reliable Thickness-Dependent Properties of

Organic-Inorganic Perovskite Platelet Crystal. *Adv. Funct. Mater.* **2016**, *26*, 5263–5270.

(229) Di, D.; Musselman, K. P.; Li, G.; Sadhanala, A.; Ievskaya, Y.; Song, Q.; Tan, Z.-K.; Lai, M. L.; MacManus-Driscoll, J. L.; Greenham, N. C.; et al. Size-Dependent Photon Emission from Organometal Halide Perovskite Nanocrystals Embedded in an Organic Matrix. *J. Phys. Chem. Lett.* **2015**, *6* (3), 446–450.

(230) Hall, W. H. X-Ray Line Broadening in Metals. *Proc. Phys. Soc. A* **1949**, *62*, 741–743.

(231) Wang, J. T. W.; Wang, Z.; Pathak, S.; Zhang, W.; Dequilettes, D. W.; Wisnivesky-Rocca-Rivarola, F.; Huang, J.; Nayak, P. K.; Patel, J. B.; Mohd Yusof, H. A.; et al. Efficient Perovskite Solar Cells by Metal Ion Doping. *Energy Environ. Sci.* **2016**, *9*, 2892–2901.

(232) McMeekin, D. P.; Wang, Z.; Rehman, W.; Pulvirenti, F.; Patel, J. B.; Noel, N. K.; Johnston, M. B.; Marder, S. R.; Herz, L. M.; Snaith, H. J. Crystallization Kinetics and Morphology Control of Formamidinium-Cesium Mixed-Cation Lead Mixed-Halide Perovskite via Tunability of the Colloidal Precursor Solution. *Adv. Mater.* **2017**, *29*, 1607039.

(233) Rolston, N.; Watson, B. L.; Dauskardt, R. H. Mechanical Integrity of Solution-Processed Perovskite Solar Cells. *Extrem. Mech. Lett.* **2016**, *9*, 353–358.

(234) Stranski, I. N.; Krastanow, L. Zur Theorie Der Orientierten Ausscheidung von Ionenkristallen Aufeinander. *Abhandlungen der Math. Klasse IIb* **1938**, *146*, 797–810.

(235) Reichelt, K.; Jiang, X. The Preparation of Thin Films by Physical Vapour Deposition Methods. *Thin Solid Films* **1990**, *191* (1), 91–126.

(236) Buin, A.; Comin, R.; Ip, A. H.; Sargent, E. H. Perovskite Quantum Dots Modeled Using Ab Initio and Replica Exchange Molecular Dynamics. *J. Phys. Chem. C* **2015**, *119* (24), 13965–13971.

(237) Grote, C.; Berger, R. F.; DeQuilettes, D. W.; Koch, S.; Burke, S.; Paranji, R.; Shropshire, A. J.; Ziffer, M. E.; Ginger, D. S. Strain Tuning of Tin–Halide and Lead–Halide Perovskites: A First-Principles Atomic and Electronic Structure

Study. *J. Phys. Chem. C* **2015**, *119* (40), 22832–22837.

(238) Merdasa, A.; Bag, M.; Tian, Y.; Källman, E.; Dobrovolsky, A.; Scheblykin, I. G. Super-Resolution Luminescence Microspectroscopy Reveals the Mechanism of Photoinduced Degradation in $CH_3NH_3PbI_3$ Perovskite Nanocrystals. *J. Phys. Chem. C* **2016**, *120* (19), 10711–10719.

APPENDICES

A. SRH recombination with shallow traps

As discussed in Section 2.5.2, the general formula for SRH recombination does not have a rate equal to $k_1\Delta n$, with k_1 constant. To demonstrate this behaviour more clearly I have solved the rate equation $d(\Delta n)/dt = - U_{SRH}$ numerically for several scenarios, shown in Figure A.1, where U_{SRH} is defined by Equation 2.7

For all the following scenarios, the SRH lifetimes were taken to be $\tau_n = \tau_p = 1$ ns. The initial photoexcited carrier density was set as $\Delta n_0 = 10^{14}$ cm^{-3} and the intrinsic carrier density was taken to be $p_0 = n_0 = 10^5$cm^{-3} for both holes and electrons, calculated from

$$n_0 = N_c \exp((E_F - E_g)/kT)$$
$$p_0 = N_V \exp(-E_F/kT)$$

Equation A.1

setting zero energy at the top of the valence band, with $N_c = N_V = 10^{15}$, $E_F = 0.6$ eV, $E_g = 1.2$ eV and T = 300 K.

The scenarios are as follows:

Heavily p-doped:
$p_0 = 10^{16}$ cm^{-3}. First case: Mid-gap trap state which gives $p_1 = n_1 = 10^5$cm^{-3}. Second case: very shallow traps with $n_1 = 5\text{x}10^{14}$cm^{-3} (both these scenarios give the same result).
The solution is equivalent to a mono-exponential decay with $k_1 = 1/\tau_n$.

Moderately p-doped:
$p_0 = 10^{14}$ cm^{-3}. Mid-gap trap state which gives $p_1 = n_1 = 10^5$cm^{-3}.
The solution is equivalent to k_1 changing from $1/(\tau_n + \tau_p)$ to $1/\tau_n$ as time goes on and Δn decreases.

Intrinsic:
$p_0 = n_0 = 10^5$cm^{-3}. Mid-gap trap state which gives $p_1 = n_1 = 10^5$cm^{-3}.
The solution is equivalent to a mono-exponential decay with $k_1 = 1/(\tau_n + \tau_p)$.

Shallow trap:

Intrinsic doping. Trap level E_t = 0.1 eV below conduction band which gives $n_1 = N_c \exp((E_t\text{-}E_g)/kT) = 7\text{x}10^{13}\text{cm}^{-3}$, $p_1 = N_V \exp(-E_t/kT) = 0\ \text{cm}^{-3}$.

The decay is no longer exponential and appears 'stretched', since k_1 depends on Δn.

Very shallow trap:

Intrinsic doping. Trap level 0.05 eV below Fermi level which gives $n_1 = 5\text{x}10^{14}\text{cm}^{-3}$, $p_1 = 0\ \text{cm}^{-3}$.

The lifetime of the decay is increased for shallower traps.

Very shallow trap with moderate doping:

$p_0 = 10^{14}\ \text{cm}^{-3}$. Trap level 0.05 eV below Fermi level which gives $n_1 = 5\text{x}10^{14}\text{cm}^{-3}$, $p_1 = 0\ \text{cm}^{-3}$.

The solution becomes mono-exponential again, but the lifetime is longer than for deep traps.

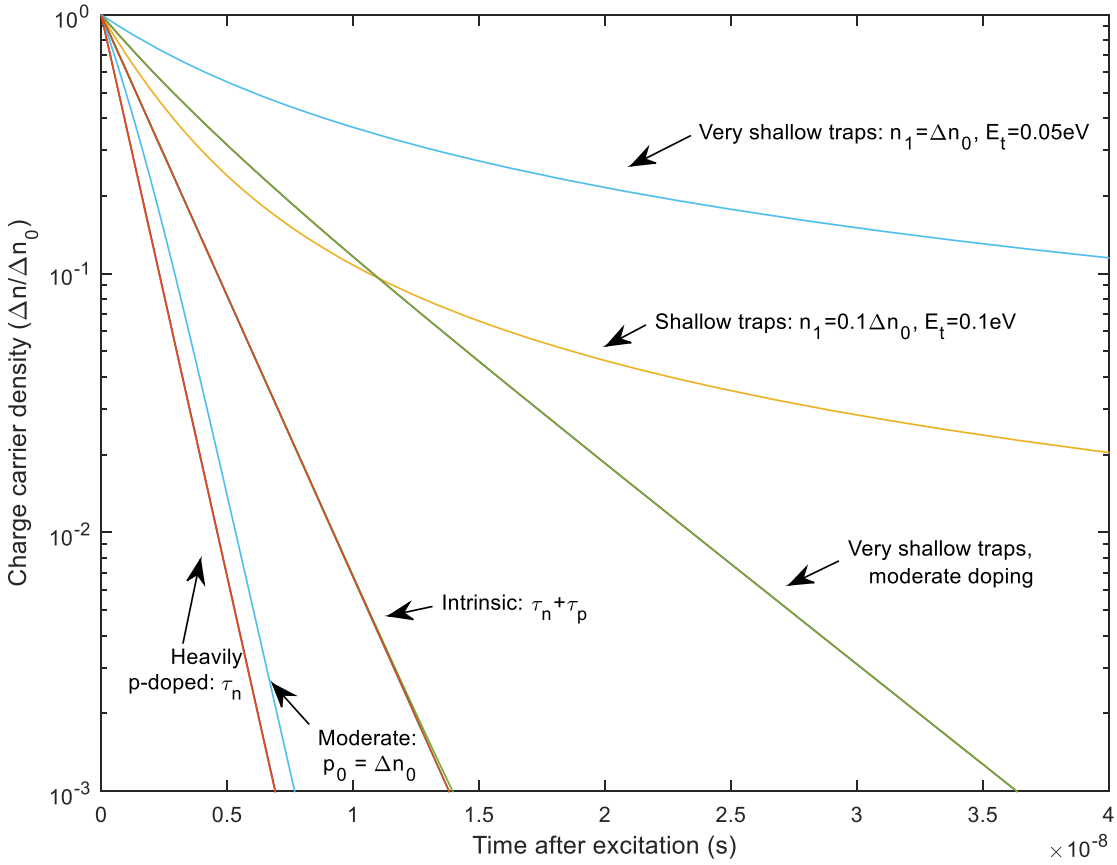

Figure A.1. Simulation of the charge-carrier density decay curves for SRH recombination under a range of conditions.

B. PLQE for transient measurements

Equation 2.10 for the PL quantum efficiency assumes a constant carrier density, however in this thesis the PLQE is measured with a pulsed laser, such that the carrier density decays to zero between each pulse. Here I investigate whether it is valid to use an average carrier density from a transient measurement, in the PLQE formula for steady state.

For pulsed measurements, the carrier density, and therefore the recombination rates, are time dependent. Equation 2.10 must therefore be integrated over the measurement time, or equivalently, the time between excitation pulses. The PLQE is then given by

$$\varphi_{\text{pulse}} = \frac{\int U_r dt}{\int U_r + U_{nr} dt}$$

Equation B.1

where U_r is the radiative recombination rate and U_{nr} is the non-radiative recombination rate, as in Equation 2.10. This is equivalent to the number of charge-carriers recombining radiatively divided by the total number of photoexcited charge-carriers. Assuming the carrier density decays entirely within the pulse window, the bottom of the equation above is equal to Δn_0, the initial photoexcited charge-carrier density.

To perform the integrals in Equation B.1, we need to know how the recombination rates depend on charge-carrier density Δn and also how Δn changes with time. We assume that Equation 2.5 gives a suitable time dependence for the charge-carrier density, and that both k_1 and k_2 can be radiative or non-radiative.

We can now integrate the top of Equation B.1, with U_r given by

$$U_r = k_1^r \Delta n + k_2^r \Delta n^2$$

Equation B.2

Integrating the terms of Equation B.2 over the time between laser pulses, t_p, gives

$$\int_0^{t_p} \Delta n \, dt = \Delta n_0 \frac{K}{k_1} log\left(\frac{K + 1 - e^{-k_1 t_p}}{K}\right)$$

Equation B.3

$$\int_0^{t_p} \Delta n^2 \, dt = \Delta n_0^2 \frac{K^2}{k_1}\left[t_p k_1 - \frac{1}{x} - log\left(\frac{x}{K}\right) + \frac{1}{K}\right]$$

Equation B.4

where $K = k_1/(k_2 \Delta n_0)$ is a dimensionless parameter as in Equation 2.5 and $x = (1 + K) \exp(k_1 t_p) - 1$.

Assuming the charge-carrier density effectively decays to zero within the pulse window, we can let t_p tend to infinity:

$$\varphi_{pulse} = \frac{1}{\Delta n_0}\int_0^{\infty} U_{rad} dt = \frac{1}{\Delta n_0}\int_0^{\infty} k_1^r \Delta n + \, k_2^r \Delta n^2 dt$$

Equation B.5

$$\varphi_{pulse} = \frac{k_1^r}{k_1} K \, log\left(\frac{K + 1}{K}\right) + \frac{k_2^r}{k_2}\left[1 - K \, log\left(\frac{K + 1}{K}\right)\right]$$

Equation B.6

Expressing the steady state PLQE in terms of k_1 and k_2 gives

$$\varphi_{steady} = \frac{k_1^r}{k_1}\frac{K}{K + 1} + \frac{k_2^r}{k_2}\frac{1}{K + 1}$$

Equation B.7

To use this simpler steady-state equation for pulsed measurements, we need to choose a suitable carrier density to use in $K = k_1/(k_2 \Delta n_{ave})$.

To make the steady state and pulsed expressions for PLQE equivalent, the average carrier density must be chosen to be

$$n_{ave} = \frac{\int \Delta n^2 dt}{\int \Delta n \, dt}$$

Equation B.8

which for a simple exponential decay is equal to $\Delta n_0/2$. The average value can approach Δn_0 if the lifetime is long with respect to the pulse window, and can be less than $\Delta n_0/2$ if the decay is stretched, which will change with temperature for our measurements. However, since we are more concerned about the order of magnitude of

the PLQE than the precise value, we consider the use of the steady state formula with an average carrier density of $\Delta n_0/2$ to be a suitable approximation. An example is shown in Figure B.1 showing that the approximation of a constant Δn_0 diverges as k_2 is changed, however, the bottom panel shows on a log scale that this difference is negligible.

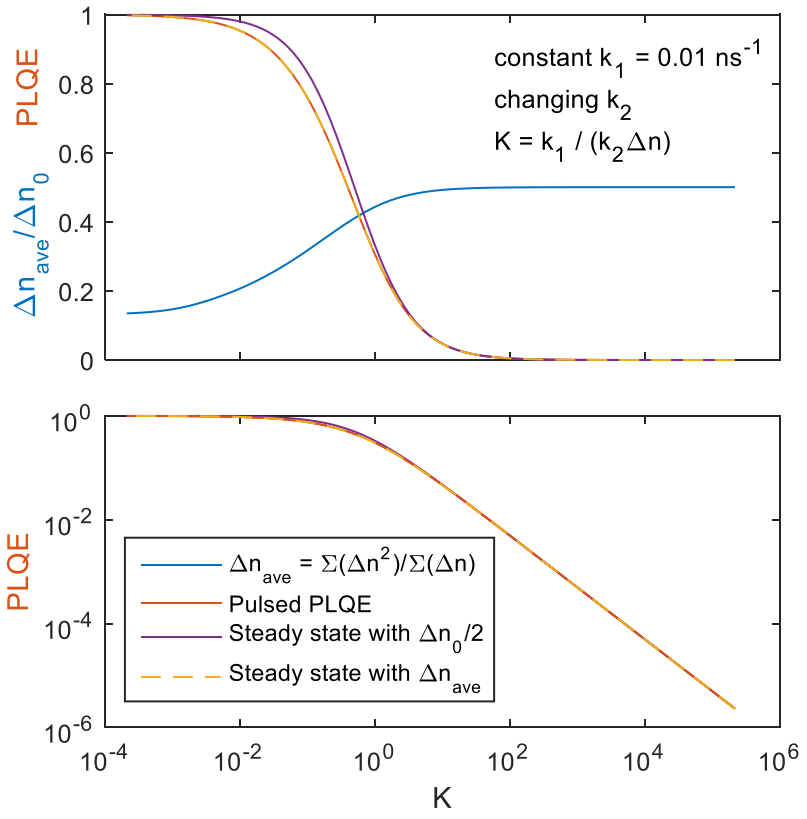

Figure B.1. Simulation of the PLQE under pulsed and steady-state excitation, showing that a correct choice of the carrier density can make the expressions equivalent.